Materials Horizons

ROYAL SOCIETY OF CHEMISTRY

REVIEW

View Article Online
View Journal | View Issue



Cite this: *Mater. Horiz.*, 2024, **11**, 3213

# Two decades of ceria nanoparticle research: structure, properties and emerging applications

Ali Othman,†[ab] Akshay Gowda,†[b] Daniel Andreescu,[a] Mohamed H. Hassan,[a] S. V. Babu,[b] Jihoon Seo *[b] and Silvana Andreescu *[a]

Received 17th January 2024,
Accepted 26th April 2024

DOI: 10.1039/d4mh00055b

rsc.li/materials-horizons



Cerium oxide nanoparticles (CeNPs) are versatile materials with unique and unusual properties that vary depending on their surface chemistry, size, shape, coating, oxidation states, crystallinity, dopant, and structural and surface defects. This review encompasses advances made over the past twenty years in the development of CeNPs and ceria-based nanostructures, the structural determinants affecting their activity, and translation of these distinct features into applications. The two oxidation states of nanosized CeNPs ($Ce^{3+}/Ce^{4+}$) coexisting at the nanoscale level facilitate the formation of oxygen vacancies and defect states, which confer extremely high reactivity and oxygen buffering capacity and the ability to act as catalysts for oxidation and reduction reactions. However, the method of synthesis, surface functionalization, surface coating and defects are important factors in determining their properties. This review highlights key properties of CeNPs, their synthesis, interactions, and reaction pathways and provides examples of emerging applications. Due to their unique properties, CeNPs have become quintessential candidates for catalysis, chemical mechanical planarization (CMP), sensing, biomedical applications, and environmental remediation, with tremendous potential to create novel products and translational innovations in a wide range of industries. This review highlights the timely relevance and the transformative potential of these materials in addressing societal challenges and driving technological advancements across these fields.

**Wider impact**

Ceria nanoparticles or nanoceria is a versatile material with unique and unusual optical, mechanical and catalytic properties. The co-existence of two-oxidation states $Ce^{3+}/Ce^{4+}$ at the nanoscale level facilitates the formation of oxygen vacancies and defect states, which confer an extremely high reactivity and the ability to act as a catalyst for both oxidation and reduction reactions. Due to its unique features, we now see a broad interest in the implementation of this material across a wide array of industries. However, its unique features are a function of the chemical, structural, surface defects, size, shape and doping effects, which are currently not fully understood. This review provides a comprehensive, critical, and accessible resource of general interest to the materials community, highlighting the structure and fundamental properties of this material and translation of its distinct features into applications. Scientists can use this resource as a starting point to explore this material's properties and pursue avenues for creating new products and breakthrough innovations.

## 1. Introduction

Cerium, a member of the lanthanide series, is the most abundant of all rare earth metals. Unlike other elements in the series that typically exist in the +3 state, cerium adopts between +3 and +4 oxidation states, exhibiting unique redox properties and reactivity. Its oxide form, *e.g.* ceria, cerium oxide or cerium dioxide ($CeO_2$), has gained significant interest in both industry and academia. Ceria-based materials, composed of $CeO_2$, embody an array of distinctive features that make them highly desirable across many scientific areas and a wide range of industries. Nanosized ceria has gained significant attention over the past twenty years owing to its exceptional properties at the nanoscale. The unique crystal structure, characterized by the presence of oxygen vacancies and cerium cations with variable oxidation states, confers a plethora of properties including high oxygen storage capacity, redox activity, high surface functionality and catalytic power. Notably, nanoscale ceria can accommodate more oxygen vacancies in its crystal structure than its bulk counterpart.[1] This attribute

[a] *Department of Chemistry and Biomolecular Science, Clarkson University, Potsdam, New York 13699-5810, USA. E-mail: eandrees@clarkson.edu*
[b] *Department of Chemical and Biomolecular Engineering, Clarkson University, Potsdam, New York 13699, USA. E-mail: jseo@clarkson.edu*
† Contributed equally to this work.

enables ceria nanoparticles (CeNPs) to exhibit very high oxygen mobility and exceptional oxygen storage capacity (OSC), making them adept at releasing and storing oxygen depending on the redox environment. These distinctive features have spurred intense investigation into CeNPs' research and exploration of their properties in applications ranging from catalysis, energy conversion, semiconducting industries to environmental remediation, biosensing and biomedicine.

Ceria-based materials are used in catalytic converters, solid oxide fuel cells (SOFCs), catalysts for volatile organic compound (VOC) oxidation, sensors, and chemical mechanical planarization (CMP). More recently, the scope of CeNPs has expanded to water and $CO_2$ splitting for hydrogen production and biomedical applications as enzyme mimetics, theranostic probes and therapeutic materials. Over 30 000 reports have been published on the synthesis, properties, and applications of ceria-based materials,[2–7] many focusing on their role in catalysis, energy and environment. An emerging trend is the exploration of CeNPs in fields such as pharmacology, medicine, biosensing and bioimaging.[8,9] However, challenges like biodistribution, cross-reactivity with clinically relevant species, and potential toxicity constrain their commercial potential.[10,11]

This review aims to offer readers a comprehensive understanding of critical physicochemical properties of the CeNPs, focusing on surface modification, doping and structure–activity relationships, followed by an exploration of their significant applications. Throughout this review, we will highlight the importance of CeNPs' structural design parameters, interactions, and reactivity in the context of next-generation devices. We will commence by examining the structural and shape-dependent properties of CeNPs, followed by a discussion of size-dependent characteristics, with a particular emphasis on

**Ali Othman**

*Ali Othman received his PhD in Chemistry from Clarkson University (Potsdam, NY, USA) in 2019. He was a Postdoctoral Associate and Adjunct Assistant Professor at Clarkson University (2019–2022). His research interests focus on the development of novel functional nanomaterials and their applications for (bio)-sensing, bioanalytical, chemical mechanical planarization (CMP), and environmental remediation applications. He has co-authored over 25 peer-reviewed papers, 4 patents and 2 book chapters. Currently, Dr Othman is a Research Scientist leading and working on the development of materials for gas/liquid purification at Pall Corporation, USA.*

**Akshay Gowda**

*Dr Akshay Gowda is a Process Integration Engineer at Intel Corporation, Rio Rancho, NM, USA. He received his PhD in Chemical and Biomolecular Engineering from Clarkson University, Potsdam, NY, USA in 2020. His PhD thesis focused on the physico-chemical properties of ceria particles and developing cleaning chemistries for their removal from silicon dioxide film surfaces for wafer cleaning applications post-chemical mechanical planarization (CMP) process in semiconductor industries. After working as a CMP Process Development Engineer for two years, he currently works on developing and integrating processes for photonics-based chips.*

**Daniel Andreescu**

*Daniel Andreescu is Associate Professor in the Department of Chemistry and Biomolecular Science at Clarkson University. He received his MS and PhD degrees in Chemistry from the University of Bucharest, Romania in 2002. Between 1996 and 2001, he was researcher at the National Research and Development Institute for Industrial Ecology. In 2003, he joined Clarkson University, where he currently works on the synthesis and characterization of nanosize metallic and metal-composite particles and their applications in sensing and environmental remediation.*

**Mohamed H. Hassan**

*Dr Mohamed H. Hassan is a postdoctoral research fellow in the Department of Materials Science and Engineering at the University of Pennsylvania. He earned his PhD in Chemistry from Clarkson University in 2023. His primary research endeavors revolve around investigating charge transport in metal–organic materials, with a specific emphasis on their practical applications in water remediation, energy storage, and conversion technologies.*

the $Ce^{3+}/Ce^{4+}$ ratio and oxygen vacancies, along with the mechanisms underlying oxygen vacancy formation. Ceria doping is a pivotal focus as it can substantially enhance ceria's properties, opening doors to innovative applications. We delve into the intricacies of the doping process and the role of doped ceria in catalytic reactions. Subsequently, we address the antioxidant properties of CeNPs and their interactions with reactive oxygen species (ROS), touching upon their potential applications in catalysis, sensing, and biomedicine. A dedicated section will cover surface functionalization and its crucial role in modulating interactions between NPs and their surrounding environment. Additionally, we will explore the incorporation of CeNPs into composite and nanohybrid structures interfaced with other metals or rare-earth metal oxides,[12] enhancing their performance and augmenting their area of applicability. Finally, we will delineate applications and future directions, encompassing catalysis, CMP, biosensing, and environmental remediation.

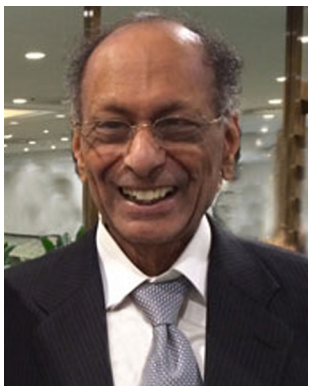

S. V. Babu

*Dr Babu is Professor Emeritus at Clarkson University, where he was the Director (1999–2016) of the NY State Center for Advanced Materials Processing (CAMP) and Vice Provost, Research (2001–04). He is now CTO, ChEmpower Corp. His PhD (Physics) is from SUNY, Stony Brook (1971). He held research appointments at Niels Bohr Institute, Copenhagen, International Center for Theoretical Physics, Trieste and NYU. He started at IIT, Kanpur, in 1972, and moved to Clarkson in 1981. He published over 290 papers, is the co-author of 33 patents, and co-edited four books. Babu supervised 50 PhD and 40 MS students.*

## 2. Physicochemical properties of ceria nanoparticles

Physicochemical properties, including size, shape, crystal plane, and surface chemistry, have significant influence over the reactivity of ceria particles. Over the past two decades, substantial efforts have been dedicated to modulating oxygen vacancy levels and $Ce^{3+}/Ce^{4+}$ ratio by manipulating the synthesis conditions. A significant body of research has been dedicated to the creation of ceria particles with enhanced reactivity and higher $Ce^{3+}$ concentration at the surface. This can be achieved through variations in the surface size and by doping with rare earth (RE), transition, or noble metals. This interest is driven by CeNPs' remarkable capacity to neutralize free radicals, which has garnered considerable attention in the field of biomedicine. It has led to the development of innovative ceria-based antioxidant therapeutics. The recognized antioxidant activity of CeNPs is strongly linked to their redox activity, the $Ce^{3+}$ levels present at the surface, and the presence of oxygen vacancies. In this section, our focus will be on elucidating how the structural and physicochemical properties of ceria influence over oxygen vacancies and surface reactivity (Fig. 1).

### 2.1. Structural and defect properties

Bulk cerium oxide or ceria has a fluorite crystal structure with face-centered cubic unit cell (space group $Fm\bar{3}m$) and a lattice parameter of 5.411 Å at room temperature. In this arrangement, each $Ce^{4+}$ ion (yellow spheres) is surrounded by eight nearest-neighbor $O^{2-}$ ions (red spheres), forming a cube structure. Each $O^{2-}$ ion is tetrahedrally coordinated to four closest $Ce^{4+}$ ions, as depicted in Fig. 2a.

Jihoon Seo

*Dr Jihoon Seo is an Assistant Professor of Chemical and Biomolecular Engineering at Clarkson University in NY, USA. He holds a PhD in Energy Engineering and a Bachelor of Engineering in Materials Science and Engineering from Hanyang University in South Korea. His research focuses on novel planarization and cleaning technologies in manufacturing processes. Dr Seo collaborates with semiconductor manufacturers and equipment suppliers, advancing CMP through the development of cutting-edge processes and materials. Currently, Prof. Seo is leading the CMP team at Clarkson University.*

Silvana Andreescu

*Dr Silvana Andreescu is the Egon Matijević Endowed Chair in Chemistry in the Department of Chemistry and Biomolecular Science at Clarkson University. She received her PhD in 2002 from the University of Bucharest, Romania and University of Perpignan, France. Dr Andreescu's research program integrates electroanalytical, biochemical and materials science advances to develop innovative sensing technology for human and environmental health. Her recent work features the development of easy-to-use chemical and biological sensors based on nanoceria chemistry for the field detection of clinical, food and environmental targets.*

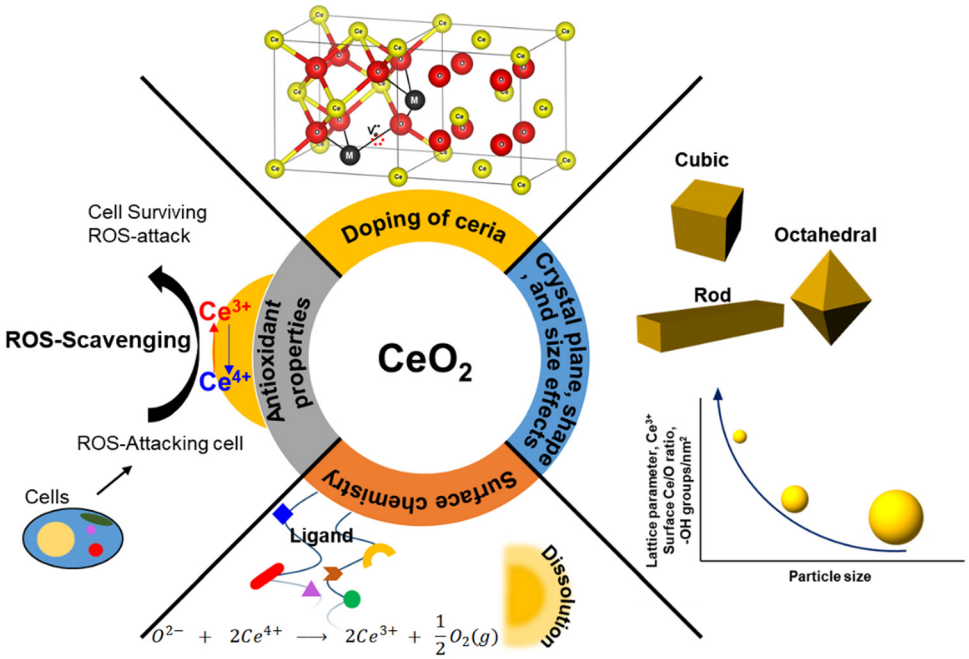


Fig. 1 Summary of physicochemical properties that influence the reactivity of CeNPs.

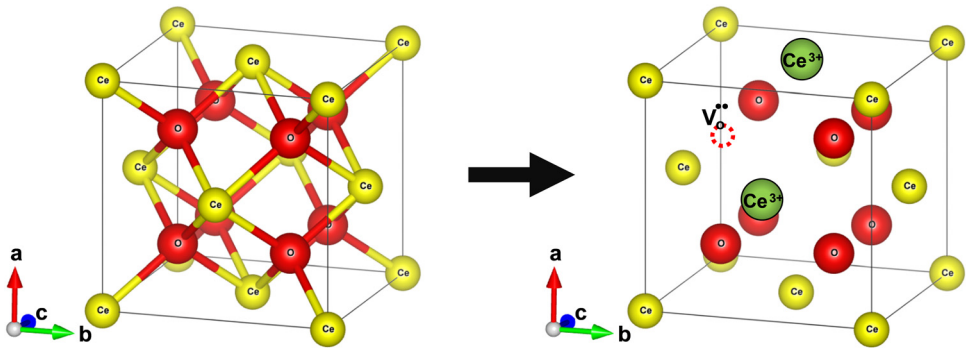


Fig. 2 Schematic diagram of reversible lattice distortion in a cubic ceria unit cell. (a) Fluorite crystal structure of bulk ceria. (b) Distorted crystal structure of nanoceria due to the formation of oxygen vacancy and concomitant reduction of $Ce^{4+}$ ions to $Ce^{3+}$ ions. Red and yellow-colored spheres represent $O^{-}$- and $Ce^{4+}$ ions, respectively, while green spheres represent $V_o^{\bullet\bullet}$.

Defects within ceria can be introduced by changing temperature, oxygen partial pressure, electrical field or surface stress, or through the incorporation of other ions, and these defects can be broadly categorized into intrinsic and extrinsic types.[1] Intrinsic defects primarily arise due to thermal fluctuations or interaction with the surrounding environment such as redox processes. In contrast, extrinsic defects emerge from impurities or the introduction of dopants[1] (will be covered in Section 2.4). The two most noteworthy intrinsic defects observed in ceria are oxygen vacancies[13,14] and anion Frenkel defect. In an anion Frenkel defect, an oxygen ion is displaced from its lattice position to an interstitial position, resulting in a defect at the interstitial location and a vacancy at the original position.[15] These defects are typically present in low concentrations and do not impact the lattice change.

In oxygen vacancy type defect, an oxygen vacancy is created due to the liberation of an oxygen ion from a lattice site. The two excess electrons generated by the vacancy created are localized on two neighboring cerium ions, thereby reducing $Ce^{4+}$ to $Ce^{3+}$.[16,17] This process can be represented as follows.

$$O^{2-} + 2Ce^{4+} \rightarrow 2Ce^{3+} + \frac{1}{2}O_2(g) \quad (2.1)$$

$$O_o^{\times} + 2Ce_{Ce}^{\times} \rightarrow V_o^{\bullet\bullet} + 2Ce_{Ce}^{'} + \frac{1}{2}O_2(g) \quad (2.2)$$

Eqn (2.1), which represents the vacancy formation reaction, is written using Kröger–Vink defect notation in eqn (2.2), where $Ce_{Ce}^{\times}$ represents a $Ce^{4+}$ ion on a Ce lattice site, $O_o^{\times}$ represents an $O^{2-}$ ion on an O lattice site, $Ce_{Ce}^{'}$ represents a $Ce^{3+}$ ion on a Ce lattice site and $V_o^{\bullet\bullet}$ represents a neutral oxygen vacancy site.

 

The formation of an oxygen vacancy results in a decrease in the coordination number of $Ce^{4+}$ to $O^{2-}$ ions and introduces $Ce^{3+}$ ions into the crystal lattice, as shown in Fig. 2b. $Ce^{3+}$ ions have a larger ionic radius (1.034 Å) as compared to $Ce^{4+}$ ions (0.92 Å).[18] Therefore, the introduction of $Ce^{3+}$ ions and oxygen vacancies results in a distortion (dislocation of atoms from their equilibrium lattice points) of the local symmetry and generates strain in the lattice. Ceria particles release strain by undergoing lattice expansion,[19,20] as shown in Fig. 2b. Different distortions can be induced due to different $Ce^{3+}$ localization motifs with correspondingly different vacancy formation energies. The localization of electrons upon vacancy formation occurs either on the cerium ions neighboring the vacancy (*i.e.*, Ce–O) or cerium ions next to the nearest neighbor (*i.e.*, Ce–Ce).[21,22]

**2.1.1. Oxygen vacancies.** Oxygen vacancy defects can be categorized into surface (present on the surface) and subsurface oxygen vacancies (present in the bulk) depending on their location.[23,24] Oxygen vacancies can either be isolated (single oxygen vacancy) or form clusters. Vacancy clusters of different shapes including triangular, dimers and straight lines have been reported.[25,26] Scanning tunneling microscopy (STM) provides the most visually convincing demonstrations of clusters of oxygen vacancies. Clusters of oxygen vacancies like linear surface vacancy clusters (LSVCs) are more favorable for the migration of oxygen in ceria that happens through a vacancy hopping mechanism. The STM images showed that one subsurface vacancy per LSVC is necessary.[24] This structural requirement reveals the high reduction tendency of cerium ion upon the liberation of an oxygen ion.

Yang *et al.* reported vacancy formation energies of 3.39 and 3.21 eV for surface and subsurface oxygen vacancies, respectively, on a (111) surface, implying that the energies for the formation of surface and subsurface vacancies are relatively close to each other.[27] Using state-of-the-art STM as well as DFT calculations, Esch and co-workers showed in an elegant study that the surface oxygen vacancies on the (111) ceria surface are immobile at room temperature and that direct diffusion (movement of lattice oxygen) needs higher temperatures ($>400$ °C).[24] Note that with increasing annealing time, the number of surface defects should decrease due to the small diffusion barrier, making it highly mobile at the elevated temperatures, in which the clustering of surface vacancies is energetically unfavorable.[28]

Fig. 3a and b show the two types of vacancies, namely, surface and subsurface oxygen vacancies, identified on a partially reduced ceria surface in filled-state and empty-state, respectively. Both types of vacancies were present with similar coverages. This observation was indeed in line with DFT calculations, which predicted the same vacancy formation energy for both the defects, as shown in Fig. 3c. Furthermore, on a fully reduced ceria surface, three configurations of surface vacancies were identified: single surface or subsurface vacancies, vacancy dimers and vacancy trimers. The structural models of dimers and trimers of oxygen vacancies are summarized in Fig. 3d. The superposition of single surface and

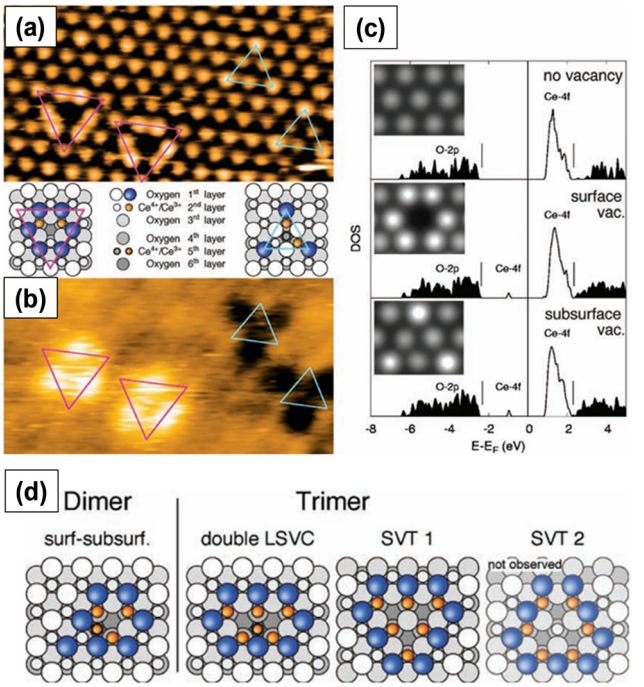


Fig. 3 STM images of surface and subsurface oxygen vacancies in (a) filled-state and (b) empty-state. Pink and blue triangles represent surface and subsurface vacancies, respectively. (c) Density of states (DOS) calculations along with STM images in filled-state (inset). Structures of the observed vacancy dimers and trimers. Reprinted with permission from ref. 24.

subsurface vacancies results in the formation of a vacancy dimer. Double LSVCs form after the removal of another surface oxygen atom. Two possible variations of vacancy trimers, of which only the one that exposes $Ce^{3+}$ ions (SVT 1 in Fig. 3d), was observed.

Both surface and subsurface oxygen vacancies on a partially reduced (111) ceria surface were observed by several other researchers.[29–31] Oxygen vacancies are located at the third surface atomic layer. When the concentration of subsurface oxygen vacancies is very high, the defects form arrays with a propensity to form linear motifs.[29] The oxygen vacancies initially form triangular clusters and upon annealing form line defects. The clustering of oxygen vacancy defects on ceria surface is energetically more favorable than the formation of isolated surface oxygen vacancy defects.[30]

**2.1.2. Non-stoichiometric oxides of ceria and their structural properties.** In reducing atmospheres (low oxygen pressures) and at elevated temperatures, ceria forms a continuum of oxygen deficient nonstoichiometric oxides with composition $CeO_{2-x}$, where $0 < x \leq 0.5$,[32] as shown in eqn (2.3). The actual reduction limit of nonstoichiometric ceria is $Ce_2O_3$ (*i.e.*, when $x = 0.5$), where all cerium ions in the unit cell are in 3+ oxidation state.

$$CeO_2 \leftrightarrow CeO_{2-x} + \frac{x}{2}O_2(g) \qquad (2.3)$$

Different types of $CeO_{2-x}$ oxide phases are identified in the literature. However, some conflicting results exist on the

structures and compositions of intermediate phases. The traditional powder X-ray diffraction (XRD) method has limitations in determining the structural characteristics of nonstoichiometric oxides.[3] Due to the low X-ray scattering power of O atoms, it is difficult to obtain the detailed sublattice structure of O from the XRD technique.[13] Thus, neutron and electron diffraction techniques have been employed to overcome the limitations of the XRD technique.[33,34]

The so-called α-phase non-stoichiometric oxides have compositions in the range of $0 < x < 0.286$ for $CeO_{2-x}$ ($CeO_{1.714}$–$CeO_2$). The α-phase shows a disordered nonstoichiometric fluorite-related structure that is stable at high temperatures (above 685 °C). The XRD patterns obtained at high temperatures do not show superstructures and the lattice parameter of the cubic phase increases with $x$.[34] At lower temperatures, however, the α-phase transforms into a series of fluorite related phases described by the general formula $Ce_nO_{2n-2m}$. The lattice parameters at low temperatures are close to those reported for α-phase, although the α-phase is disordered and low temperature phases show structural changes.[35–37] This implies that variation in oxygen partial pressure and temperature does not alter the positions of cerium ions and that the change in symmetry arising due to the reduction of ceria is primarily due to the formation of oxygen vacancies. Some examples of these phases are $Ce_{10}O_{18}$ (the ε phase), $Ce_6O_{11}$ (the β phase, monoclinic) and $Ce_{11}O_{20}$ (the δ phase, triclinic).[37,38]

The $CeO_{2-x}$ oxides with the composition $x > 0.286$ at high temperature are dominated by the σ-phase, a nonstoichiometric phase with body-centered cubic crystal structure. The C-type sesquioxide ($Ce_2O_3$), end member of the σ-phase, shows bixbyite crystal structure (space group *Ia*3).[35] The structures of $CeO_2$ and $Ce_2O_3$ are closely related in that their cerium ion arrays are almost identical and oxygen ions occupy tetrahedral positions in both cases. The oxygen ions occupy all available locations in the fluorite structure while only three-quarters are occupied in the bixbyite structure.[19,36] As a result, the lattice parameter of $Ce_2O_3$ is almost twice that of $CeO_2$. The nonstoichiometric σ-phase is very difficult to distinguish from the C-type sesquioxide.

### 2.2. Crystal plane and shape-dependent properties

The reactivity of ceria-based materials is significantly affected by the morphology, oxidation states and the exposed crystal planes.[39–41] In this section, we will discuss the three thermodynamically stable low-index crystallographic planes of ceria, namely (100), (110) and (111),[42–44] as shown in Fig. 4a–c. Some of the important characteristics of these three crystal planes are summarized in Table 1. Other ceria surfaces like (211), (210) and (310) are less stable and suffer severe reconstruction.[40] The (110) surface is a type 1 surface that exposes both cerium and oxygen ions, and each layer has zero charge as the anions and cations are present in stoichiometric proportions in each plane (six coordinate cerium ions and three coordinate oxygen ions).[45,46] The (111) ceria surface is a type 2 surface, which is terminated with oxygen ions. There is no net dipole moment as the three O–Ce–O layers (stacked one on top of the other) maintain charge neutrality. The coordination number is three and seven for oxygen and cerium, respectively.[44] The (100) surface of ceria is a type 3 surface, which is intricate because an ideal surface could have either oxygen or cerium ions in the top surface, thereby leading to a polar and unstable surface.[46] Oxygen and cerium have coordination numbers of two and six, respectively.

The structures and stabilities of the three low-index lattice planes of ceria have been extensively investigated by many researchers. Although the results vary, the stability generally follows the order (111) > (110) > (100).[27,47] Vacancies are the active sites for oxygen activation in oxidation reactions in many catalytic applications. (110) and (111) ceria surfaces have the lowest and highest vacancy formation energies, respectively. The (111) surface is less prone to accommodate a vacancy and hence the energy needed for vacancy formation on its surface is the highest among the three.[47] The subsurface vacancy site is the most stable vacancy on the (111) surface.[48] In (110) surface, the vacancy with one $Ce^{3+}$ ion in both the surface and first subsurface layers is determined to be the most stable. In (100) surface, two $Ce^{3+}$ ions neighboring the vacancy site are the most stable; the next most stable site is 0.30 eV higher in energy.[22] In case of (110) and (100) ceria surfaces, for the same oxygen vacancy, more than one distribution of $Ce^{3+}$ sites are observed.

The morphology and crystal plane of ceria can be affected by the synthesis method and the cerium precursor salt.[49–53] Ceria with well-defined lattice planes and morphologies can be obtained by modulating some of the critical synthesis parameters. Synthesis of ceria nanomaterials with different shapes like cube, octahedron, tetrahedron, sphere, rod and plate have been reported in the literature. The most widely employed synthesis procedure to produce ceria in industrial applications is by chemical precipitation, which results in the formation of NPs. Factors like pH, base concentration, reaction temperature and time affect the physicochemical properties of NPs including the shape and size.[54–58] Facet engineering can be used as a powerful tool to enhance the modification of CeNPs, for example, silanization through the favorable adsorption of tetraethyl orthosilicate (TEOS) on the (100) facets and spontaneous breakage of the Si–O bonds of TEOS as the rate determining step for silanization.[59]

Among various other methods, the hydrothermal process has been used to prepare different ceria nanoshapes. Mai and collaborators showed that ceria nanocubes, nanorods and nanopolyhedra can be selectively synthesized by varying the base concentration and temperature during hydrothermal synthesis. First, anisotropic $Ce(OH)_3$ nuclei form from the reaction of $Ce^{3+}$ precursor ions with the base (NaOH). At low base concentration (0.01 mol $L^{-1}$) and temperature of 100 °C, the rate of dissolution/recrystallization is very low. Consequently, the driving force for the anisotropic growth of $Ce(OH)_3$ nuclei is also low, and hence, nanopolyhedra exposing (111) and (100) crystal planes are formed. At a much higher base concentration (6 mol $L^{-1}$) and 100 °C temperature, the dissolution/recrystallization rate is enhanced. $Ce(OH)_3$ nuclei

 

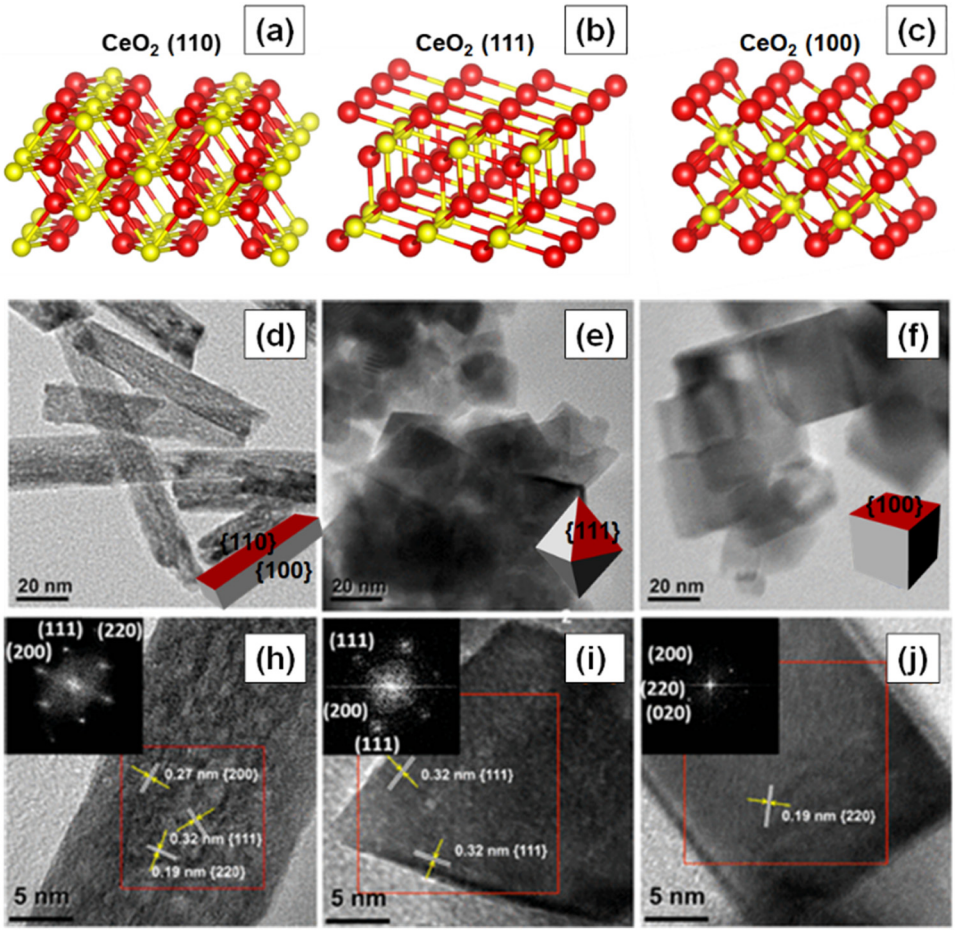


Fig. 4 Atomic structures of the three low index crystal planes of ceria. (a) 110, (b) 111, and (c) 100. Red and yellow-colored spheres represent $O^{-}$- and $Ce^{4+}$ ions, respectively. TEM and HRTEM images of the three different ceria nanoshapes (d) and (h) nanorods, (e) and (i) nanooctahedra and (f) and (j) nanocubes. Fourier transform patterns of the selected areas of the samples are shown in the insets of HRTEM images. Fig. 4d–j reprinted with permission from ref. 39. Copyright 2018 American Chemical Society.

Table 1 Properties (coordination number and oxygen vacancy formation energy) of low-index crystallographic planes of ceria

| Property/crystallographic plane | (110) | (111) | (100) |
|---|---|---|---|
| Coordination number | Ce(6)<br>O(3) | Ce(7)<br>O(3) | Ce(6)<br>O(2) |
| Atom/s exposed by first layer | Ce and O | O | O |
| Relaxed surface energy (eV) | 1.01 | 0.68 | 1.41 |
| Unrelaxed surface energy (eV) (estimated from DFT calculations) | 1.26 | 0.69 | 2.05 |
| Oxygen vacancy formation energy (eV) (calculated from DFT corrected for on-site Coulomb interactions) | 1.99 | 2.6 | 2.27 |

grow anisotropically to form nanorods exposing (110) and (100) surfaces. The increase in synthesis temperature to 180 °C led to the oxidation of $Ce(OH)_3$ to $CeO_2$ and nanocubes exposing (100) planes were formed. Besides NaOH, $PO_4^{3-}$, urea and $H_2O_2$ can also be used for the hydrothermal synthesis of ceria nanomaterials.[60–65]

Surfactant- or organic-assisted synthesis, with organic molecules used as coating agents, are often used to control the particle growth as the organic material adsorbs on specific planes of nanocrystals and directs the oriented growth. As mentioned above, the concentration of surfactant and cerium precursor salt, reaction temperature and time are some of the crucial factors that affect the morphology of ceria nanomaterials.[66–70] Pan *et al.* used a surfactant-assisted method to synthesize nanorods, nanoplates and nanotubes[52] using cetyltrimethylammonium bromide (CTAB). $CTA^{+}$ adsorbs on ceria nanocrystals and interacts with the (111) and (100) facets. The exposed surfaces couple to reduce the surface energy to form nanoplates. Due to the low coating ability at lower CTAB concentrations, nanoplates are transformed into nanorods to lower the surface energy by an anisotropic growth mechanism. At high CTAB concentrations, the nanoplates

transform into nanotubes due to a rolling mechanism. Sometimes, the combination of different organic molecules can also be used to selectively fabricate ceria nanomaterials with specific shapes. For example, the addition of oleic acid (OA) as a co-surfactant to a solution of $Ce(NO_3)_3$ and diphenyl ether in oleylamine at 320 °C in the sol–gel synthesis method led to the generation of nanowires and tadpole-shaped ceria nanocrystals due to the anisotropic growth of the nuclei.[71]

Surfactants or surface coating agents play an important role in the synthesis and later dictate the properties of the CeNPs. For instance, nanospheres were obtained using diethylene glycol as the reaction solvent and polyvinylpyrrolidone (PVP) as the surfactant, but when the synthesis was carried out in the absence of PVP, agglomerated and irregular shaped nanoparticles were obtained.[72] The charge of the surfactant can affect the morphology and the stability of ceria nanomaterials and should be considered. Anionic surfactants can adsorb on the positively charged ceria and effectively stabilize them while cationic surfactants repel away from cerium cations and result in the agglomeration of nanocrystals. The ceria nanomaterials prepared by surfactant-assisted synthesis usually have good dispersibility and uniform size distribution. This technique can be employed to fabricate different shapes ceria, which cannot be obtained using the conventional methods. Nonetheless, the use of organic solvents and surfactants can results in impurities and depending of the solvent and surfactant used can increase the manufacturing costs. The effect of other synthesis methods on different ceria nanoshapes and the associated formation mechanisms are presented in several comprehensive reviews, and the readers can refer to them for additional information.[73–75] The anions of the cerium precursor salt can selectively interact with specific crystal planes and hence form nanocrystals with different morphologies. The $Br^-$, $I^-$, $Cl^-$ and $SO_4^{2-}$ counter anions of cerium precursor salt form nanorods, whereas $NO_3^-$ and $BrO_3^-$ anions lead to the formation of nanocubes and NPs, respectively.[50] The anisotropic growth of $Ce(OH)_3$ nuclei formed by $Br^-$, $I^-$, $Cl^-$ and $SO_4^{2-}$ results in nanorod formation. In the presence of $NO_3^-$ and $BrO_3^-$, $CeO_2$ nuclei are formed due to the oxidizing ability of these anions, and the growth of isotropic $CeO_2$ nuclei results in the formation of nanocubes/NPs. $CeCl_3$ precursor salt exposes (100) and (110) planes due to the formation of nanorods while $Ce(NO_3)_3$ exposes (100) planes due to the formation of nanocubes.[51]

The shape of nanoceria can also affect the concentration of oxygen vacancy defects and hence their reactivity. Numerous studies have indeed investigated the effect of shape on vacancy concentration and catalytic activity. For instance, Cao and collaborators studied the effect of shape or crystal plane on the catalytic activity of ceria for CO oxidation.[39] Different morphologies, *e.g.*, nanorods, nanooctahedra and nanocubes, with all having similar crystallite sizes were synthesized. The high-resolution transmission electron microscopy (HRTEM) images of the synthesized ceria nanoshapes are shown in Fig. 4d–j. The ceria nanocubes and nanorods exposed (100) crystal plane while the nanooctahedra exposed (111) crystal plane. The concentration of $Ce^{3+}$ ions, however, was similar in all three nanoshapes. Electron paramagnetic resonance (EPR) spectra suggested the presence of isolated vacancies on the (100) facets of ceria nanorods and nanocubes and vacancy clusters on the (111) facets of ceria octahedra. Furthermore, the type of oxygen vacancies and surface properties of ceria nanoshapes were correlated to their catalytic activity.

Ceria octahedra expose eight (111) planes while ceria cubes expose six (100) planes. Ceria nanorods expose (100) and (110) surfaces.[76] The reactivity of different facets, as determined by theoretical calculations, follows the order (110) > (100) > (111).[1,77,78] This order, in fact, is in agreement with the experimental results on the activity of different crystal planes of ceria. Nevertheless, different vacancy formation energies in a given surface can be obtained, which is due to some of the limitations of techniques used for theoretical calculations, discussed in detail elsewhere.[1,44]

### 2.3. Size impact on the reactivity and catalytic activity properties

Particle size has a significant impact on the reactivity and catalytic activity of ceria nanomaterials. The effect of particle size was first experimentally probed by Tsunekawa's group. In a series of publications, they showed that the lattice parameter (calculated from electron diffraction patterns) increases with the decrease in the particle size from 6.7 to 2.1 nm.[18,19] Three possible models were proposed to explain the increase in the lattice parameter value based on the fact that oxygen forms peroxide, $O_2^{2-}$, and superoxide, $O_2^-$, on the surface of reduced $CeO_2$. One model suggests that CeNPs consist of a layer of $Ce_2O_3$ with an estimated thickness of 0.561 nm on the outside while the core is $CeO_2$. Several studies also observed size-induced lattice expansion in CeNPs, particularly for sizes below 20 nm, due to the increase in the oxygen vacancies and $Ce^{3+}$.

Wu *et al.* determined the concentration of $Ce^{3+}$ as a function of particle size using electron energy loss spectroscopy (EELS).[79] The fraction of $Ce^{3+}$ ions rapidly increased with decreasing particle size below 15 nm. Interestingly, their EELS spectra revealed completely reduced ceria, $Ce_2O_3$, at a diameter of 3 nm. This reduced ceria was found to have a fluorite structure like that of bulk $CeO_2$. Also, the EELS spectra acquired from the edge and the center of the particles showed that for larger particles, the reduction of $Ce^{4+}$ to $Ce^{3+}$ happens mainly at the surface, resulting in a $Ce_2O_3$ surface layer but leaving the core as $CeO_2$. Hailstone and collaborators studied the size-dependent lattice expansion of colloidal ceria NPs using TEM.[80] The lattice constant increased with a decrease in particle size, with 1.1 and 11.8 nm particles having values of 0.578 and 0.547 nm, respectively. The corresponding lattice expansion was found to be about 6.8% and 1.1% for 1.1 and 11.8 nm CeNPs, respectively. The diffraction patterns for all the three different-sized particles were found to be consistent with that of the fluorite crystal structure of $CeO_2$ and not with the predicted cubic or the hexagonal structure of $Ce_2O_3$. Most of the surface ions were $Ce^{3+}$ and, correspondingly, there were substantial oxygen vacancies. The larger radius of $Ce^{3+}$ along with the

 

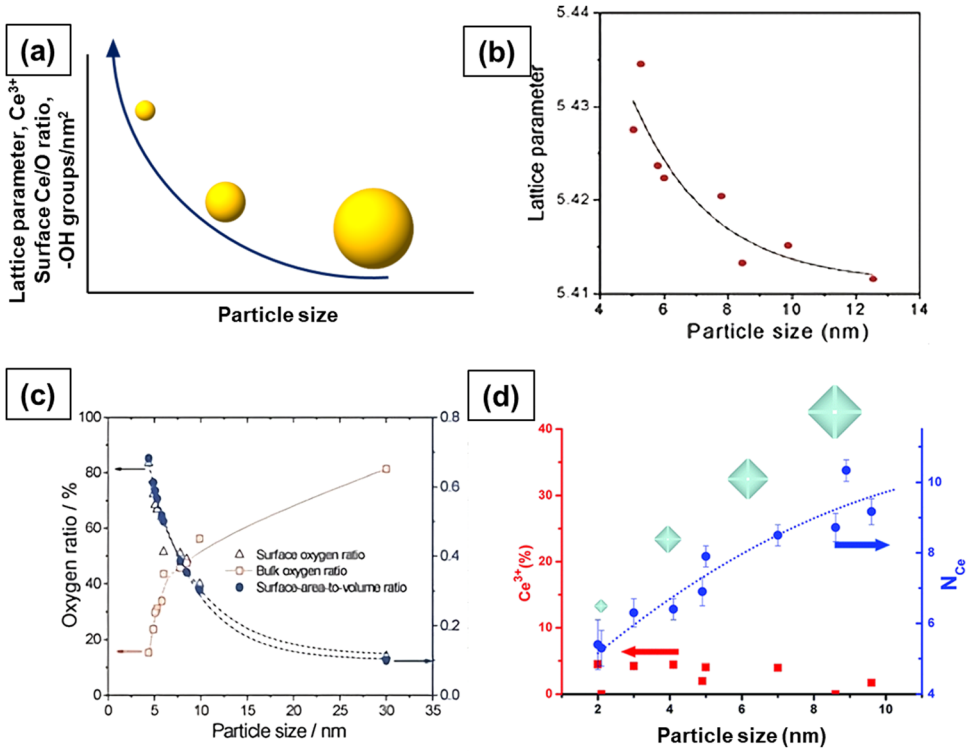


Fig. 5 (a) Effect of particle size on lattice parameter, concentration of $Ce^{3+}$, oxygen vacancies and hydroxyl species. More and more oxygen vacancies form with decrease in size and this leads to an increase in the concentration of $Ce^{3+}$ ions and lattice parameter. (b) Increase in lattice parameter with the decrease in size. (c) The concentration of surface oxygen and bulk oxygen as a function of particle size. (d) Concentration of $Ce^{3+}$ and Ce–Ce coordination as a function of particle size. Fig. 5b and c reproduced from ref. 81 with permission from the Royal Society of Chemistry. Fig. 5d reprinted with permission from ref. 83. Copyright 2012 American Chemical Society.

associated oxygen vacancies corroborate the higher lattice constant and hence the greater lattice expansion observed for smaller particles.

As the size of ceria NP decreases, more and more oxygen vacancies are formed and hence the concentration of $Ce^{3+}$ increases, as shown in Fig. 5a. Since $Ce^{3+}$ ions have a larger ionic radius than $Ce^{4+}$ ions, the particle size reduction leads to lattice distortion and introduces strain in the lattice. This strain is liberated after lattice expansion; therefore, the lattice parameter increases (Fig. 5a).[4,6,8,16,17,19] Xu *et al.* studied the size-dependent structural, chemical and electronic properties of ceria.[81] The lattice parameter increased with the decrease in particle size, as shown in Fig. 5b, but their results did not provide any proof of increase in $Ce^{3+}$ concentration and oxygen vacancies. Nonetheless, a dramatic increase in the concentration of reducible oxygen was observed at sizes below 5 nm due to peroxide formation on ceria surface. It is now established that the CeNP size influences the degree of hydroxylation and hydroxyl stability, with particles $<5$ nm having a higher density of more thermally stable hydroxyl groups, as compared to larger particles.[82] These functional groups dictate the surface reactions and the behavior of the CeNPs in aqueous environments, which is relevant for many processes, *e.g.*, pro- or antioxidant activity and surface sorption. This also suggests that, beyond the varying $Ce^{3+}/Ce^{4+}$ ratios, the surface hydroxyl groups also play a critical role in the CeNP reactivity.

The surface oxygen concentration varies inversely with the bulk oxygen concentration as a function of particle size, as shown in Fig. 5c. The concentration of surface oxygen increases at the expense of the concentration of bulk oxygen. It is likely that the significant increase in the concentration of reducible/surface oxygen is due to the increased $Ce^{3+}$ concentration as $Ce^{3+}$ ions interact with $O_2$ and form cerium superoxide ($Ce^{4+}O_2^-$). A decrease in particle size leads to increased $Ce^{3+}$ species and hence a higher concentration of $Ce^{4+}O_2^-$ species. The formation of cerium superoxide ($Ce^{4+}O_2^-$) and cerium peroxide ($Ce^{3+}O_2^{2-}$) species will be discussed in Section 2.6. The size-dependent lattice parameter and relative $Ce^{3+}$ concentration values of ceria particles reported by several published studies are summarized in Table 2.

Vayssilov *et al.* showed that 2 nm ceria particles prepared by thermal evaporation contained only 2% $Ce^{3+}$.[90] Using X-ray absorption near edge structure spectroscopy (XANES), Nachimuthu *et al.* estimated that the concentration of $Ce^{3+}$ ions was very low ($<5\%$) even for 2 nm ceria particles.[91] Paun *et al.* studied the size-dependent properties of ceria particles using TEM, XRD, X-ray spectroscopy (XPS), extended X-ray absorption fine structure (EXAFS) and XANES.[83] These analyses revealed that the $Ce^{3+}$ concentration does not vary with size under ambient conditions although the lattice parameter increases with the decrease in particle size. As can be seen in Fig. 5d, the $Ce^{3+}$ concentration remained at the same $\sim 4\%$ value with the

Table 2 Size-dependent relative $Ce^{3+}$ concentration and lattice parameter values of ceria particles from different studies

| Particle size range (nm) | [$Ce^{3+}$] range (%) | Preparation method | Lattice parameter range (nm) | Ref. |
|---|---|---|---|---|
| 2–7 | 17.3–42.5 | Hydrothermal | 0.5453–0.5560 | 18 and 19 |
| 4–60 | — | Precipitation (semi-batch reactor) | 0.5401–0.5419 | 84 |
| 3–20 | — | Thermal evaporation | 0.5402–0.5615 | 79 |
| 6–15 | — | Precipitation | 0.5413–0.5433 | 85 |
| 1–12 | — | Precipitation | 0.547–0.578 | 80 |
| 4–10 | 29.4–29.5 | Microemulsion | 0.5415–0.5435 | 81 |
| 3–30 | 17–44 | Precipitation | 0.548–0.560 | 17 |
| 10–90 | 15–26.3 | Precipitation | — | 86 |
| 10–235 | 19.3–27.6 | Supercritical solvothermal | 0.5406–0.5425 | 87 |
| ~10 | 34 | Green synthesis | — | 88 |
| Bulk | — | — | 0.5403 | 89 |

decrease in particle size from 8 nm to 2 nm. This value of 4% is way lower than that reported in other studies, which are in the range of 20–30% for about the same particle size. The presence of $Ce^{3+}$ ions in traces was attributed to the use of $Ce^{3+}$ precursors used for synthesis.

While most studies reported lattice expansion in the range of 0.1–0.5% for particles smaller than 5 nm, Tsunekawa *et al.*[19] and Wu *et al.*[79] observed lattice expansion in the range of 2–3.5% for similar particle sizes. Hailstone and collaborators reported a very high lattice expansion of 7% for 1 nm CeNPs.[80] These dramatic differences in lattice expansion is potentially attributed to the effect of surface stabilizers used in the synthesis to control the particle growth. Another aspect that is worth highlighting is the relative $Ce^{3+}$ concentration. Majority of the studies reported $Ce^{3+}$ concentrations greater than 15% for particles smaller than 5 nm. Nevertheless, a few studies reported very low (<5%) relative $Ce^{3+}$ concentration values for particles smaller than 5 nm. These apparent differences could be due to variations in the preparation method, synthesis conditions, surface coating agents, or the characterization method employed to estimate $Ce^{3+}$ concentration. A thorough knowledge of the particle synthesis chemistry is necessary to understand the effect of synthesis method on $Ce^{3+}$ concentration. In this regard, it is critical to create standards for the synthesis method and the determination of relative $Ce^{3+}$ concentration.

The size-dependent oxygen vacancy formation energies in $(CeO_2)_n$ with n values in the range of 20–140 was investigated using DFT calculations.[92–94] The removal of a low-coordinate O atom from ceria needs the least energy, consistent with the results reported for other metal oxides. The removal of such O atoms from nanosized particles is more favored than that from the extended surfaces. The increase in particle size is associated with a marked decrease in the oxygen vacancy formation energy, indicating that this energy reaches a minimum at certain sizes. The size dependence of the oxygen vacancy formation energy is controlled by electrostatics. The bandwidth of the unoccupied density of states projected on to the cerium 4f orbital levels is a crucial factor that affects the energy of vacancy formation. The presence of corner cerium atoms is identified as the structural pattern necessary for a significant reduction of vacancy formation energy.

By summarizing these results, the following conclusions can be drawn. (1) With a decrease in particle size, more and more oxygen vacancies are formed and, consequently, the $Ce^{3+}$ concentration is enhanced. (2) An increase in $Ce^{3+}$ concentration increases the lattice parameter due to the lattice expansion as $Ce^{3+}$ ions have higher ionic radius than $Ce^{4+}$ ions. (3) Most of these changes (formation of oxygen vacancies and generation of $Ce^{3+}$ ions) occur on the surface. As a result, the surface is very similar to that of $Ce_2O_3$ while the bulk remains as $CeO_2$. When the particle size decreases to about a nanometer or two, the particle transforms from $CeO_2$ to $Ce_2O_3$, as shown by several studies, and the particle mostly consists of $Ce^{3+}$ ions. The conversion from $CeO_2$ to $Ce_2O_3$ C-type sesquioxide does not require a change in the crystal structure. Hence, in some studies, even ~1–2 nm particles showed fluorite structure as the C-type is a combination of three types of fluorite like unit cells. (4) The oxygen vacancy formation is thermodynamically more favorable on CeNP' surfaces than in the bulk. (5) The corresponding formation energies of the $Ce^{3+}$ ions are also lower on the nanoceria surfaces than in the bulk. Clearly, these findings suggest that the concentration of surface $Ce^{3+}$ ions, the surface functional groups and the associated oxygen vacancies and, hence, the reactivity of NPs increases with a decrease in particle size, while the oxygen vacancy formation energy diminishes markedly.

### 2.4. Modification by doping

Due to the increased surface area to volume ratio and relative ease of vacancy defect formation, CeNPs show enhanced reactivity and outstanding catalytic activities enabling their use in many commercial applications. However, pure CeNPs are associated with some drawbacks like the deactivation of OSC and catalytic activity and a loss of surface reactivity due to thermal sintering at high temperatures, which limit their use in some commercial applications.[95,96] It is, therefore, of interest to modify the properties of CeNPs and alter the surface energies to facilitate their use in such applications. Any chemical modification or doping of CeNPs involving an increase in the concentration of oxygen vacancies should in principle increase their reactivity. This is true only if (a) the chemical modification process does not lead to a significant reduction in the concentration of active redox species and (b) the defects formed at

 

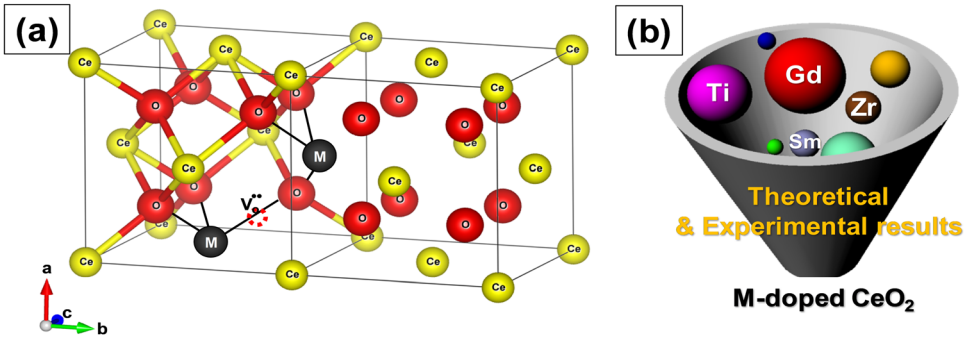


Fig. 6 (a) Schematic of the crystal structure of ceria with metal ion dopant M. Addition of dopants (rare earth, transition or noble metal ions) during synthesis results in the formation of oxygen vacancies. (b) Development strategy for ceria with metal ion dopant M.



high degrees of reduction do not cluster, making ion transport difficult.

One of the important strategies to overcome these limitations is to incorporate other metal ions into the crystal structure of CeNPs by doping. The addition of dopants results in higher resistance to sintering at elevated temperatures and an enhancement of reducibility and OSC of CeNPs and therefore improves the overall catalytic performance.[97,98] The concept of modifying CeNPs by doping with foreign materials indeed led to enhanced thermal stability and improved catalytic activity. In a typical doping process, cerium atoms in the crystal lattice are replaced with noble metals, transition metals or rare earth metals.

Doping is done during synthesis and the dopants substitute $Ce^{4+}$. The result is that oxygen vacancies are introduced in the crystal structure of ceria for charge compensation,[99] as shown in Fig. 6a. Doped CeNPs show very high oxygen mobility through a vacancy diffusion mechanism and hence high ionic conductivity.[100,101] Given the importance of oxygen vacancy defects of CeNPs in many applications, this topic has garnered a lot of attention. Most reported works explored the use of rare earth ($Y^{3+}$, $Gd^{3+}$, $Sc^{3+}$, $Sm^{3+}$, $Er^{3+}$, $Eu^{3+}$, $La^{3+}$, *etc.*), noble (Pt, Pd, Au, and Rh) and transition metals (Cu, Co, Ni, Mn, Zr, Zn, Fe, *etc.*) as dopant materials to modify the physicochemical properties of CeNPs (Fig. 6b). The dopants are further categorized into two types, isovalent and aliovalent, based on their oxidation state.[102,103] Isovalent dopants are the ones that have a 4+ oxidation state (same as that of the host $Ce^{4+}$), while aliovalent dopants have an oxidation state that is different from that of the host. The substitution of $Ce^{4+}$ with the isovalent dopants in the crystal lattice of ceria introduces intrinsic oxygen vacancies and reduces the oxygen vacancy formation energy because of structural distortion.[72] On the other hand, substitution with aliovalent dopants incorporates both extrinsic and intrinsic defects and reduces vacancy formation energy due to structural distortion and electronic modifications.

**2.4.1. Doping with rare-earth metals.** Rare earth-doped CeNPs are attractive candidates for many industrial oxidation reactions, biomedical and biosensing applications and electrodes in solid oxide fuel cells (SOFCs). The introduction of oxygen vacancies upon doping ceria with rare-earth ions can be represented as follows in Kröger–Vink defect notation (eqn (2.4))

$$Re_2O_3 + 2Ce_{Ce}^{\times} + O_O^{\times} \rightarrow V_o^{\bullet\bullet} + 2Re_{Ce}^{'} + 2CeO_2 \qquad (2.4)$$

where $Re_{Ce}^{'}$ represents a $Re^{3+}$ ion on a Ce lattice site.

The increase in the concentration of Gd from 0 to 15% increased the OSC of CeNPs but with a further increase, the OSC decreased.[104] The enhanced OSC was attributed to the increased specific surface area and decreased particle size. In contrast, Hennings *et al.* reported that the OSC decreased after with Gd.[105] Nevertheless, the concentration of oxygen vacancies increased with the increase in Gd concentration. They argued that the drop in OSC was due to the replacement of reducible $Ce^{4+}$ by non-reducible $Gd^{3+}$ and the suppressed reduction of $Ce^{4+}$. Trivalent La, Sm, Y and Gd increase the concentration of $Ce^{3+}$ ions on the surface of particles.[106] An increase in $Ce^{3+}$ concentration enhances oxygen vacancies and facilitates the transport of oxygen from the bulk to the surface. La and Pr doping boosted the concentration of surface reducible $Ce^{4+}$ ions and shifted the reduction peak of CeNPs to lower temperatures.[107] It is important to point out that the optimal concentration of dopant required to obtain the maximum increase in the concentration of $Ce^{3+}$ and oxygen vacancies depends upon the type of the dopant. For instance, in one study, it was shown that the optimal concentration of La and Pr was about 5% and 50%, respectively.[108]

Of all RE elements, Pr yields the maximum concentration of oxygen vacancies. In case of Pr doping, the presence of both $Ce^{3+}$ and $Pr^{3+}$ ions increased the concentration of oxygen vacancies due to the reduction of $Pr^{4+}$ to $Pr^{3+}$ and $Ce^{4+}$ to $Ce^{3+}$.[107] Of Nd- and La-doped CeNPs prepared using the microemulsion method, the oxygen vacancy defect concentration was higher for La-doped ceria than for Nd-doped ceria, and this difference was attributed to the larger ionic radius of La as compared to Nd.[109] Y, Sm and Gd doping increased the $Ce^{3+}$ and oxygen vacancy defect concentration while Yb doping reduced it due to the smaller ionic radius of $Yb^{3+}$ as compared to that of the other three ions.[110] Er and Ho also decreased the density of oxygen vacancies due to a similar reason.[111] Using DFT calculations, Kim *et al.* established a trend between the

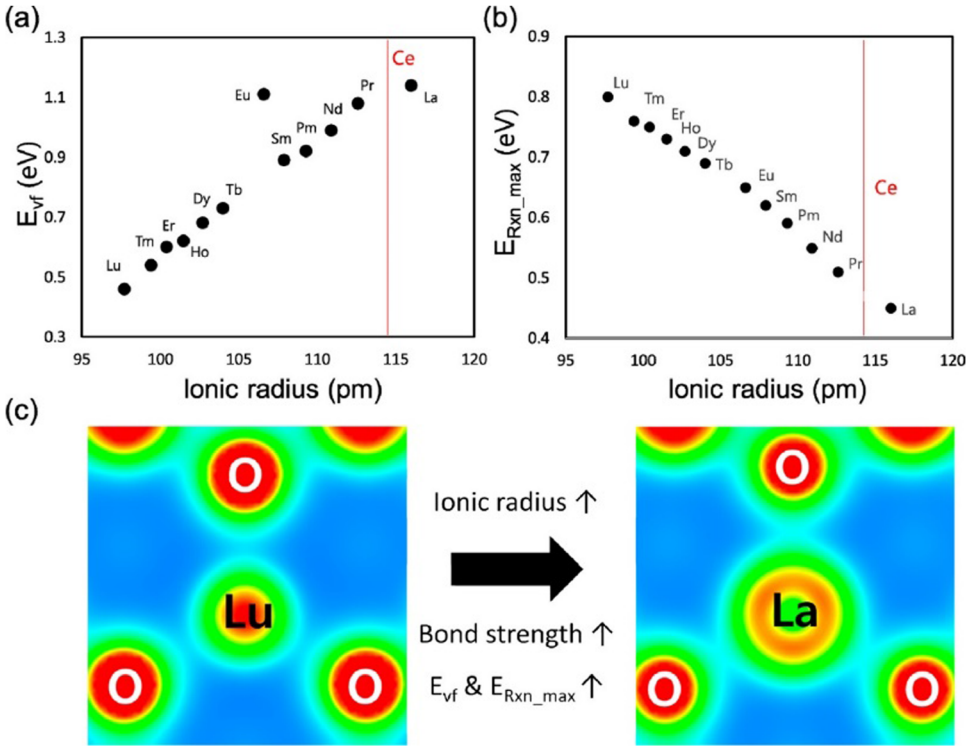


Fig. 7 Relationship between (a) oxygen vacancy formation energy and radius of RE ion and (b) maximum reaction energy and radius of RE ion. (c) Charge density distribution in RE ion having largest ionic radius (La) and with smallest ionic radius (Lu) bonded with O atoms in RE doped ceria. Reprinted from permission from ref. 112. Copyright 2017 American Chemical Society.

radius of the RE metal ion and oxygen vacancy formation energy, which is related to the catalytic activity.[112] The relationship between the oxygen vacancy formation energy and the ionic radius of RE metal, and the highest reaction energy and ionic radius of RE metal ion (Fig. 7a and b) showed an increase in the vacancy formation energy with the ionic radius, whereas the maximum reaction energy (for the case of CO oxidation considered as an example) decreases with the ionic radius. The contribution of the dopant to oxygen vacancy formation energy was also investigated. The ionic radius of the dopant ($R_{ion}$) was also found to influence the RE–O interaction, which in turn altered the oxygen vacancy formation energy ($E_{vf}$), by measuring how easily oxygen vacancies are formed. While most research suggests that doping CeNPs with RE elements typically results in expansion, the radius and coordination number of the dopant ion also play an important role and can lead to variations in RE–O bonds length and different $E_{vf}$. The charge density distribution between RE–O was studied by calculating the RE–O bond strength. The charge of cerium ion in pure $CeO_2$ is 4+ and the ionic radius of $Ce^{4+}$ is 114.3 pm. In contrast, the charge of the other RE elements in $CeO_2$ is 3+ and the ionic radius of the RE ion is relatively smaller than that of $Ce^{4+}$ with La being an exception. As a result, structural stress is induced along RE–O. The stress created by the dopant ion having a smaller ionic radius weakens the strength of the RE–O, as shown in Fig. 7c. Therefore, dopants having a lower ionic radius lead to a lower $E_{vf}$.

Because lanthanide complexes have excellent luminescence, these structures can be widely used in biosensing and bioimaging applications.[113,114] CeNPs show weak emission characteristics that restrict their use in fluorescence-based imaging and sensing. Europium (Eu), one of the rare earth metals, has a strong red light emission upon doping and is considered a suitable dopant to enhance emission in CeNPs as the ionic radius of $Eu^{3+}$ ion (0.1066 Å) is higher than that of $Ce^{4+}$ (0.097 Å) but lower than that of $Ce^{3+}$ (0.1143 Å) and shows excitation from ultraviolet to visible region.[115] Therefore, Eu doping intensifies the photoluminescence properties of CeNPs, opening up many possible opportunities for applications in molecular imaging. The appearance of a broad band in the excitation spectrum of Eu-doped CeNPs is due to the charge-transfer from $O^{2-}$ to $Ce^{4+}$.[116] Both $Ce^{3+}$ and oxygen vacancy concentration increase with an increase in Eu concentration. The conflicting roles of $Ce^{3+}$ ions and oxygen vacancy defects in influencing the photoluminescence response of doped CeNPs have been reported. Kumar *et al.* found that the increase in $Ce^{3+}$ concentration enhanced the photoluminescence properties, whereas an increase in vacancy defect concentration adversely affected the photoluminescence by interfering with the radiative route of emission.[117] Erbium (Er) is another rare-earth element that has been used by several investigators as a dopant to impart fluorescence in ceria particles.[118,119]

Not all trivalent rare-earth metals increase the concentration of $Ce^{3+}$ and oxygen vacancies. An important question that then

 

needs to be answered is what cations can be used for doping ceria particles? Several studies suggested that dopants having ionic radii lesser than that of $Ce^{4+}$ ion can be doped into the ceria lattice. However, this is not always the case as evidenced from many contradictory results reported in the literature.[2,120] When the dopant substitutes a $Ce^{4+}$ ion in the crystal lattice of ceria, the periodic electrostatic field distribution changes due to different electronegativity, oxidation state and ionic radius of the dopant with respect to the Ce ion. The thermodynamics (enthalpy) of dopant incorporation and other thermodynamically relevant factors can be potentially helpful in identifying the right dopant. Computational techniques can also provide some guidance in understanding the thermodynamics of dopant addition to the ceria lattice.

**2.4.2. Doping with transition and noble metals.** Apart from rare earth metals, transition and noble metals were also used to dope CeNPs to enhance their catalytic properties. CeNPs doped with transition metals like Co, Zr, Cu, Fe, Mn, and Cr have good redox ability and can therefore act as active materials for oxidation reactions. The reactivity of these ceria-mixed materials is influenced by various factors like valency of the dopant, catalyst composition, nature and type of the support, as well as the synthesis technique, particle size and shape and crystal structure.

Among composite structures, zirconia-doped ceria (ceria–zirconia) has been studied intensively due to its significance in various industrial catalytic reactions. Ceria forms a substitutional type solid solution with zirconia. When CeNPs are doped with zirconia, the smaller $Zr^{4+}$ ion causes lattice distortion, leading to an increase in oxygen mobility. After introducing $Zr^{4+}$ ions into the crystal lattice of ceria, both Ce–O–Zr and Ce–O–Ce bond lengths in $Ce_xZr_{1-x}O_2$ lattice decrease and oxygen shows a centro-symmetric eight-fold coordination.[121] This change in the local environment of oxygen around $Ce^{4+}$ and $Zr^{4+}$ cations leads to the formation of active oxygen species that plays an important role in the OSC property and therefore its catalytic activity. The reduction of ceria in ceria–zirconia solid solutions can be described by the following chemical reaction.

$$Ce_xZr_{1-x}O_2 + H_2 \leftrightarrow Ce_xZr_{1-x}O_{2-\delta} + H_2O + V_o \quad (2.5)$$

The oxygen nonstoichiometric ($\delta$) value in the above equation changes with composition $x$. The enhanced reducibility is due to the improved oxygen mobility of solid solutions as compared to the pure oxides. The high concentration of oxygen vacancy defects increases the active sites for ionic conduction and provides a high diffusion path through the nanosized grain boundaries that promote fast kinetics.[122,123] The introduction of $Zr^{4+}$ ions in the fluorite crystal structure of ceria decreases the specific surface area at the operating conditions. Nonetheless, the increased thermal resistance to sintering, decreased oxidation enthalpies, higher reduction efficiency and increased OSC of zirconia-doped ceria contribute to the enhanced performance of the ceria–zirconia system in designing a new generation of three-way catalytic converters (TWCs).[124]

Ceria–zirconia catalysts have gradually replaced pure ceria whose properties do not meet the requirements of high conversion efficiency and thermal resistance needed to sustain stringent emission regulations. Additionally, a critical need for more thermally stable materials to improve the performance of TWCs during cold start led to the development of several strategies. Among them, the doping of ceria–zirconia with rare earth elements like La, Pr, Y, Sm and Nd resulted in an increased thermal stability and OSC.[125] The cerium precursor salt was found to have a significant influence on the catalytic properties. The ceria–zirconia catalysts prepared using cerium salt having +4 oxidation state, $(NH_4)_2Ce(NO_3)_6$, was found to have higher $Ce^{3+}$ concentration than those prepared using cerium salt having +3 oxidation state $Ce(NO_3)_3{\cdot}6H_2O$.[126] Also, the catalysts prepared with $Ce^{4+}$ precursor salt had higher Zr concentration and showed improved oxygen mobility than those prepared by the $Ce^{3+}$ precursor. The catalytic activity of ceria–zirconia catalysts is dependent on both the BET surface area and Ce/Zr surface atomic ratio. The Ce/Zr value in turn depends on the synthesis technique and therefore the catalytic activity strongly depends on the preparation method. Thus, the BET surface area of the catalyst prepared using $Ce(NO_3)_3{\cdot}6H_2O$ was higher than that prepared using $(NH_4)_2Ce(NO_3)_6$; the latter showed higher catalytic activity, which was attributed to the higher Zr concentration on its surface.

In other reports, the addition of Cu to the ceria lattice increased its OSC and redox properties by reducing the activation energy for $Ce^{4+}$ reduction, as showed by Hu *et al.*[127,128] Their results showed that the Cu/Ce ratio in the catalyst strongly influenced the catalytic and redox properties. The pore structure and morphology of Cu-doped ceria NPs can be affected by the precursor used for synthesis. $CuCeO_x$ nanofiber catalysts prepared by the electrospinning technique showed higher catalytic activities as compared to those prepared by other conventional methods.[129] The enhanced catalytic activity of nanofibers was ascribed to the large specific surface area and increased concentration of $Ce^{3+}$ ions and oxygen vacancy defects. The doping of CeNPs with Cu also increased the overall surface area and improved the redox properties.

Mn doping into ceria lattice has also shown to increase the concentration of oxygen vacancy defects. XPS analysis of the surface indicated that Ce is present in +4 or +3 oxidation state while Mn exists in +3 or +2 oxidation state.[130] EPR analysis indicated the presence of $Mn^{2+}$ and $Mn^{3+}$ species in the defect sites of the ceria lattice, interstitial spots and on the surface of ceria. Doping with Mn decreased the particle size of calcined CeNP powders and dramatically increased the BET surface area.[131] Impedance spectroscopy measurements have revealed that the Mn ions enter into the solid solution and increased the conductivity by decreasing the apparent activation energy. DRIFTS results showed that a fraction of Mn ions remain segregated on the particle surface. The remarkable enhancement in the catalytic activity of Mn-doped ceria at low temperature is ascribed to the good dispersion of $Mn^{2+}/Mn^{3+}$ ions in the ceria matrix, high OSC, increased redox properties and synergistic interaction between the Mn and Ce. Among

co-precipitation (CP), sol–gel (SG) and hydrothermal methods used to prepare Mn-doped ceria, the catalyst synthesized by the HT method showed very high catalytic activity at low temperature.[131] The larger surface area, increased reducibility, higher concentration of surface adsorbed active oxygen species and an increased number of oxygen vacancy sites are the possible reasons for the enhanced catalytic activity of the mixed catalyst prepared by the hydrothermal method.

In other structures, the presence of $Ni^{3+}$ ions and a very high concentration of oxygen vacancy defect sites in Ni-doped ceria NPs ($Ni_{0.1}Ce_{0.9}O_{2-x}$) has showed an increase in the surface reducibility of these doped structures as compared to pure ceria.[132] Ni-doped ceria showed superior electrochemical properties due to the increased concentration of $Ce^{3+}$, $Ni^{3+}$ and oxygen vacancy defects used to boost faradaic surface redox reactions.[133] Doping with Ni leads to additional structural stress and lattice expansion and extrinsic defects on the particle surface and near grain boundaries. It also results in enhanced surface oxygen reactivity and thus more active reduction sites at their surface. Other reports explored the use of Co to increase the catalytic properties of $CeO_2$ and found the enhanced performance of the Co–$CeO_2$ catalyst as compared to that of bulk $Co_3O_4$ or ceria due to a synergetic effect between Co and $CeO_2$, leading to the increased concentration of oxygen vacancy defects and enhanced reducibility.[134] The preferential exposure of the (112) crystal plane of Co–$CeO_2$, which contained a large concentration of $Co^{3+}$ active sites, was also suggested to be responsible for the higher catalytic activity. The increase in cobalt dopant concentration also increased the band gap energy and reducibility of the catalyst.[135]

Fe doping of ceria enhanced the catalytic activity due to the increased concentration of surface $Ce^{3+}$ and chemisorbed reactive oxygen species.[136] The addition of iron into the crystal lattice of ceria decreased the crystallite size and increased the specific surface area.[137] Fe-doped ceria favors sintering at lower temperatures, enhances the reducibility and increases the number and strength of basic sites.[138] The doping of ceria with iron can also improve the conductivity, decrease the activation energy and enhance the dynamic oxygen storage capacity (DOSC). Therefore, the Fe-doped ceria catalyst showed low temperature activity and increased total oxygen storage capacity (TOSC). It was suggested that the incorporation of Fe into the crystal lattice of ceria strongly modifies the kinetics of oxygen diffusion and enhances the OSC.

Ag, Au, Pt and Pd doping are other suitable approaches to enhance the catalytic activity of CeNPs. The addition of Ag favors the formation of reducible oxygen species that is suggested to be responsible for the improved catalytic activity.[139] The synergistic interaction between Ag and ceria is the key for the low-temperature reduction of ceria.[140] Three different methods used to prepare Pt-doped ceria catalyst resulted in different values of ionic $Pt/Pt^0$ ratios.[141] Furthermore, these three different catalysts were found to achieve varying catalytic activities, increasing with the increasing concentration of ionic Pt species. DFT calculations suggested that the presence of ionic Pt species activated the oxygen atoms on the cerium next to it, resulting in decreased activation energy for dissociative methane adsorption. As a result, the novel square-planar configuration of $PdO_4$ in Pd-doped ceria is shown to be more reactive.[142] The creation of an oxygen vacancy in this structure is energetically more favorable. The structural and chemical attributes of Pd–O–Ce moieties were found to contribute to the higher catalytic activity of Pd-doped ceria.[143] All Ce ions in the crystal are in 4+ oxidation and they are not reduced to 3+ state upon the formation of oxygen vacancies, as evident from the density of electron states, where the filled Ce 4f gap states associated with the reduced ceria are not present. The physicochemical properties of rare earth, transition and noble metal-doped ceria particles are summarized in Fig. 8.

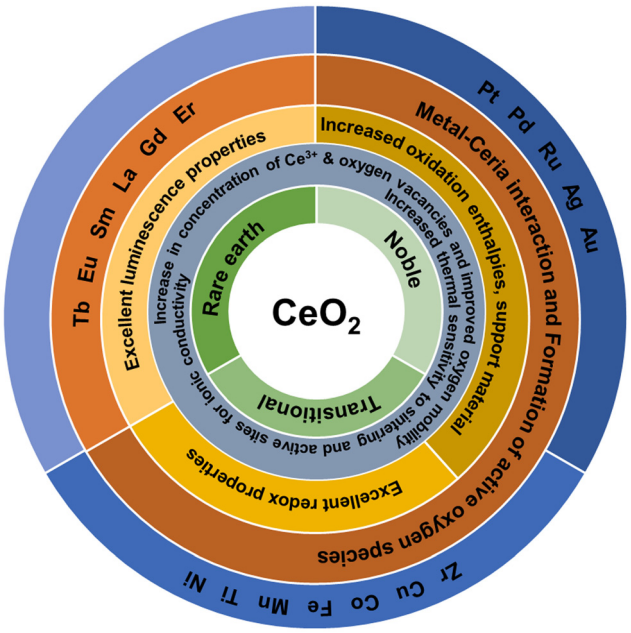


Fig. 8 Schematic of the physicochemical properties of rare earth, noble and transition metal-doped ceria particles used to obtain mixed and doped structures with $CeO_2$.

The improved catalytic activity of doped CeNPs has been generally attributed to an increased concentration of oxygen vacancies and $Ce^{3+}$ and OSC. Other factors like large surface area, improved redox activity, enhanced thermal resistance and the synergistic interaction between the metal and ceria also contribute to the enhanced activity. Almost all transition and noble metals investigated were reported to enhance the catalytic activity. Nevertheless, other factors like the preparation method, concentration of the dopant, type of dopant, oxidation state, and crystal structure also influence the catalytic properties of doped ceria.[144–146]

Experimental studies provide critical information on the characteristics of the catalyst, oxidation reactions, surface processes and its mechanism. The selection of appropriate characterization methods is essential in gaining mechanistic details on important aspects of the ceria's activity such as metal–ceria interactions, role of the dopant, oxygen vacancy defect and surface oxygen species.[125] In addition to

 

experimental tools, theoretical studies based on computer simulations can provide an atomistic understanding of the structure of ceria-based catalysts, the role of dopant, oxygen vacancy defect and $Ce^{3+}$ ions on the catalytic properties of catalysts.

Detailed structural analysis of $Ce_{1-x}Zr_xO_2$ catalyst suggests that the formation of long and short Zr–O bonds in fluorite structure is mainly responsible for enhanced OSC observed for ceria–zirconia.[147–149] The substitution of $Ce^{4+}$ ion with $Zr^{4+}$ increases the reducibility of $Ce^{4+}$ in ceria, although $ZrO_2$ is not a reducible oxide. The addition of reducible ions like $Sn^{4+}$ and $Ti^{4+}$ into the ceria lattice can enhance the OSC of $Ce_{1-x}Sn_xO_2$ and $Ce_{1-x}Ti_xO_2$, respectively. Along with the $Ce^{4+}$/$Ce^{3+}$ couple, the $Sn^{4+}$/$Sn^{2+}$ and $Ti^{4+}$/$Ti^{3+}$ redox couples can also contribute to and therefore increase the reducibility of CeNPs. The coordination around $Ti^{4+}$ or $Sn^{4+}$ ion is different from the fluorite structure of ceria due to the lower ionic radius (0.74 Å for $Ti^{4+}$ and 0.69 Å for $Sn^{4+}$) of these ions as compared to that of $Ce^{4+}$ ion (0.97 Å) and this results in distortion of the ceria lattice.[150–152]

Computational methods were used to study the properties of doped ceria materials.[72,153,154] The distortion of the oxygen sublattice leads to long and short Ce–O and Ti–O, Zr–O, Fe–O, and Zn–O bonds in $CeO_2$–$TiO_2$, $CeO_2$–$ZrO_2$, $CeO_2$–$Fe_2O_3$ and $CeO_2$–$ZnO_2$ solid solutions. The increased reducibility of these materials was explained by weak longer bonds.[155,156] The $Ce^{4+}$ coordination gets distorted to 4+4 type coordination from its ideal 8-fold coordination in these different materials. Transition and noble metal ion doping significantly enhanced the reducibility of $Ce_{1-x}M_xO_{2-\delta}$ (M = Co, Mn, Cu, Ni, Fe, Ru, Pt, and Pd), whereas doping with rare earth metal ions $Ce_{1-x}A_xO_{2-\delta}$ (A = La, Y) was seen to have little effect in increasing the OSC and reducibility of ceria. The optimized structure obtained by computer simulations exhibited a deviation in the bond length of cation–oxygen from the ideal bond length value of 2.34 Å (for Ce–O in $CeO_2$).[155] For instance, simulation results for $Ce_{28}Mn_4O_{62}$ structure showed that the mean Mn–O bond length was 2.0 Å in 4+2 coordination. Doping with other transition and noble metal ions also changed the coordination of $Ce^{4+}$ and formed longer Ce–O bonds. The addition of Pd in $Ce_{1-x}M_xO_{2-\delta}$ (M = Mn Ni, Fe, Cu and Co) resulted in a further increment in OSC; correspondingly, the model calculations revealed a further increment in the bond length. These enhancements have been attributed to the improved reducibility of both the host and dopant ions because of lattice distortion in the presence of the dopant.[72] In the case of rare earth ion doping, the calculations showed a very little increase in bonds lengths from the fluorite structure; therefore, the absence of longer Ce–O and RE–O (rare earth or RE = La and Y) bonds make the resulting structure less susceptible to reduction.[153]

Dopants like Zr, Hf, Ti, Nb and Ta in the (110) ceria surface reduce the oxygen vacancy formation energy.[157] Pentavalent dopants like Nb and Ta in the (110) ceria surface enhance reducibility by charge transfer from the dopant ion to a cerium ion in the surface. The doping of ceria with Pd and Pt also lowers the oxygen vacancy formation energy, attributable to the gap states formed above the valence band and below the empty Ce 4f states.[158] Alfredsson and Catlow compared the adsorption energies of Pt and Pd on (111) zirconia and ceria surfaces using periodic DFT analysis.[159] They found higher adsorption energies for Pt layer (400 kJ $mol^{-1}$) on both ceria and zirconia than Pd layer (200 kJ $mol^{-1}$).

Krcha *et al.* used density functional theory (DFT+*U*) to investigate the structural and electronic effects of transition metal dopants belonging to groups IV–XII in the (111) surface of ceria.[160] The dopant can have an oxidation state anywhere between 3+ and 8 +, and, in such a case, the $Ce^{4+}$ ions are reduced to $Ce^{3+}$ only when the dopant has an oxidation state higher than 4+. Fig. 9a summarizes the oxidation state of dopant in both the completely oxidized and oxygen vacant surfaces. The transition metal ions in groups IV and V change the surface reducibility and the ones in groups X–XII become the reduction center. Metal ions in groups IV and V are associated with their stable oxidation states of 4+ and 5+, respectively, in the oxidized as well as reduced surfaces. Metal ions of groups X–XII are associated with 4+ oxidation state in the oxidized surface and a 2+ oxidation state in the reduced surface. Au, however, is an exception as it has a 3+ oxidation state in the reduced surface. There is no clear trend in metal ions of groups VI through IX. Group metals have a 6+ oxidation state and the metals in the 4th row of groups VII, VIII and IX (Co, Fe and Mn) have a 4+ oxidation state in the oxidized surface and a 3+ oxidation state in the reduced surface. They also showed that the oxygen vacancy formation energy decreases with the group number, as shown in Fig. 9b. The oxygen vacancy formation energies are usually higher when the dopant reduces as compared to only when Ce reduces. Oxygen vacancy formation increases more or less linearly with M–O bond energy, as shown in Fig. 9c.

Structural changes or effects modifying the Ce–O chemical bonding are local effects while the global electronic structure is considered as a global effect.[101] To identify whether a particular dopant exhibited a local or global effect, the dopant ion was placed next to and far away from the oxygen vacancy and the vacancy formation energy was calculated. If the energy of forming an oxygen vacancy far away from the dopant is equal to the energy of forming a vacancy on nondoped oxide, then the dopant has a local effect. On the other hand, if the energy needed to form a vacancy next to the dopant is equal to that needed to form a vacancy far from it, then the dopant has a global effect. Dopants like La and Y reduce the energy needed for the formation of an oxygen vacancy next to them or far from them.[72] Such dopant ions affect vacancy formation energy due to the creation of a hole in the valence band maximum. When an oxygen vacancy is formed, one of the two electrons fills the hole and the other electron occupies a Ce 4f state. As the Ce 4f gap states are energetically higher than the hole states, La or Y doping lowers the vacancy formation energy. This is considered as a global effect as this mechanism is found to be independent of the distance between the vacancy formation site and the dopant. In case of non-reducible dopant like Zr, since $Zr^{4+}$ is

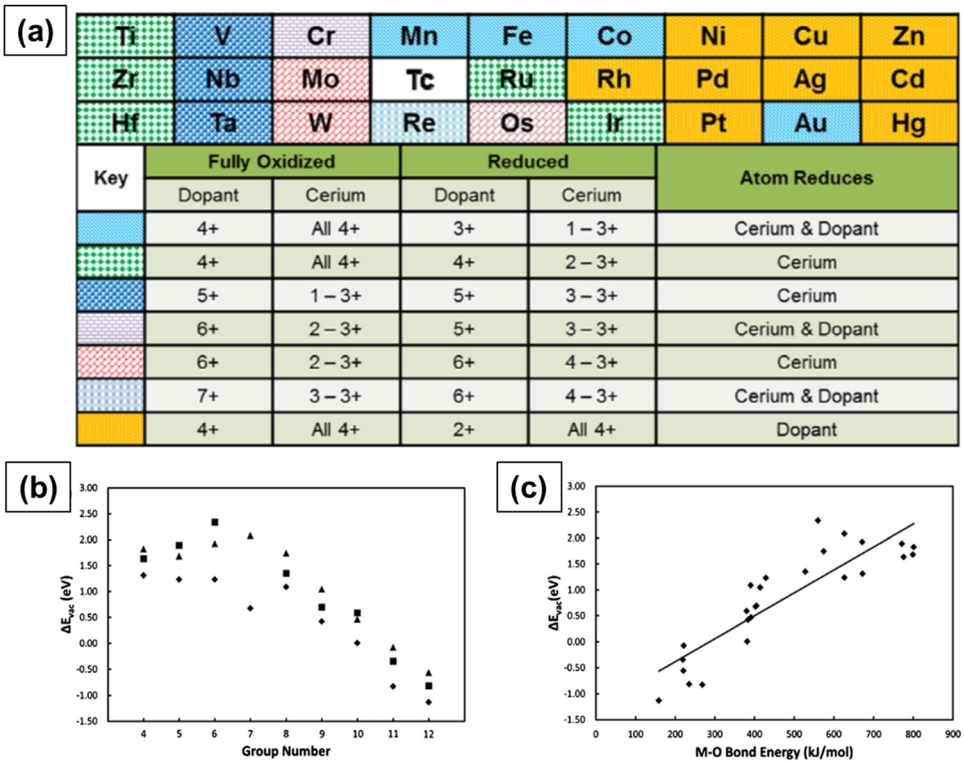


Fig. 9 (a) Trends in the electronic behavior of M-doped $CeO_2$ upon the formation of a surface oxygen vacancy in the nearest neighbor. Relationship between (b) oxygen vacancy formation energy and metal ion dopant column in the periodic table of elements and (c) oxygen vacancy formation energy and M–O bond dissociation energy. Reprinted from ref. 160.

smaller than $Ce^{4+}$, structure relaxation effects drive the lowering of the vacancy formation energy and hence the energies of the doped and defective surfaces are about the same. On the contrary, reducible dopants like Pt, Ru, Nb and Ta exhibit both local and global effects and hence the energy required to form a vacancy near the dopant is lower than that required to create a vacancy defect away from it. The local effect with these dopants is related to the chemical interaction, *i.e.*, dopant-oxygen binding.

The catalytic properties at the interface of ceria–metal have been extensively studied as this interface is the favored spot for the exchange of oxygen and is recognized as the active site responsible for the enhanced catalytic activity.[161,162] An interfacial reaction mechanism was proposed in which CO is suggested to be adsorbed on the metal and then oxidized by oxygen transfer from ceria, which in turn is oxidized by $H_2O$.[163,164] More detailed information has been obtained on the ceria–metal interaction, in which ceria is supported on the metal.[165] Additional proof of the interfacial activity involving the dissociation of CO-like molecules on oxygen vacancies on the ceria surface and a systematic investigation of ceria–metal properties has been demonstrated using advanced characterization techniques.[166–168] Some of the important fundamental observations of these studies explain the enhanced catalytic activities due to (a) the interplay between metal and oxygen vacancy, with the metal enabling the creation of oxygen vacancies on ceria; (b) the primary role of interface spots in the creation of reaction intermediates, therefore describing the different behaviors of metal–ceria systems and the ceria or metal alone; and (c) the presence of $Ce^{3+}$ species under transient reaction conditions in CO oxidation mechanism.

Theoretical studies using DFT calculations have unraveled a great deal of information on the structure of ceria-based catalysts, the mechanism and the role of oxygen vacancy defects and dopants in enhancing the catalytic activity. These results are in line with those of experimental studies and hence are helpful in gaining a fundamental understanding of the catalytic attributes of ceria-based materials in industrially relevant applications. While extensive research has been dedicated to this topic over the past twenty years, there remain several questions that still have to be explored. (i) Will different sized doped-ceria materials behave differently – does the size of the doped-ceria particle have an influence on catalytic activity; (ii) can any dopant enhance the catalytic activity – can dopants be grouped into different categories like dopants that have a very little effect and the ones that have significant effect on the catalytic activity; (iii) will doping with multiple metals enhance the catalytic activity greatly? If yes, what combination of metals can do this; (iv) will surface coating on doped ceria particles alter their catalytic properties (iiv); is surface modification by the addition of metal oxide clusters possible? If yes, what impact will it have on the catalytic activity?

### 2.5. Free radical scavenging

The distinctive free radical scavenging and regenerative antioxidant properties of the CeNPs have attracted considerable

 

interest in a broad range of applications in biomedicine.[169–171] In 2007, Seal's group first showed that CeNPs can efficiently scavenge superoxide radical anions and attributed this scavenging activity to the ability of Ce to switch between 3+ and 4+ oxidation states.[172] Subsequently, Pirmohamed and coworkers reported that the CeNPs show catalase mimetic activity.[173] Over the past decade, CeNPs have been investigated intensively as a potential therapeutic tool to inactivate free radicals and ameliorate causes of oxidative stress in a variety of *in vitro* and *in vivo* models, including cells, bacteria and whole animals. CeNPs can show antioxidant enzyme-mimetic activity, scavenge reactive oxygen species (ROS) and reactive nitrogen species (RNS) and protect against radiation.[174–178] They were also found to be effective in treating many diseases including cardiovascular diseases and neurodisorders.[170,179,180] Here, we review the reaction mechanisms and discuss the physicochemical properties of CeNPs that are responsible for their ROS/RNS scavenging activities and enable them to be used in pharmaceutical and biomedical applications.

**2.5.1. Antioxidant enzyme-like mimetic and ROS scavenging activity.** ROS ($O_2^{\bullet -}$, $H_2O_2$, $^{\bullet}OH$) and RNS ($ONOO^-$ and $^{\bullet}NO$) are powerful oxidizing and nitrating agents that play a critical role in several important biological processes including signal transduction, biochemical reactions and physiological and pathological changes.[181] While ROS/RNS are important in cell signaling, an excessive level of these species can damage the DNA, proteins and lipids and thereby cause oxidative stress, which subsequently results in the damage of tissues and cells. These conditions can lead to diseases like cancer, diabetes, cardiovascular and neurodegenerative diseases and arthritis.[182,183] While conventional antioxidants can only scavenge a particular type of ROS or RNS, CeNPs can scavenge many ROS and RNS, and their effectiveness is dependent of the size and surface properties of the NPs. The deleterious effects arising from surplus $O_2^{\bullet -}$ are usually controlled and alleviated by endogenous SOD enzymes located in the cytoplasm and mitochondria.[184] SOD enzymes eliminate $O_2^{\bullet -}$ species by converting them to $O_2$ and $H_2O_2$ through a catalytic dismutation reaction that occurs in two steps as follows.[185,186] This process is schematically shown in Fig. 10a.

$$O_2^{\bullet -} + 2H^+ + (Cu^+)\text{-SOD} \rightarrow H_2O_2 + (Cu^{2+})\text{-SOD} \quad (2.6)$$

$$O_2^{\bullet -} + (Cu^{2+})\text{-SOD} \rightarrow O_2 + (Cu^+)\text{-SOD} \quad (2.7)$$

$$2O_2^{\bullet -} + 2H^+ \rightarrow H_2O_2 + O_2 \text{ (overall)} \quad (2.8)$$

The SOD enzyme works by accepting electrons from or losing electrons to $O_2^{\bullet -}$. In reaction 2.6, the reduced $(Cu^+)$-SOD catalyzes the oxidation of $O_2^{\bullet -}$ to $H_2O_2$ while in reaction 2.7, the oxidized $(Cu^{2+})$-SOD catalyzes the reduction of $O_2^{\bullet -}$ to $O_2$. Reduced $(Cu^+)$-SOD is regenerated after reaction 2.7 and the cycle begins again. Overall, for every molecule of $H_2O_2$ formed, $2O_2^{\bullet -}$ molecules are dismutated. A similar mechanism for

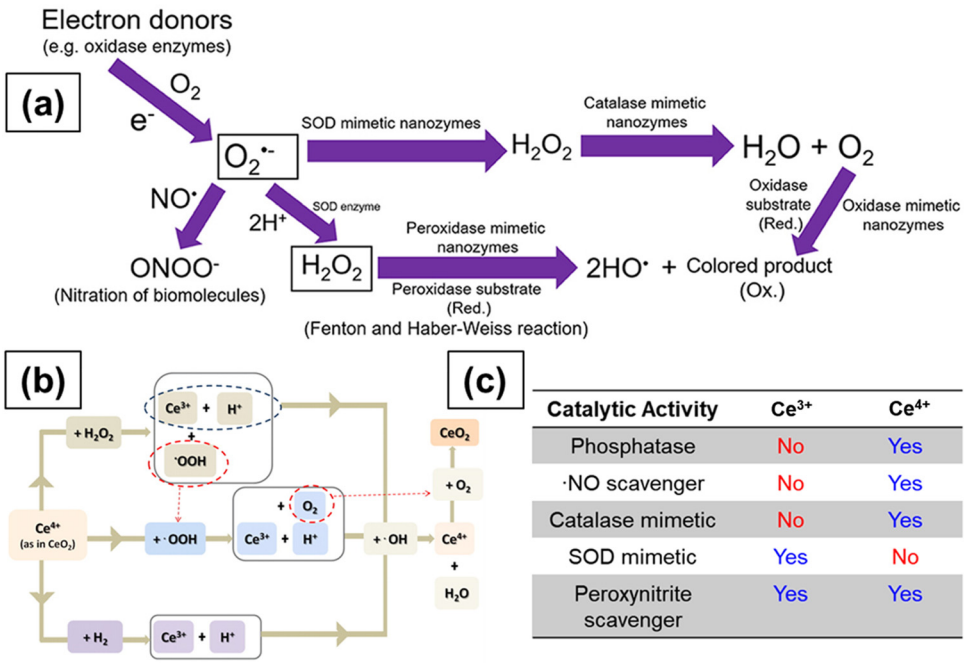


| Catalytic Activity | $Ce^{3+}$ | $Ce^{4+}$ |
|---|---|---|
| Phosphatase | No | Yes |
| ·NO scavenger | No | Yes |
| Catalase mimetic | No | Yes |
| SOD mimetic | Yes | No |
| Peroxynitrite scavenger | Yes | Yes |

Fig. 10 (a) Schematic representation showing the reactions involved in antioxidant enzyme-mimetic and ROS and RNS scavenging properties of ceria particles. Superoxide ($O_2^{\bullet -}$) anions are first produced by single electron donors and the $O_2^{\bullet -}$ anions react with $^{\bullet}NO$ and $H^+$ to form $OONO^-$ and $H_2O_2$, respectively. The $O_2^{\bullet -}$ anions are converted to $H_2O_2$ by SOD and SOD mimetic enzymes. Catalase mimetic enzymes can further convert $H_2O_2$ into water and oxygen. Hydroxyl radicals can be generated from $H_2O_2$ in the presence of peroxidase mimetic enzymes, and oxidase mimetic enzymes can oxidize the substrate and form a colored product without the presence of $H_2O_2$. Reprinted from ref. 199. (b) Transformation of $Ce^{3+}$ to $Ce^{4+}$ and regeneration of $Ce^{3+}$ from $Ce^{4+}$. Reprinted from ref. 193. (c) Effect of SOD and catalase mimetic properties and $^{\bullet}NO$ and $OONO^-$ scavenging properties of ceria particles on the relative surface $Ce^{3+}$ concentration of ceria. Reprinted with permission from ref. 200. Copyright 2013 American Chemical Society.

superoxide radical anion scavenging by ceria NPs has been proposed involving the oxidoreduction of $Ce^{3+}/Ce^{4+}$ states at the NP surface, as shown below.[170,180]

$$O_2^{\bullet -} + Ce^{3+} + 2H^+ \rightarrow H_2O_2 + Ce^{4+} \text{ (oxidation of } Ce^{3+} \text{ to } Ce^{4+}) \quad (2.9)$$

$$O_2^{\bullet -} + Ce^{4+} \rightarrow O_2 + Ce^{3+} \text{ (reduction of } Ce^{4+} \text{ to } Ce^{3+}) \quad (2.10)$$

The above two reactions indicate that the $Ce^{3+}/Ce^{4+}$ redox couple of ceria NPs can be regenerated. In the first step, superoxide anions bind to oxygen vacancies around two $Ce^{3+}$ species and an electron is transferred from $Ce^{3+}$ ion to an oxygen atom. In the second step, two protons in the solution bind to two oxygen atoms and form a molecule of $H_2O_2$. The second superoxide anion then binds to the remaining oxygen vacancy and a second $H_2O_2$ molecule is formed and $Ce^{3+}$ is oxidized to $Ce^{4+}$. Furthermore, the two electrons produced will reduce the $Ce^{4+}$ ions to $Ce^{3+}$ ions and, in this case, $H_2O_2$ acts as a reducing agent. However, while these reactions have been postulated, the mechanisms driving the SOD-mimetic activity of ceria NPs are still subject to debate and their behavior in biological environments are subject of numerous scientific investigations. In some studies, CeNPs having higher $Ce^{3+}$ concentration were more efficient scavengers of $O_2^{\bullet -}$ than those with lower $Ce^{3+}$ concentration.[172] In another study, CeNPs treated with $H_2O_2$ and hence having lower $Ce^{3+}$ concentration showed a decrease in the SOD mimetic activity as compared to bare ceria, implying that the surface $Ce^{3+}$ species play a key role in the SOD mimetic activity,[187] as indicated in Fig. 10c. These processes take place at the surface of the metal oxide and are affected by conditions such as pH and temperature.[169]

High $H_2O_2$ levels are considered detrimental to cellular homeostasis as compared to high levels of $O_2^{\bullet -}$ as $H_2O_2$ forms highly toxic $^{\bullet}OH$ radicals *via* the Fenton reaction with metals, as shown in Fig. 10a. Enzymes like glutathione peroxidase, catalase and peroxiredoxins all lower the $H_2O_2$ levels in cells, but catalase is the most efficient enzyme in disproportionating $H_2O_2$ into innocuous $H_2O$ and $O_2$,[188] as shown in Fig. 10a. The catalase mimetic activity of CeNPs was first demonstrated based on the shift in the peak in the luminescence spectra of ceria NPs after the addition of $H_2O_2$ to astrocyte cells.[174] The luminescence spectra of the CeNPs reversed to its original form (the peak shifted back to the original wavelength) after the decomposition of $H_2O_2$. The CeNPs protect cells from oxidative stress due to their catalase mimetic and SOD mimetic activities. The catalase mimetic activity depends strongly on the concentration of $Ce^{3+}$ with ceria having low $Ce^{3+}$ concentration, showing improved catalase activity as compared to those with high concentration of $Ce^{3+}$,[173] as indicated in Fig. 10c.

Besides, $Ce^{3+}$ concentration, factors like particle size, buffer species like $PO_4^{3-}$, and solution pH can all affect the catalase and SOD-mimetic activities of ceria.[189,190] The presence of $PO_4^{3-}$ was shown to diminish the SOD-mimetic activity and enhance the catalase activity due to the ability of $Ce^{3+}$ ions to form strong coordination complexes on reaction with $PO_4^{3-}$, which bind preferentially to ceria NPs with high $Ce^{3+}$ concentration. The mechanism by which phosphate changed the properties of ceria NPs was attributed to the formation of $CePO_4$-like complexes that blocks the redox activity of ceria NPs.[189] Since the ability of ceria particles to cycle between 3+ and 4+ oxidation states is the key to their catalytic activity, the catalase mimetic activity diminishes in the presence of any compound that can block $Ce^{3+}$ and stabilize the ceria NPs in the 3+ state. Therefore, the ability of CeNPs to swiftly change between 3+ and 4+ oxidation states is crucial in maintaining their SOD-mimetic activity. These studies indicate the need to comprehensively study and understand the influence of phosphate ions and other ions on SOD mimetic activity of ceria, particularly because cells contain high concentrations of phosphate ions, and other ions and their presence can potentially affect the biological activities of ceria NPs.

Contradictory results were reported in the literature on the influence of pH on the antioxidant activity of CeNPs with some studies showing no effect of pH and other studies, revealing marked effects on both the SOD mimetic activity and $Ce^{3+}$ concentration on the particle surface. Singh *et al.*[189] and Xue *et al.*[176] showed that the dispersion stability and SOD mimetic activity of ceria NPs are not affected by pH. In contrast, using XPS spectroscopy, Karakoti *et al.* showed that the $Ce^{3+}$ concentration changed with pH.[191] Perez *et al.* investigated the effect of pH on the antioxidant properties of CeNPs.[190] Dextran coated-ceria NPs exhibited catalase mimetic activity in alkaline conditions but not in acidic conditions (pH 4). They argued that the antioxidant ability of ceria NPs is dependent on their ability to cycle between 3+ and 4+ oxidation states and that the $Ce^{3+}$ ions are converted to $Ce^{4+}$ ions during the $H_2O_2$ scavenging process. The regeneration of $Ce^{3+}$ occurs through chemical reactions between $Ce^{4+}$ ions on the surface of NPs and $H^+$ ions in solution, as shown in Fig. 10b. The low pH of the solution inhibited the ability of ceria NPs to scavenge more free radicals and therefore diminished the antioxidant activity due to the high concentration of $H^+$ ions. These conflicting results could be due to different synthesis methods and hence varying surface $Ce^{3+}$ concentrations. Moreover, the effect of surface coating or surface reactions, the potential binding of peroxide and superoxide species to the ceria surface, and the stabilizing effects of coexisting ions have not been taken into account in these studies and can have significant effects in biological environments. Systematic studies of the effect of surface ligands, surface faceting and a potential reorganization of ceria NPs are the essential next steps needed to understand these processes, the interfacial reactions and their contribution to the ceria's unique reactivity.

CeNPs can also efficiently scavenge $^{\bullet}OH$ (hydroxyl radical), a strong oxidant. Hydroxyl radicals in cells are usually scavenged by two methods. The first method involves preventing the initiation of $^{\bullet}OH$ by enzymes like SOD, catalase and glutathione peroxidase. The second method involves the breaking of the chain reaction of $^{\bullet}OH$ by nonenzymatic antioxidants.[192] The $^{\bullet}OH$ scavenging ability of CeNPs was first shown by Das *et al.*,

 

who first demonstrated that CeNPs were able to scavenge $^{\bullet}OH$ formed from $H_2O_2$.[175] When CeNPs were treated with $H_2O_2$, the color changed from yellow to orange, indicating that $Ce^{3+}$ (yellow) reacts with the $^{\bullet}OH$ generated from $H_2O_2$ and gets oxidized to $Ce^{4+}$ (orange), as shown in Fig. 10a. In a later report, Xue *et al.* demonstrated that CeNPs scavenge $^{\bullet}OH$ by providing direct experimental evidence *via* a methyl violet assay.[176] With the decrease in the size of CeNPs and a corresponding increase in the concentration of surface $Ce^{3+}$, the efficiency of CeNPs in scavenging $^{\bullet}OH$ and preventing a reduction in the optical absorption of methyl violet increased. The $^{\bullet}OH$ scavenging activity of CeNPs was attributed to a two-step mechanism involving the ability of $^{\bullet}OH$ to reversibly cycle between $Ce^{3+}$ and $Ce^{4+}$. In the first step, $^{\bullet}OH$ oxidizes $Ce^{3+}$ to $Ce^{4+}$, and in the second step, $Ce^{4+}$ is reduced back to $Ce^{3+}$. The mechanism can be described by the chemical reactions 2.9 and 2.10 and is also schematically represented[193] in Fig. 10b. The morphology of CeNPs was also found to have a significant impact on their scavenging activity to the different crystal planes exposed by different morphologies. The antioxidant activity of different morphologies follows the order: nanowires > nanobars > NPs.[194] A better understanding of the catalytic mechanisms and the fundamental parameters affecting the 'enzyme-like' activity will enable the future development of high performance nanoenzymes[195,196] as alternatives to natural oxidase and peroxidase enzymes, providing advantages such as a stability, robustness and low cost, making them suitable for many applications.

**2.5.2. RNS scavenging activity.** Nitric oxide (NO) is not a highly reactive molecule but nitric oxide radical ($^{\bullet}NO$) reacts with $O_2^{\bullet-}$ or $O_2$ and forms the highly reactive and damaging peroxynitrite anion ($OONO^-$) (Fig. 10a) that can damage lipids, DNA and proteins.[197] Self and co-workers showed that CeNPs scavenge $^{\bullet}NO$ under physiologically relevant conditions[198] and showed that $^{\bullet}NO$ scavenging was more predominant in particles with a lower concentration of $Ce^{3+}$ and oxygen vacancies in contrast to the SOD-mimetic activity, which is predominant in particles with a higher concentration of $Ce^{3+}$ and oxygen vacancies. They postulated that the CeNPs scavenge $^{\bullet}NO$ with the help of electropositive nitrosyl ligand formed by internal electron transfer from $^{\bullet}NO$ to a $Ce^{4+}$ ion according to the following reaction.

$$Ce^{4+} + {}^{\bullet}NO \rightarrow (Ce^{4+}NO \leftrightarrow Ce^{3+}NO^{+}) \quad (2.11)$$

Fig. 10c summarizes the SOD and catalase mimetic properties and $^{\bullet}NO$ and $OONO^-$ scavenging properties of CeNPs and the effect of the relative surface $Ce^{3+}$ concentration on varying radicals.

**2.5.3. Peroxidase and phosphatase-like mimetic activities.** CeNPs exhibit peroxidase, oxidase and phosphatase mimetic activities. Heckert *et al.* explored the ability of CeNPs to catalyze a Fenton-like reaction in the presence of $H_2O_2$ and showed that $CeCl_3$ generated hydroxyl radicals in the presence of $H_2O_2$.[187] EPR analysis indicated the generation of both $^{\bullet}OH$ and $O_2^{\bullet-}$ in the presence of cerium and $H_2O_2$. The authors hypothesized that $^{\bullet}OH$ and $O_2^{\bullet-}$ were generated from reactions similar to Fenton/Haber Weiss reactions.

$$Ce^{3+} + H_2O_2 + H^+ \rightarrow Ce^{4+} + {}^{\bullet}OH + H_2O \quad (2.12)$$

$$^{\bullet}OH + H_2O_2 \rightarrow HO_2^- + H_2O \quad (2.13)$$

$$Ce^{4+} + HO_2^- \rightarrow O_2 + Ce^{3+} + H^+ \quad (2.14)$$

CeNPs can exhibit peroxidase-like catalytic activity over a wide range of temperatures and pH values, making them more stable substitutes to natural enzymes.[201]

A phosphatase is an enzyme that hydrolyzes phosphoric acid monoesters into phosphate ions.[202] Phosphatase enzymes play a significant role in many biological processes, including signal transduction and cellular regulation. Some metal ions and their complexes were shown to enhance the rate of phosphate ester hydrolysis through different processes like nucleophile activation, Lewis acid activation and leaving group activation.[203] Lanthanide ions and their complexes are efficient catalysts for hydrolyzing phosphate esters.[204] CeNPs have been shown to effectively mediate the dephosphorylation of phosphopeptides[205] in less than ten minutes. The dephosphorylation activity of CeNPs was attributed to the Lewis acidity of $Ce^{3+}/Ce^{4+}$ surface sites capable of coordinating oxygen atoms of phosphate groups and lowering the P–O bond scission energy by promoting nucleophilic attack from hydroxyl groups on the surface. Ceria NPs can also be used for the dephosphorylation of biologically active amino acids.[206] Kuchma and collaborators investigated the reactivity of CeNPs towards phosphate ester bonds of biologically relevant molecules like ATP, *p*-nitrophenylphosphate (*p*NPP), DNA and *o*-phospho-L-tyrosine.[207] The dephosphorylation mechanism was investigated using DFT calculations, and the reaction was found to proceed through phosphate group inversion similar to an $SN^2$ mechanism. Because of the ability of CeNPs to interact with the phosphate ester bonds of biologically relevant molecules, they can be used as potential therapeutics.

The ability of CeNPs to eliminate surplus levels of $O_2^{\bullet-}$ and $H_2O_2$ from cells makes them ideal SOD and catalase-mimetic. Nevertheless, the exact mechanisms by which CeNPs act as antioxidant enzyme-mimetic in the cells have been a topic of debate. The variability in the types of CeNPs used in the *in vitro* and *in vivo* studies can strongly influence the surface $Ce^{3+}$ concentration and hence their surface reactivity. Limitations of existing characterization tools and lack of sophisticated techniques to analyze such interactions *in situ* hinder the fundamental understanding of the enzyme-mimetic activity of the CeNPs. The apparent differences in results can also arise from the different synthetic procedures of the particles. Moreover, the limited data on the detailed characterization of CeNPs exposed to biological environments that would take into account the effect of the medium composition, surface binding and non-specific adsorption on the particle reactivity makes it difficult to draw fundamental conclusions based on a direct comparison with the reported mimetic activity in simple aqueous solutions. Ideally, standards for the synthesis techniques

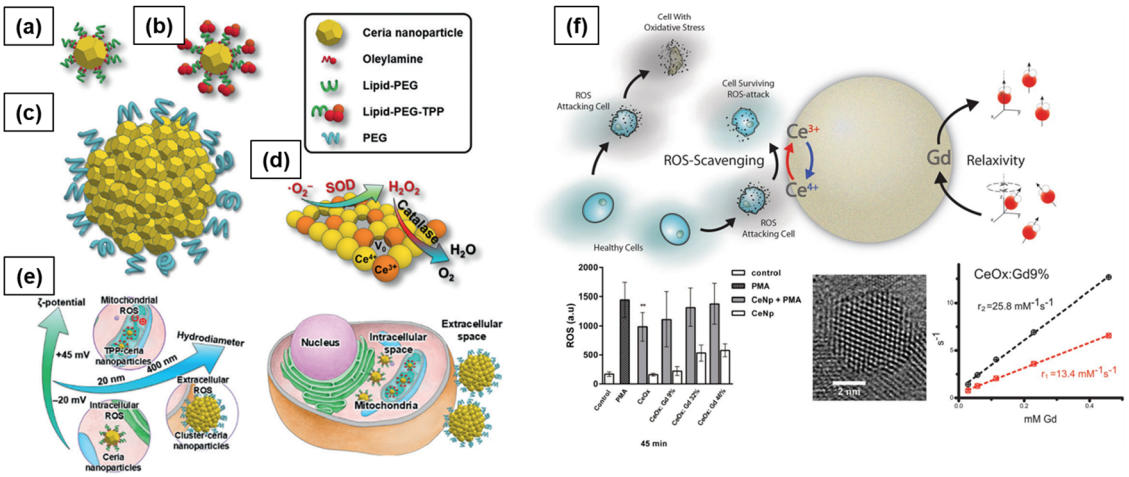


Fig. 11 Schematic showing (a) ceria particle, (b) triphenylphosphonium (TPP) coated ceria particle, (c) ceria particle cluster, (d) SOD- and catalase-mimetic activities of ceria particles and associated ROS scavenging reactions, (e) ROS scavenging activities of ceria, TPP-coated ceria and ceria particle cluster in cells and (f) top: Gd-doped ceria particles with antioxidant and MRI contrast enhancing properties; bottom: antioxidant assay, HRTEM image and relaxivity measurement results (from left to right). Reprinted from ref. 208 and 209.

of CeNPs with a full characterization of their physicochemical properties should be established to prevent the misinterpretation of results. Advances in different microscopy spectroscopic methods have been very helpful in the analytical characterization of these materials under biological conditions. Establishing a set of characterization tools that enable comprehensive correlation between the physicochemical properties of CeNPs and their antioxidant/prooxidant activity is necessary and, in principle, can be helpful in tuning the properties of the particles. A schematic of the SOD and catalase mimetic activities of pure ceria, triphenylphosphonium (TPP) coated ceria[208] and Gd-doped ceria[209] is shown in Fig. 11, indicating the effect of surface ligands on CeNPs activity.

### 2.6. Interactions with molecular oxygen and $H_2O_2$

The characterization of different types of oxygen species formed by the adsorption of $O_2$ on CeNPs is important as these species play a key role in many oxidation reactions. One of the major applications of CeNPs is as an oxygen storage material in TWC converter in automotive exhausts. Ceria acts as a buffer to supply $O_2$ during $O_2$-deficient conditions of engine operation and extract $O_2$ when there is surplus $O_2$ in the exhaust stream, thus helping to maintain the concentration of oxygen. The mechanism of oxidation reactions on ceria surfaces involves the reaction of the adsorbate with the $O_2$ present in the substrate, which is then replenished from the gas phase $O_2$.[125] Studies to understand the adsorption and desorption of $O_2$ on ceria surfaces are thus critical for TWC applications. Using both experimental methods and theoretical models, it has been established that the reactivity of stoichiometric ceria (unreduced ceria) towards molecular oxygen is very low as compared to that of reduced ceria. $O_2$ physisorbs on the surface of unreduced ceria NPs by a weak interaction dominated by dispersion forces.[210–212] DFT calculations of oxygen adsorption revealed very low adsorption energies and showed that $O_2$ adsorbs only at very low temperatures on unreduced ceria. On the other hand, molecular oxygen binds very strongly on reduced ceria surfaces.[213–215]

The formation mechanism involves the creation of an oxygen vacancy, which results in the formation of two $Ce^{3+}$ ions; hence, the vacancy site is a two-electron donor center. $O_2$ interacts with the oxygen vacancy and adsorbs such that one oxygen atom fills the vacancy and the other points out from the surface.[210] $O_2$ adsorption at an oxygen vacancy site therefore removes the defect and results in the formation of a surface peroxo species ($O_2^{2-}$).[216] Diamagnetic $O_2^{2-}$ can be detected by Raman and FTIR spectroscopy. The peaks related to $O_2^{2-}$ typically occur in the 820–880 $cm^{-1}$ region.[217] $O_2^-$ species, on the other hand, are formed when $O_2$ interacts with low-coordinated $Ce^{3+}$ ions (steps, edges, dislocations, *etc.*), which are one-electron donors.[218] In this case, oxygen vacancies are not involved and $O_2^-$ species are formed in the vicinity of exposed $Ce^{3+}$ ions.[213] The fingerprint of the $O_2^-$ species is, besides the characteristic EPR signal, a Raman or IR peak in the region 1110–1150 $cm^{-1}$.[216]

Early experimental studies used FTIR spectroscopy to investigate the adsorption of $O_2$ on ceria. The adsorption of $O_2$ on partially reduced ceria resulted in an IR peak at 1128 $cm^{-1}$ attributed to $O_2^-$ species and at 883 $cm^{-1}$ related to peroxide species. $O_2^-$ and $O_2^{2-}$ are the intermediates formed during oxygen dissociation/re-oxidation that occurs according to the following scheme.[219]

$$O_{2(aq/g)} \leftrightarrow O_{2(ads)} \leftrightarrow {O_{2(ads)}}^{-} \leftrightarrow {O_{2(ads)}}^{2-} \leftrightarrow 2{O_{(ads)}}^{-} \leftrightarrow 2{O_{(lattice)}}^{2-} \quad (2.15)$$

where aq stands for aqueous and ads stands for adsorbed.

As can be seen from Eq. 2.15, first, the $O_2^-$ is formed after exposure to $O_2$. The $O_2^-$ is then converted into peroxide and finally to lattice oxygen by gaining more electrons from the surface. As a result of this re-oxidation, the surface will become

 

electron-deficient and further electron transfer from the surface to $O_2$ does not occur. Similar bands were also observed in studies that used Raman spectroscopy to probe the adsorption of $O_2$ on ceria. Pushkarev *et al.* studied the adsorption of $O_2$ on CeNPs using *in situ* Raman spectroscopy and demonstrated that $O_2$ adsorbs on one- and two-electron defects and forms $O_2^-$ and $O_2^{2-}$ species, respectively.[215] Two bands each in ranges of 1120–1140 $cm^{-1}$ and 830–880 $cm^{-1}$, related to superoxide and peroxide species, respectively, were observed. The two different bands can be ascribed to disparate configurations of the binding of superoxide species to ceria and to the peroxide species bound to defects with different geometries. Temperature-programmed experiments revealed the re-oxidation of the surface by adsorbed oxygen species. The $O_2^-$ that form first due to the adsorption of $O_2$ are unstable and transform into peroxides, which then translate into lattice oxygen, similar to what was reported previously.

Wu *et al.* investigated the adsorption of $O_2$ on ceria nanocubes, nanorods and nanooctahedra exposing (100), (110)/(100) and (111)/(100) crystal planes, respectively.[220] They illustrated the mechanism of oxygen activation and transformation on these surfaces, which is pivotal in understanding the mechanism of oxidation reactions catalyzed by nanoscale ceria. The adsorption of $O_2$ on ceria gave rise to a band at 1139 $cm^{-1}$, which they attributed to the O–O stretching of $O_2^-$. The other observed peaks at 830 and 860 $cm^{-1}$ were ascribed to peroxide species on isolated and clustered two-electron defects. The amount of adsorbed oxygen species on reduced ceria nanoshapes changes with the degree of reduction. The weak bands of adsorbed oxygen species in ceria nanorods suggest the presence of small amounts of defect sites. Temperature-dependent oxygen adsorption experiments revealed that the adsorbed $O_2^-$ species were stable up to 350 K while the peroxide species were stable until 473 K. Based on their results, they suggested that the re-oxidation of ceria occurs, as shown in Eq. 2.15. 20% of adsorbed oxygen desorbs into gas phase through disproportionation reactions of $O_2^{2-}$ and $O_2^-$ species, as shown below.

$$O_{2\ ads}^- + O_{2\ ads}^- \rightarrow O_{2\ ads}^{2-} + O_2 \quad (2.16)$$

$$O_{2\ ads}^{2-} + O_{2\ ads}^{2-} \rightarrow 2O_{lattice}^{2-} + O_2 \quad (2.17)$$

The adsorption of oxygen on the (111) surface of ceria was studied using DFT calculations. $O_2$ does not adsorb on oxidized surfaces and binds weakly to one-electron defect sites.[210] $O_2^-$ forms on the hollow sites of the (111) surface in a side-on configuration above $Ce^{4+}$ ions. The $O_2^-$ preferentially adsorbs on $Ce^{4+}$ surface sites due to electrostatic interaction; hence, $Ce^{4+}O_2^-$ is predicted to be the reactive intermediate as $Ce^{3+}O_2$ is more stable. Partially-reduced ceria exposed to $O_2$ resulted in the formation of $O_2^-$ and $O_2^{2-}$, and the associated Raman peaks were observed at 1131 and 825 $cm^{-1}$, respectively.[217] The energies of $O_2$ adsorption on unreduced ceria surfaces were found to be endothermic while those on reduced surfaces were exothermic. The position of oxygen vacancies can affect the formation and dissociation of oxygen species.

Most of the experimental and theoretical results indicate that oxygen vacancy sites and $Ce^{3+}$ play crucial roles in the formation of peroxide and superoxide species, respectively, and that these adsorbed oxygen species are active intermediates in the subsequent oxidation reactions.[221,222] The possible geometries of adsorbed oxygen species at different active sites on the reduced and unreduced surfaces of ceria are depicted in Fig. 12.

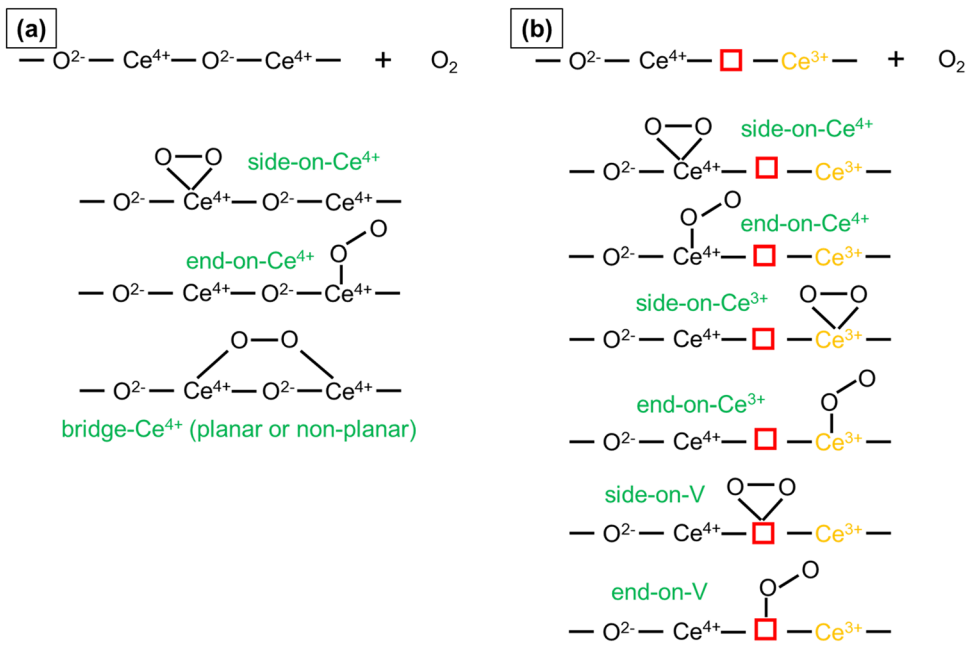


Fig. 12 Possible complexes of adsorbed oxygen species formed due to the interaction of molecular $O_2$ with ceria NPs.

The adsorption energies, vibrational frequencies, partial charges and relevant geometrical parameters for different configurations have been calculated by several theoretical studies.[210,213] The end-on-V configuration of peroxide adsorption on ceria is energetically the most favorable one of all the possible structures. The side-on-V structure of superoxide adsorption is the second stable structure. $O_2$ physisorbs (adsorbs very weakly) on $Ce^{4+}$ of an unreduced surface in an end-on configuration. The values of energies suggest that $O_2$ binds very strongly above one-($Ce^{3+}$) and two-electron defects (oxygen vacancies), implying that the dissociation process is energetically more favorable on the reduced ceria surface than on an oxidized surface.[223]

In summary, $O_2$ adsorbs very strongly on the surface oxygen vacancy and forms diamagnetic peroxide species since two electrons from 4f orbitals of $Ce^{3+}$ ions are transferred to the half-filled $\pi_{2p}$* orbitals of $O_2$.[223] $O_2^{2-}$ species are formed from the adsorption of $O_2$ at low-coordinated $Ce^{3+}$ ion, which is quite far away from the oxygen vacancy site.[213] $O_2$ preferentially binds in a side-on configuration, with the end-on mode being less favorable. This interaction results in the charge transfer of one of the two electrons in the 4f orbital of $Ce^{3+}$ to the $\pi_g$* orbital of $O_2$. Simultaneously, one $Ce^{3+}$ ion is oxidized to $Ce^{4+}$ ion and a complex ($Ce^{4+}O_2^-$) is formed through ionic interaction.[217]

The interaction of $H_2O_2$ with CeNPs was also studied in great detail in many reports on antioxidant activity relevant to biomedical applications. Nonetheless, the mechanism of reaction of $H_2O_2$ with CeNPs is still not completely understood. Postulating that $H_2O_2$ oxidizes $Ce^{3+}$ to $Ce^{4+}$, it was shown that CeNPs exposed to $H_2O_2$ and having a lower concentration of $Ce^{3+}$ suppressed the SOD mimetic activity.[187] Later, several studies demonstrated that the oxidation of $Ce^{3+}$ to $Ce^{4+}$ is reversible and that the reduction happens after a long period (15 days) in aqueous solution following the degradation of $H_2O_2$.[180,190] The mechanism of the reduction reaction was investigated, and it was proposed that $H_2O_2$ reacts with $Ce^{4+}$ ions and reduces them to $Ce^{3+}$ ions while it simultaneously gets oxidized to molecular $O_2$. Some controversies exist regarding the mechanism of oxidation/surface complexation of CeNPs, and the impact of surface coating on the oxidation/complexation in the presence of $H_2O_2$. Most of the studies ascribed the change in the color of CeNPs in the presence of $H_2O_2$ to the conversion of $Ce^{3+}$ to $Ce^{4+}$ while some suggested that the color change was due to the formation of $Ce^{3+}O_2^{2-}$ and/or $Ce^{4+}O_2^-$ or $Ce^{4+}$.[224] With respect to surface coating, some studies showed that coating does not have any influence on the reaction of $H_2O_2$ with the particles while others showed apparent differences in the reactivity depending on the surface coating.[225,226] In a comparative study, the 8.2 nm ceria NPs coated with a thick layer of polyethylene imine or polymaleicanhydride-*alt*-1-octadecene were found to be less reactive than the smaller 3.8 nm with a thin layer of poly(lactic acid).[225]

Yu *et al.* developed an E-pH diagram for the $CeO_2$–$H_2O$–$H_2O_2$ system to understand the role of $H_2O_2$ in the preparation of cerium conversion coating processes.[227] Their results indicated that $H_2O_2$ could perform dual functions, either oxidize $Ce^{3+}$ to $Ce^{4+}$ or reduce $Ce^{4+}$ to $Ce^{3+}$. It was shown that $H_2O_2$ acts as a reducing agent at lower pH values (pH $<$ 2) and as an oxidizing agent at higher pH values. $Ce^{4+}$ can exist in several hydrolyzed forms depending on pH and the most stable ones are $Ce(OH)^{3+}$, $Ce(OH)_4$, $Ce(OH)_2^{2+}$ and polymerized form. The overall reaction for reducing the action of $H_2O_2$ on $Ce^{4+}$, $Ce(OH)^{3+}$ and $Ce(OH)_2^{2+}$ in the pH regions $<-0.7$, $-0.7$ to 0.7 and 0.7–2.1, respectively, can be written by the following equations.

$$2Ce^{4+} + H_2O_2 \rightarrow 2Ce^{3+} + O_2 + 2H^+ \quad (2.18)$$

$$2Ce(OH)^{3+} + H_2O_2 \rightarrow 2Ce^{3+} + O_2 + 2H_2O \quad (2.19)$$

$$2Ce(OH)_2^{2+} + H_2O_2 + 2H^+ \rightarrow 2Ce^{3+} + O_2 + 4H_2O \quad (2.20)$$

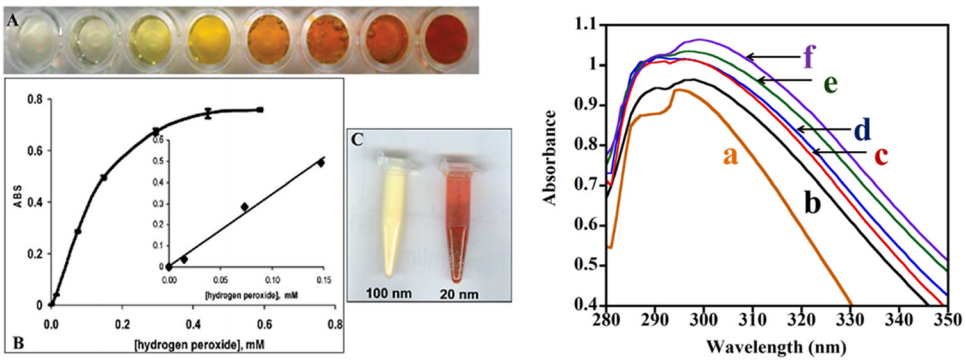


Fig. 13 Left. Colorimetric analysis of colloidal ceria nanoparticle dispersion treated with $H_2O_2$ as a function of $H_2O_2$ concentration at neutral pH, indicating color change proportional with the concentration of $H_2O_2$: (A) photos of ceria dispersions showing color with increasing intensity as a function of $H_2O_2$ concentration. (B) Calibration curve obtained by plotting optical absorption as a function of $H_2O_2$ concentration. Inset shows the linear region. (C) Effect of $H_2O_2$ addition to ceria dispersion on particle size (20 and 100 nm ceria). Reprinted with permission from ref. 229. Copyright 2011 American Chemical Society. Right. UV spectra illustrating the $CeO_2$ NPs peaks of $Ce^{3+}$ (289 nm) and $Ce^{4+}$ (297 nm) for unreduced $CeO_2$ NPs (no $H_2O_2$) (a) and $CeO_2$ NPs reduced for 30 min with different $H_2O_2$ concentrations of 5 mM (b), 10 mM (c), 20 mM (d), 50 mM (e) and 100 mM (f). Reprinted with permission from ref. 230. Copyright 2013 American Chemical Society.

 

$Ce^{3+}$ can be oxidized to $Ce^{4+}$ in the presence of $H_2O_2$ with increasing pH, and the oxidation reaction can be represented by the general equation shown below

$$2Ce^{3+} + H_2O_2 + xH_2O \rightarrow 2Ce(OH)_{1+x/2}^{(3-x/2)+} + xH^+ \quad (2.21)$$

where the value of $x$ could be 0, 2 or 6.

$Ce^{3+}$ is the more stable form in the lower pH range and $Ce^{4+}$ can be reduced to $Ce^{3+}$ by $H_2O_2$. Conversely, $Ce^{4+}$ is the more stable form at higher pH values. $Ce^{3+}$ is soluble over a wide pH range (pH < 11) as compared to $Ce^{4+}$, which is soluble at pH < 4. During the oxidation of $Ce^{3+}$ to $Ce^{4+}$ with $H_2O_2$, the concentration of the intermediate $Ce^{3+}/Ce^{4+}$ complexes is very high.

Scholes and co-workers performed the titration of cerium-based conversion coating solutions to investigate the role of $H_2O_2$.[228] The titration results indicated the formation of a Ce(III) peroxo complex like $Ce(H_2O_2)^{3+}$, and successive deprotonation led to the formation of $Ce^{3+}O_2^{2-}$, which on oxidation gave Ce(IV) peroxo species like $Ce(IV)(O_2)(OH)_2$. Finally, the Ce(IV)peroxo complex converted to $CeO_2$ after several months and the authors attributed the conversion to the decomposition of the complex. The use of ceria NPs as colorimetric probes for the detection of glucose has been explored by several studies. The addition of $H_2O_2$ to a dilute dispersion of 20 nm ceria NPs (colorless) changed the color of the particles to reddish-orange,[229] as shown in Fig. 13. The color change indicates the modification in surface properties and chemical composition of the ceria NPs. FTIR analysis confirmed the presence of peroxo species in the presence of $H_2O_2$, and XPS analysis indicated a slight change in the concentration of $Ce^{4+}$. Ultraviolet-visible (UV-Vis) absorption analysis shows a red-shift in the spectra of CeNPs in the presence of $H_2O_2$ with the extent of red shift increasing with the concentration of $H_2O_2$.[230,231] The coordination number of Ce ions after $H_2O_2$ addition was found to increase based on analysis of the X-ray absorption fine structure (XAFS) measurements. However, the coordination number decreased back nearly to the original value at the end of the reaction (after 9 hours); the increase in the coordination number was attributed to the formation of surface-adsorbed peroxide complexes.

The interaction of $H_2O_2$ with oleate-capped CeNPs in dichloromethane (DCM) was investigated.[232] Fig. 14 shows the UV-Vis spectra of CeNPs treated with $H_2O_2$ as a function of time in the wavelength range from 200 to 700 nm. $H_2O_2$ addition was found to increase the absorbance at 2 wavelengths ($\lambda_1$ = 285 nm) and ($\lambda_2$ = 380 nm). The deconvolution of the UV-Vis spectra of the $H_2O_2$ adsorption by CeNPs revealed the appearance of two peaks corresponding to two processes: the peak at 285 nm was related to the oxidation of $Ce^{3+}$ to $Ce^{4+}$ while the peak at 380 nm was due to the formation of surface-adsorbed peroxide species. Further, the FTIR peak at 840 $cm^{-1}$ indicated the presence of peroxide/hydroperoxide species.

It should be noted that in an aqueous medium, ceria can exist in different hydrolyzed forms like $Ce(OH)_2^{2+}$, $Ce(OH)_3$, and $Ce(OH)_4$, and after the addition of $H_2O_2$, it can form cerium(III) peroxide ($Ce^{3+}O_2^{2-}$), cerium(IV) peroxide ($Ce^{4+}O_2^{2-}$) and cerium hydroperoxide ($Ce(OH)_2(O_2)$). Certainly, the ratio of these different species is dependent on the size, surface coating, preparation method, pH and ionic strength. These complexes are reversible and the particles can recover their activity after several days/weeks at room temperature or within few minutes at high temperatures of 70–100 °C due to the decomposition of the surface-adsorbed peroxide and hydroperoxides.[5]

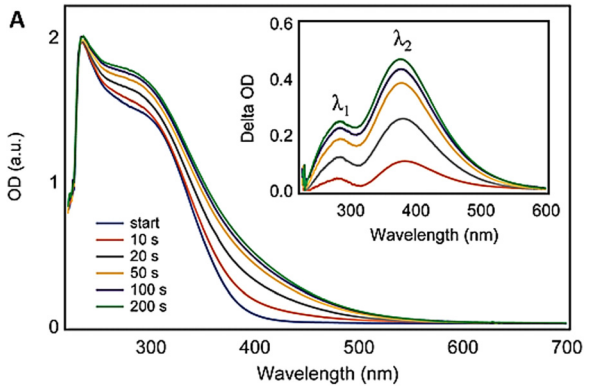


Fig. 14 UV-Vis spectra of the CeNPs dispersion treated with $H_2O_2$ obtained as a function of time. Reproduced from ref. 232 with permission from the Royal Society of Chemistry.

### 2.7. Dissolution of ceria-based systems as a promising strategy for regeneration

Every year, large quantities of ceria-based materials are used in TWC converters in automotive exhausts and CMP of dielectric films during integrated circuit (IC) fabrication. Recent reports suggest record high increases in the price of cerium-based materials due to more stringent export rules of the world's largest producer of rare earth materials and scarcity of cerium materials.[233,234] A threefold approach, which includes recycling and reuse of these materials and development of alternative materials having less hazardous ecological impacts, has been proposed. The selective dissolution of ceria-based systems appears as a promising strategy to recover cerium; hence, thorough knowledge about the fundamental aspects of ceria dissolution is essential.[235] Herein, we review the methods proposed for ceria dissolution and the impact of several parameters on dissolution.

The dissolution of ceria is not thermodynamically favorable ($\Delta_r G^\circ$ = 40 kJ $mol^{-1}$) even in concentrated mineral acid solutions.[236,237] However, the reductive dissolution of ceria is feasible due to the highly positive redox potential of the $Ce^{4+}/Ce^{3+}$ couple (1.4 V per SHE).[238] A solution containing a very strong mineral acid and a reducing agent can effectively dissolve ceria.[239] While any strong mineral acid can be used, sulfuric acid and nitric acid are especially known to be effective towards ceria dissolution. As far as reducing agent is concerned, a green reducing agent like ascorbic acid, citric acid, or oxalic acid would be very advantageous. Choosing the appropriate mineral acid and the reducing agent is paramount since mixing a mineral acid with reducing agents like $H_2O_2$

(which acts as a reducing agent under highly acidic pH conditions) is an exothermic reaction and hence deleterious.

Early work on ceria dissolution was reported in patents on cleaning ceria particles after polishing glass or silicon dioxide films with slurries containing ceria particles and other chemical additives. Mitani and Saito proposed compositions containing an acid and a reducing agent to clean ceria particles adhered to glass substrates after CMP.[240] Several reducing agents were tested in solutions containing sulfuric acid/nitric acid to enhance the dissolution of ceria particles. A solution containing 0.1 M $HNO_3$ and 1 M $H_2O_2$ yielded the highest dissolution rate. However, the pH of the solutions containing $H_2SO_4/HNO_3$ and $H_2O_2$ was very low ($<0$); hence, such compositions caused problems with subsequently deposited materials during IC fabrication and corroded the polymeric brushes used for post-CMP cleaning. Later, significant efforts were made to developing cleaning compositions that were compatible with the consumables (polymeric pads and brushes) used for post-CMP cleaning process. Avanzino and Shonauer proposed cleaning compositions containing a reducing agent (like phosphorus acid, hypophosphoric acid, oxalic acid and L-ascorbic acid) and a complexing agent (like ascorbic acid, citric acid, tartaric acid, malic acid and glutamic acid) for removing ceria particles on silicon dioxide and silicon nitride films.[241] In an embodiment of their invention, they showed that the dissolution of ceria particles increased with the increase in phosphorus acid and ascorbic acid concentrations chosen as prototype additives.

Of all the mineral acids, nitric acid and sulfuric acid are known to yield high dissolution rates.[242] The dissolution rate in the presence of acids increases with acid concentration. Temperature has a strong influence on dissolution, and the dissolution rate increases gradually with the rise in temperature.[243,244] Several studies have reported an enhancement in dissolution rate by ~3–4 orders of magnitude between 20 °C and 90 °C. The surface of ceria reacts with $H^+$ ions in solution and the particle surface area decreases due to the reduction in particle radius with time.[242] The dissolution of ceria in dilute $HNO_3$ or $H_2SO_4$ can be catalyzed by Pt NPs. Ultrasound energy can also boost the dissolution of ceria in various solutions.[238] pH has a significant impact on ceria dissolution, and the dissolution is significant only below pH 5.[245] The dissolution rate of ceria, however, is independent of the mixing rate. The dissolution of ceria in nitric acid is controlled by chemical reaction and not by diffusion as the dissolution rate did not change with the mixing rate.[244]

The dissolution of CeNPs depends strongly on the chemical composition. For instance, the incorporation of 10% trivalent lanthanide ions increased the dissolution rate by an order of magnitude,[243] as shown in Fig. 15a. The crystal lattice weakening because of oxygen vacancies formed to balance the charge deficit after the incorporation of lanthanide ions was found to be the key reason for the increase in the dissolution rate. The modification of the crystal structure of ceria did not lead to any change in the dissolution rate. While an increase in temperature and concentration of acid increased the dissolution rate by one and half orders of magnitude, respectively, changing the reducing agent did not have any impact on the dissolution rate, as shown in Fig. 15a. Beaudoux *et al.* showed that ceria particles can be dissolved at room temperature in a mixture of ascorbic acid and a dilute mineral acid.[237] The dissolution rate of ceria particles having a specific surface area of 15 $m^2\ g^{-1}$ increased with the concentration of sulfuric acid or nitric acid in a solution containing 0.5 M ascorbic acid, as shown in Fig. 15b. Ceria particles having different specific surface areas, *i.e.*, different particle sizes, showed significantly different dissolution rates.[237] Regardless of the different conditions employed, CeNPs were completely dissolved in 0.5 M ascorbic acid and dilute nitric acid or sulfuric acid. A three-step mechanism is proposed for the dissolution process in ascorbic acid and nitric acid mixture. The first step involves the adsorption of reducing agent on the reactive $Ce^{3+}$ surface sites on ceria. The second step is the reduction of Ce ions from $Ce^{4+}$ to $Ce^{3+}$ by the reducing agent, and the third step involves the release of $Ce^{3+}$ species *via* Ce–O bound acid hydrolyses.

Recently, the dynamics of dissolution of CeNPs using *in situ* liquid cell TEM coupled with high intensity electron-beam

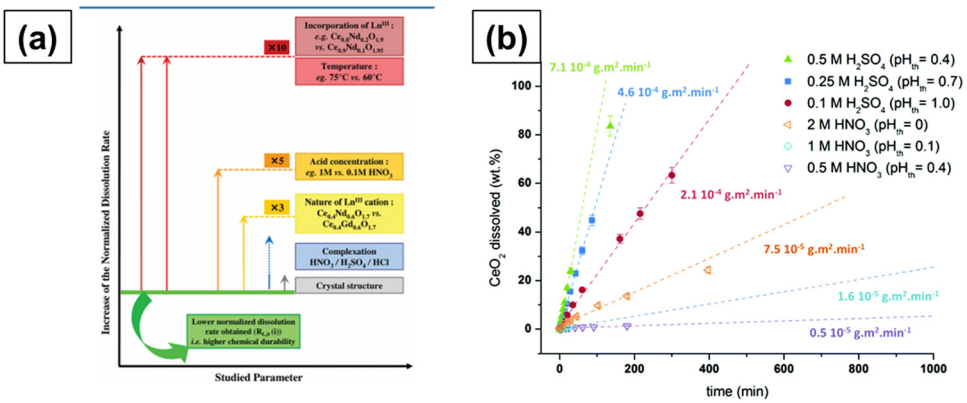


Fig. 15 (a) Effect of different physicochemical parameters on the dissolution rate of $Ce_{1-x}Ln_xO_{2-x/2}$. Reprinted with permission from ref. 243. Copyright 2012 American Chemical Society. (b) Effect of acid concentration on the dissolution rate of ceria particles in a solution containing 0.5 M ascorbic acid. Reproduced from ref. 237 with permission from the Royal Society of Chemistry.

 

irradiation of nanoparticle dispersions[246] were studied. Very high dissolution rates, exceeding previously reported values at room temperature by several orders of magnitude, were reported by the authors. It was suggested that the radicals, ions and electrons were generated by electron–water interaction and that these species assist in the reductive dissolution of CeNPs. Several procedures have been demonstrated for recovering cerium from post-polish CMP slurry. The recovery process involves selectively dissolving ceria in a mixture containing nitric acid and $H_2O_2$.[247–250] Cerium from the solution is precipitated post-dissolution as cerium(III) carbonate, which is subsequently converted into ceria by annealing in a rotary kiln. However, the dissolution rates reported in most of the studies are too low to consider any practical application.

Evidently, severe conditions are required to dissolve CeNPs. Published research suggests that sulfuric acid and nitric acid yield high dissolution rates than other mineral acids. There are many unanswered questions regarding this topic; hence, there is still a need to understand the dissolution of CeNPs from a fundamental perspective. In particular, it is pivotal to study the effect of the preparation method, particle size and surface coating, among other factors, on the dissolution of ceria particles as the results of these experiments would provide some valuable insights relevant to the dissolution of ceria particles used in commercial applications.

# 3. Controlled synthesis of ceria-based hybrid nanomaterials

The synthesis conditions and the ability to control the surface properties are essential aspects influencing the morphology, crystallinity and surface chemistry of CeNPs, ultimately dictating their catalytic, redox and other functional properties. Variations in ceria surface have been obtained by incorporating of a variety of ligands or by binding or mixing them to form composite hybrid structures with other molecules. The size of ceria nanocrystals and variations in their morphologies play a critical role in determining the surface oxidation states, the $CeO_{2-x}$ stoichiometry, stability and catalytic performance.[73,251] Various synthesis methods have been employed to tailor these properties, ranging from classical precipitation routes[252] to more advanced methods such as hydrothermal,[253] sol–gel[254] and microwave-assisted synthesis.[255] The selection of solvents and capping agents is also essential, particularly for achieving ultrasmall CeNPs. For example, ultrasmall ($2.5 \pm 0.2$ nm) mixed valence state ($Ce^{3+}/Ce^{4+}$) CeNPs have been obtained *via* a direct room temperature synthesis using ethylenediamine as a capping agent.[256] The ultimate choice of the method governs the size, shape and surface functions. Surface functionalization techniques including doping with other metals or metal oxides or organic ligands, surface oxidation/reduction treatments and deposition of metal NPs[257] allow for tailoring the surface chemistry and electronic structure to enhance the catalytic activity, stability and dispersibility in various media. More recent advances include the use of green solvents and biosynthesis methods to produce less toxic NPs compatible with living tissues.[258] Furthermore, post synthesis treatments such as annealing, calcination or reduction can modify surface defects, oxygen vacancy concentration, and surface area, thus affecting the redox behavior and reactivity.[259]

Such modifications generate novel interesting properties, allowing them to be used in a variety of applications. Many emerging applications of CeNPs in biomedicine, sensing and environment require surface functionalization to make them biocompatible for target binding and molecular recognition. However, the interfacial behavior of functional particles is sensitive to changes in the environment such as pH, ionic strength, temperature, natural organic materials, and concentration, often leading to aggregation,[260] and many functionalized NPs exhibit differential behavior and reactivity profiles for practical applications. In this section, we highlight the most common strategies to create functional CeNPs and CeNPs-based hybrid materials (Fig. 16). In particular, CeNPs used in conjunction with carbon-based materials, polymers, metal organic frameworks (MOFs), metals and metal oxides, and supramolecular assemblies are particularly attractive due to their chemical structures, tailorability and synergistic properties, enabling the effective utilization of these materials in different applications.

### 3.1. Ceria–carbon nanostructures

CeNPs stabilized on the surface of carbon-based materials such as graphene (GR), graphene oxide (GO) and carbon nanotubes (CNT) have enabled the design of a new class of hybrid two-dimensional materials that combine the catalytic properties of ceria with the large surface area and conductivity of carbon-based nanostructures. Graphene has been extensively studied due to its excellent electrical mobility, extremely large specific surface area, high thermal conductivity, and mechanical properties.[261] Two different procedures can be used to control the synthesis and graft CeNPs on graphene-based nanostructures. The first involves the adsorption of the precursor salt on the surface of the graphene matrix, followed by the *in situ* growth of the NPs with control of the size and shapes. The second consists of the anchoring or deposition of the as-synthesized CeNPs onto the surface of the graphene matrix (self-assembly approach).[262] $CeO_2$–graphene nanostructures synthesized using a single step (*in situ* growth) hydrothermal method demonstrated the ability to control growth of CeNPs on graphene sheets (Fig. 17). The combination of defects in CeNPs with an optimal amount of two-dimensional graphene sheets had a significant effect on the properties of the resulting hybrid, providing improved optical, photocatalytic, and photocapacitive performance.[263]

The intercalation of CeNPs within the layers of graphene nanosheets allowed the nanosheets to maintain their high surface area and prevent reduced graphene oxide (RGO) from restacking.[264] Anchoring crystalline ceria onto RGO sheets revealed strong electrostatic interaction between the ceria NPs and RGO. Therefore, the interaction of mobile holes and the increased density of the oxygen vacancies from $Ce^{4+}$ to $Ce^{3+}$ in

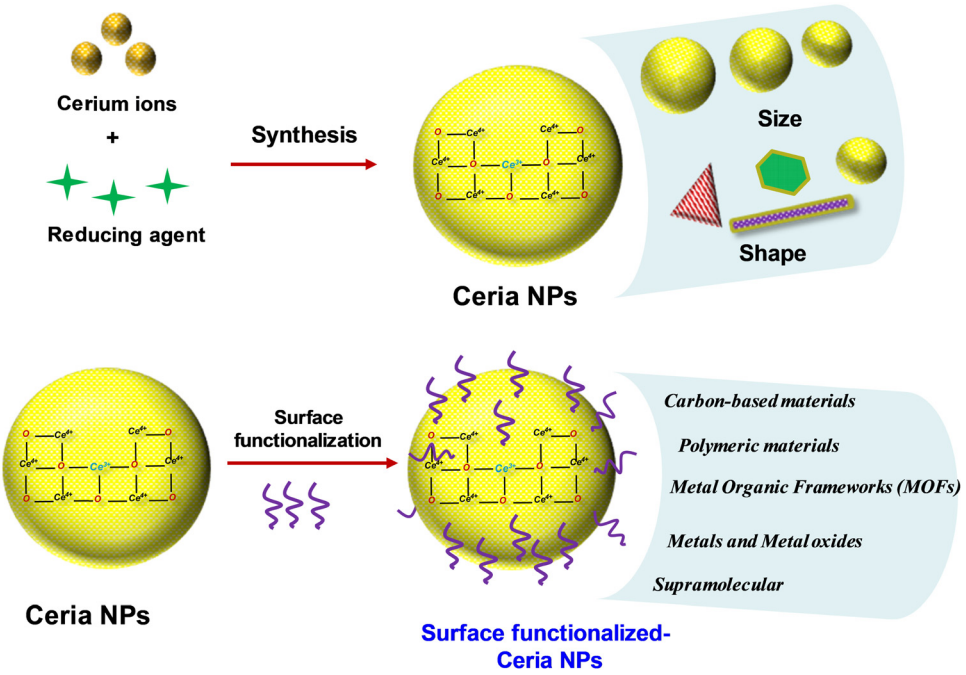


Fig. 16 Representation of the modular synthesis of CeNPs, with size and morphology control, and the surface functionalization and creation of hybrid structures with various types of materials.

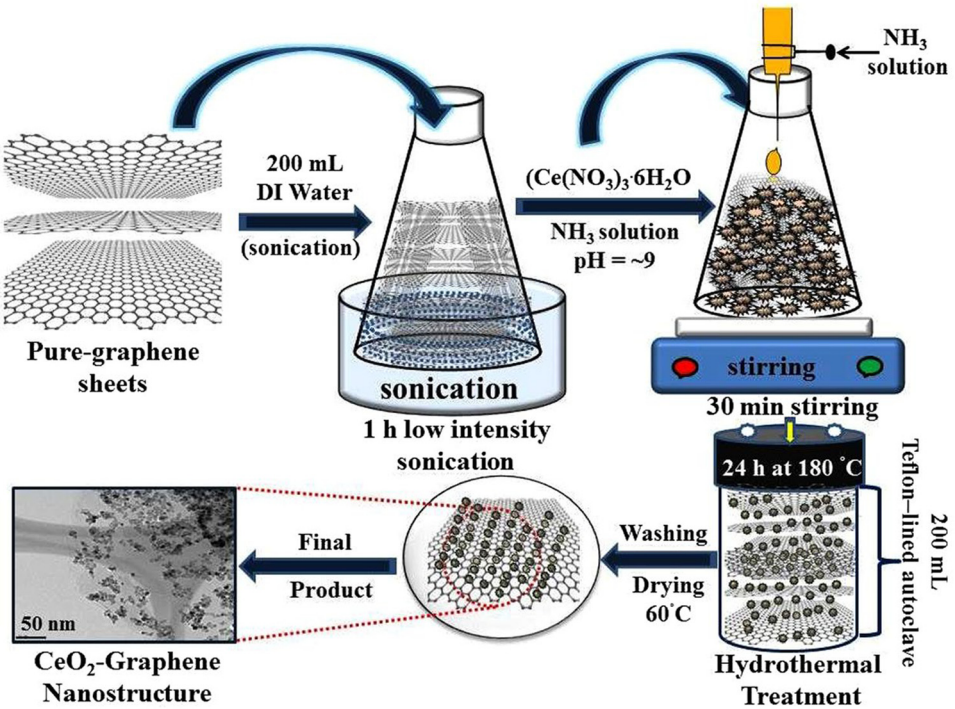


Fig. 17 Schematic representation for the synthesis steps of the $CeO_2$–graphene nanostructures. Reprinted from ref. 263.

the RGO resulted in a transformation in the n-type $CeO_2$–RGO composites, which are suitable for applications in energy devices, batteries and sensors.[265] Li *et al.*[266] utilized an *in situ* growth method to synthesize a $CeO_2$–graphene nanocomposite, which showed a specific capacitance of 208 F $g^{-1}$ and a maximum power density of 18 kW $kg^{-1}$ in supercapacitors. Dezfuli *et al.*[264] developed $CeO_2$–RGO nanocomposite electrodes, which exhibited excellent supercapacitive behavior with high specific capacitance (211 F $g^{-1}$ at 2 mV $s^{-1}$ and 185 F $g^{-1}$ at 2.0 A $g^{-1}$) and reversibility. Combining the redox

 

characteristics of CeNPs with graphene is an effective approach to design materials for redox supercapacitors.[266] However, their wide band gap semiconductor (~3.4 eV) limits their use as an electronic material and photocatalyst.[267] Tuning the band structure by chemical functionalization or attachment to conducting supports is an excellent method to enable their implementation in electronic and optical applications. In particular, defects, such as oxygen vacancies, generate localized electrons on the $CeO_2$ surface, which may interact with the functional group in the RGO sheets, thus improving the properties of RGO.[268] Such composites also show high adsorption capacities as adsorbent materials for preventing environmental pollution with contaminants such as heavy metal ions and phosphates, thus enabling applications in environmental remediation.[269] To improve the selectivity (towards cationic or anionic species), sorption capacity, and overcome limitations such as the leaching of the NPs or stacking of the C-sheets, the surface of these materials can be modified to enable specific applications. For example hydrous ceria-modified graphene has been used as a novel adsorbent for arsenic removal from aqueous solutions.[270] In other works, GO decorated with ceria showed selectivity in determination of trace metal ions and speciation of selenium.[271] Ceria-GO composites fabricated using one-pot synthesis exhibited an almost complete (>99.9%) and quick removal of arsenic species within 0.1 mg $L^{-1}$ of the initial concentration.[272] Additional uses have been demonstrated for preparing ceria-carbon based catalysts for solid oxide fuel cells (SOFCs) and field effect transistors. The chemical vapor deposition (CVD) growth of single-walled carbon nanotubes (SWNTs) is normally performed at 800–1000 °C.[273] When $CeO_2$, which stores oxygen, was used, the ceria-supported catalyst enabled the selective growth of SWCNTs on substrates due to the oxidative environment provided by the ceria.[274]

### 3.2. Polymeric ceria-based hybrid materials

The combination of the metal oxide NPs with polymers is increasingly used to overcome limitations such as NP aggregation, dispersibility, lack of specificity for reactions in complex systems, and weak mechanical strength.[275] The properties of such hybrid materials depend on the nature of the guest NPs and the structure and the functional groups of the host polymer. This approach allows tuning the composition, surface functionality, and colloidal stability of the dispersed NPs. Colloidal carrier systems or so-called smart carrier systems, such as thermosensitive microgels, have been developed, which encapsulate and stabilize the particles.[276] Polymeric materials are commonly used to stabilize CeNPs for applications in biomedicine. However, the surface charge and their surface functionalization have been found to play a critical role in their uptake mechanism and subcellular localization. Results with CeNP functionalized with different polymeric coatings (poly(acrylic acid), aminated poly(acrylic acid) or dextran, Fig. 18), endowing positive, negative or neutral changes, showed that CeNPs with a positive or neutral charge enters

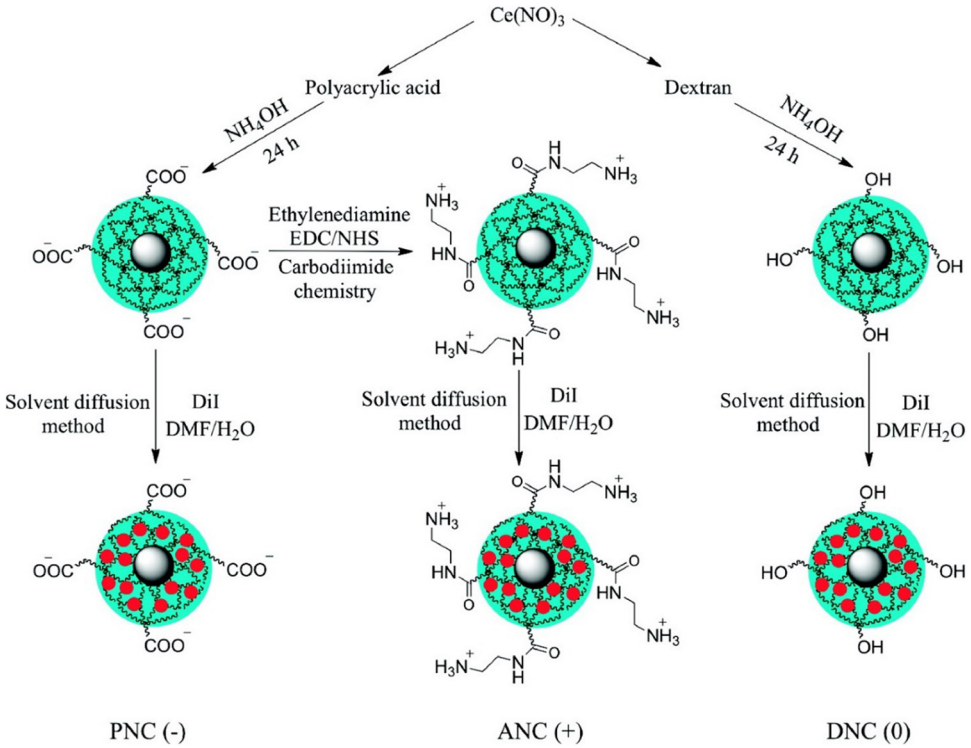


Fig. 18 Surface functionalization of ceria NPs with different polymer coatings and surface modifications were synthesized to yield nanoparticles with negative [PNC(−)], positive [ANC(+)], and neutral [DNC(0)] charge, where PNC is poly(acrylic acid), ANC is aminated poly(acrylic acid) and DNC is dextran. A fluorescent dye (DiI, red circle) was encapsulated using a modified solvent diffusion method (reprinted with permission from ref. 277. Copyright 2010 American Chemical Society).

most cells, while those negatively charged internalize mostly in cancer cell lines.[277] In other works, polymers like polyethylene glycol and polyvynilpyrrolidone create functionalized CeNPs with biocompatible coatings that show enhanced autophagic clearance.[278] Recent advances in the surface functionalization of ceria involve green synthesis methods using room-temperature aqueous and solvent-free solutions. CeNPs prepared by metal-free organocatalyzed photoinduced electron transfer radical polymerization (O-PET-ATRP) generated zwitterion-functionalized NPs that retained their shape and prevented protein adsorption. The resulting passivation of the particle surface generated higher uptake and enhanced redox properties under physiological conditions. The functionalization using this environment-friendly approach directly enhanced the intracellular delivery for cancer therapeutics.[279]

Polymers can also be used to fabricate hybrid CeNPs–polymer composites in which the polymer acts as a supporting material or dispersing agent. CeNPs can also be crystallized in a controlled manner on the surface of polymer NPs.[280] Hybrid polymeric core–shell nanoparticles, *i.e.*, CeNPs/polystyrene nanocapsules containing a model fluorophore with encapsulated fluorescent dyes, were developed by free radical microemulsion polymerization.[281] The use of CeNPs generated a significant enhancement of the fluorescence properties by suppressing the quenching of the encapsulated dye by molecular oxygen. Cellulose, a sustainable and renewable biopolymer, was used to incorporate CeNPs to obtain transparent films with UV shielding properties.[282]

Other studies have shown the use of coordination polymers employing lanthanide ions instead of d-block metal ions to generate supramolecular architectures with distinctive structures and accessible metal coordination sites.283,284 Using a sonochemical method, NPs of a Ce(III) supramolecular compound with fluorescent proepties have been synthesized as a precursor for nanoceria.[285] Polymeric materials can be used to facilitate the self-assembly of NPs and create structured supramolecular assemblies.[260,286] The surface of CeNPs has been shown to form stable surface complexes with molecules incorporating phosphate, phosphonate, or carboxylate moiety.[287] Several reports demonstated the synthesis of CeNPs using coordination polymers with tunable shell tickness and surface functions.[284,288–290]

### 3.3. Ceria-based metal organic frameworks

Metal–organic frameworks (MOFs) have emerged as a promising class of materials for gas storage, gas purification and separations, and catalysis.[291] A large number of organic linkers and metal ions provide versatility for creating tailorable structures with open metal sites that can act as catalytic or binding sites for a variety of reactions. Stabilizing CeNPs within MOF frameworks can be used as an effective strategy to enhance their reactivity by preventing aggregation and providing high accessibility to the catalytic sites through the open channels. A cerium-MOF based on MIL-125 with open-metal sites[292] was shown to retain the porosity and enhance the overall adsorption of $SO_2$ and $CO_2$. The synthesis of Ce(IV)-based UiO-66

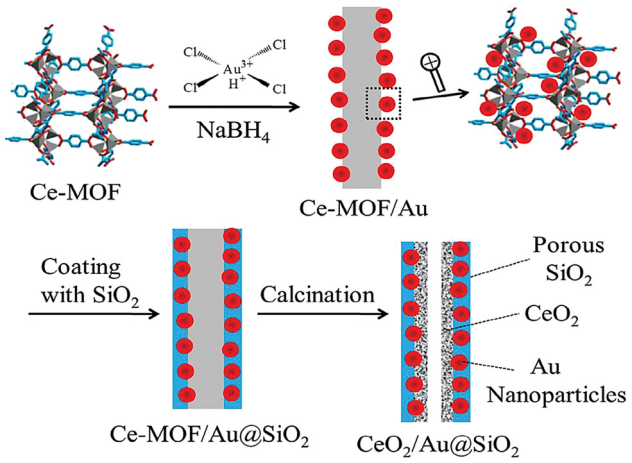


Fig. 19 The synthesis procedure for the $CeO_2$/Au@$SiO_2$ nanocomposites. Reproduced from ref. 299 with permission from the Royal Society of Chemistry.

(referred to as Ce-BDC) with different pore sizes and functionalities was reported to stabilize the $[Ce_6O_4(OH)_4]^{12+}$ cluster during MOF formation, preventing metal-hydroxo precipitation.[293,294]

Several studies have been reported on introducing Ce to the MOF framework by doping to increase the number of active sites for gas adsorption. Ce-doped MOF ((Ce-UiO-66(Zr))) exhibits over 25% increase in the amount of $NO_2$ adsorbed under dry conditions in comparison with the unmodified MOF.[295] Support materials or core shell structures have been shown to improve the catalytic activity of CeNPs.[296] Kim *et al.*[297] developed a simple method to synthesize nanoporous $CeO_2$ by the thermal conversion of aliphatic carboxylate ligand-based Ce-MOF into hierarchical metal oxides with nanocrystalline frameworks. It was found that the pore size of the prepared framework could be tuned, providing an increase in the adsorption capacity. A 3D network $CeO_2$-M was prepared by a Ce-MOF-template method and $K^+$, doping which resulted in an increased oxygen species and superior adsorption and oxygen storage capacity of ceria.[298] The solid catalyst was evaluated for *o*-xylene oxidation at low temperature. Inspired by these studies, a new generation of porous CeNPs/Au@$SiO_2$ core–shell nanocatalysts has been prepared by the pyrolysis of Ce-based MOFs (Fig. 19).[299] The $CeO_2$/Au@$SiO_2$ catalysts possess a porous nanotube structure, resulting in high catalytic activity for the reduction of 4-nitrophenol.

The enhanced reactivity of CeNPs can be obtained by creating ultrasmall (1–2 nm) CeNPs within a Ce-MOF *via* the *in situ* etching of the parent NPs (Fig. 20). This strategy enhanced the activity of the CeNPs by preventing NP aggregation, stabilizing them in a dispersed form within the porous framework.[300] At the same time, the guest molecule has high accessibility to the active sites through the porous network. The resulting CeNPs-MOF showed fast degradation kinetics of the nerve agent, *p*-nitrophenylphosphate (DMNP), providing superior activity as compared to the parent CeNPs. The ability of the $CeO_2$-MOF to degrade DMNP was explained by the increased abundance of $Ce^{3+}/Ce^{4+}$ neighboring sites and oxygen vacancies, facilitating

 

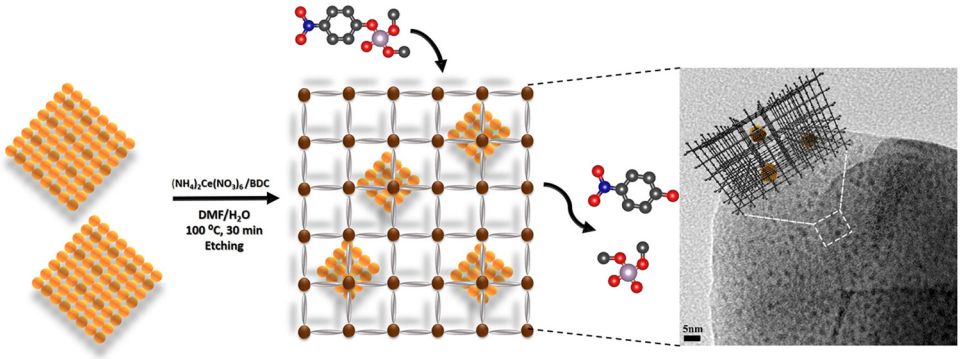


Fig. 20 Schematic of CeNPs immobilization inside Ce-MOF for DMNP degradation and the subsequent CeNP–MOF structure analysed by TEM (reprinted with permission from ref. 300. Copyright 2020 American Chemical Society).



the nucleophilic attack of the hydroxyl groups of the DMNP phosphate, leading to P–O bond cleavage and further degradation. This method provides a strategy to enhance the reactivity of CeNPs, making them more effective catalysts.

### 3.4. Ceria-based metals and metal oxides heterostructures

Noble metals (M) and metal oxides (MO) can be used in conjunction with CeNPs to create hybrid materials with lower cost and superior characteristics for applications. For example, platinum-group metals, Pd, Rh and Pt, serve as active species in TWA exhaust catalysts and the price of these metals represents around 40% of the manufacturing cost of the catalysts.[301] Reducing the use of expensive Pt Pt-MO heterostructures has been explored. Enhanced activity can be obtained by encapsulating noble metals inside ceria, *e.g.*, Pt@$CeO_2$ core–shell hybrid structures, or by loading the MNPs on the surface of hollow $CeO_2$ nanostructures. This strategy has been used to create a variety of Au, Pt, Ag@$CeO_2$ hybrid nanostructures,[302,303] providing enhanced catalytic activity by stabilizing small size noble metal NPs and creating hybrid junctions at the two-phase interface.[304] Doping CeNPs with metals has emerged as a promising approach to produce supported catalysts with atomically dispersed metals.[305] The size, morphology, stability and catalytic activity of these materials can be controlled by varying the dopant, ligand used and the reducing and oxidizing conditions. Studies to assess the effects of metal dopants on the reducibility of bulk and extended surfaces of CeNPs have been extensively reported using both experimental and theoretical approaches.[142,158,306,307]

The enhanced properties provided by these hybrid materials have found unique applications in catalysis, environmental remediation, sensing and biomedicine. For example, Ag@$CeO_2$ has demonstrated the inactivation of *Escherichia coli* through the formation of reactive oxygen species (ROS).[308] Similarly, $CeO_2$–CdO binary metal oxide nanocomposites showed antibacterial activity and growth inhibition towards *P. aeruginosa*.[309] The properties of CeNPs were also integrated with the photoinduced electron transfer of quantum dots (QDs), providing materials with significantly improved optoelectronic properties. A synthesized ceria–carbon quantum dots/RGO nanohybrid showed improved photocatalytic properties, enabling the rapid decomposition of organic pollutants.[310]

## 4. Applications and future directions

The unique properties of nanoscale ceria quickly inspired their translation in a variety of applications. The broad applicability and versatility are a consequence of the redox properties of CeNPs originating from the presence of oxygen vacancies and the $Ce^{3+}/Ce^{4+}$ mixed valence states. As a result, CeNPs are increasingly used in applications such as catalysis, chemical mechanical polishing, fuel cells, oxygen sensors, ultraviolet absorbents, sensing and biosensing, drug delivery and biomedical diagnostics.[311–316] In the following sections, we provide examples of the representative use cases of CeNPs in catalysis, chemical mechanical polishing, chemical sensing and biosensing, and environmental remediation.

### 4.1. Catalysis

The thermal stability, high OSC and proton transfer abilities make CeNPs particularly useful in catalysis.165,317 The $3^+/4^+$ reversibility and oxygen mobility, which is higher compared with other oxides such as $SiO_2$, $Al_2O_3$, and $ZrO_2$, enable the use of CeNPs as a catalyst in redox, CO oxidation, and acid–base reactions[3,318,319] among others. The main concerns related to CeNPs are related to the deterioration of the active surface area due to sintering and segregation processes, resulting in the loss of catalytic activity.[320] Therefore, much attention has been paid to develop CeNP-based catalysts with enhanced structural characteristics to resist degradation, such as combining binary metal oxide catalysts. For example, $CeO_2$–$MnO_2$ showed enhanced performance for processes such as CO oxidation,[321] selective catalytic reduction of $NO_x$ with $NH_3$,[322] and the oxidation of volatile organic compounds.[323] Further optimization has been accomplished using a Ce-based MOF to maximize the exposed active sites and enhance the porosity of the system.[324] Ceria is an excellent support for high-performance metallic catalysts, enhancing the stability and catalytic performance, as shown for example with PtFe nanocrystals hybridized by $CeO_x$, *e.g.*, PtFe–$Pt_xFe_yCe_zO_j$.[12] A particular case is the use of

mesoporous ceria, characterized by well-defined pores, typically ranging from 2 to 50 nm, and a high surface area, which provides unique capabilities for catalysis,[325] gas sensing and energy storage. The high surface area provides enhanced accessibility to active sites and facilitates the transport of reactants and products. Additionally, the oxygen vacancies facilitate switching between $CeO_2$ and $CeO_{2-x}$. Therefore, they showed improved performance in catalytic reactions including oxidation, hydrogenation and pollutant removal. A review summarizing the synthesis and catalytic applications of mesoporous ceria can be found in the ref. 325.

Doping CeNPs with transition metals or rare earth metal such as Cu, Cr, Ti, Y, and La have been adopted as a promising approach to tune the catalytic activity of these materials.[326–330] The substitution process causes structural defects and creates more oxygen vacancies on the catalyst surface, which affects the generation and mobility of charged species such as electrons and oxygen anions. Furthermore, doped ceria can also tolerate high temperature annealing treatments due to the cooperative nature of the cations of the binary oxides.[331] The electronegativity and ionic radius of $Ce^{4+}$ are 1.12 and 0.97 Å, respectively. A synergetic dopant would ideally have electronegativity and ionic radius close to these numbers. For instance, samarium (Sm) has an electronegativity and ionic radius of 1.17 and 1.07 Å, respectively. It is also soluble in the ceria sublattice and can stabilize the fluorite structure of ceria at low dopant concentration. A nanocrystalline $CeO_2$–$Sm_2O_3$ (CS) solid solution has been easily synthesized, yielding a promising catalyst for the oxidation of CO at lower temperatures owing to the large number of lattice defects, high OSC and improved redox properties.[331] Sm-doped $CeO_2$ nanopostructures have been widely used as a catalyst in methane selective oxidation,[332] allylic oxidation[333] and fuel cells applications,[334] while Gd-doped $CeO_2$ was used for gas sensing applications.[335] The Gd-doped $CeO_2$ gas sensor had better sensitivity, good stability and lower operating temperature over the nondoped one with a detection concentration of 800 ppm $CO_2$ gas. In addition, Ni-doped CeNPs have been hydrothermally prepared and showed an increased magnetization and electrical conductivity with increasing dopant concentration.[336]

As diesel emission produces soot, which have grown concerns for human health and the environment, several emission control strategies have been implemented to reduce environmental impact.[337] For example, over 90% of soot can be trapped and then be continuously or periodically combusted to $CO_2$ using the diesel particulate filter (DPF) technology. However, the periodic regeneration of DPF is not passive, which makes it complex and expensive. Ceria-based materials have been developed to decrease the soot combustion temperature ($\sim$600 °C compared to diesel exhaust temperature ($\sim$175–400 °C)) and have been extensively studied as catalysts and catalysts promoter in this research area.[338] Nascimento *et al.*[339] studied the performance of binary oxides $CeO_x/FeO_y$ catalysts modified with AgNPs for the control of diesel soot combustion. Catalytic tests showed a significant reduction of about 300 °C in the soot oxidation temperature with $CeO_x/FeO_y$ compared to $CeO_2$. Shen *et al.*[340] also investigated the catalytic performances of Fe-doped ceria catalysts with diffeent Fe contents for the soot oxidation reaction with $O_2$ or $O_2$/NO gases. They demonstrated that the addition of iron increased the number of oxygen vacancies on the surface and therefore the catalytic activities for NO oxidation and $NO_2$-assisted soot combustion.

Uniform anchoring/decoration of CeNPs on the surface of graphene sheets improves the photocatalytic and photocapacitive performance of the nanostructures for effective charge transfer and catalytic degradation processes.[263] For example, the photocatalytic activity was examined by monitoring their ability to degrade Congo red $\sim$94.5% and methylene blue dye $\sim$98% under visible light irradiation. These developments indicate the broad applicability of CeNPs-based nanostructures for future energy and environment-related applications.

### 4.2. Chemical mechanical planarization (CMP)

CMP is a surface smoothing process that is used in the semiconductor fabrication process and in a number of other manufacturing processes. It has become a critical and enabling process for the multilevel metallization necessary for interconnecting the immense number of active devices created on silicon substrates and in the device fabrication process sequence at the gate level.[312,341] Silicon dioxide CMP, or simply oxide CMP, in which a colloidal slurry consisting of ceria abrasives is commonly used, is one of the many critical processes in the fabrication of integrated circuits (ICs).[341–344] CeNPs are widely used as abrasives for oxide CMP since they interact strongly with the oxide, leading to high removal rates (RRs). With appropriate additives to ceria slurry, it is possible to achieve a highly selective polishing of the oxide with respect to the underlying silicon nitride films, as required in the planarization of shallow trench isolation structures.[344–346] $Ce^{3+}$ species present on the surface of CeNPs particles react with the hydrated oxide surface (Si–$O^-$), forming strong Ce–O–Si bonds and ultimately rupturing the underlying and weaker bonds in the oxide film, leading to its continual removal.[344,347,348] There are extensive discussions of the reaction mechanisms involved in the polishing of oxide and nitride films.[344,349,350]

Two methods, namely, solid-state displacement and solution-growth, are commonly used for the preparation of CeNPs particles for CMP applications.[341,351] In the solid-state displacement method, particles are prepared by calcining cerium carbonate at more than 600 °C under controlled air flow conditions, which is subsequently wet milled to obtain the desired particle size.[352] CeNPs with less than 100 nm size can be obtained by controlling the pre-treatment of cerium salt, calcination temperature, air flow conditions, and bead size of the milling process.[352–354] However, the particles produced by this method are faceted and have sharp edges, corners, and apexes as well as a very wide size distribution (Fig. 21a). These features tend to scratch the films during polishing and generate many unacceptable defects. Consequently, the usage of these types of particles is being avoided, while the solution-grown $CeO_2$ particles, despite of their higher cost and potential for contamination, have gained wider acceptance.[87,355,356]

 

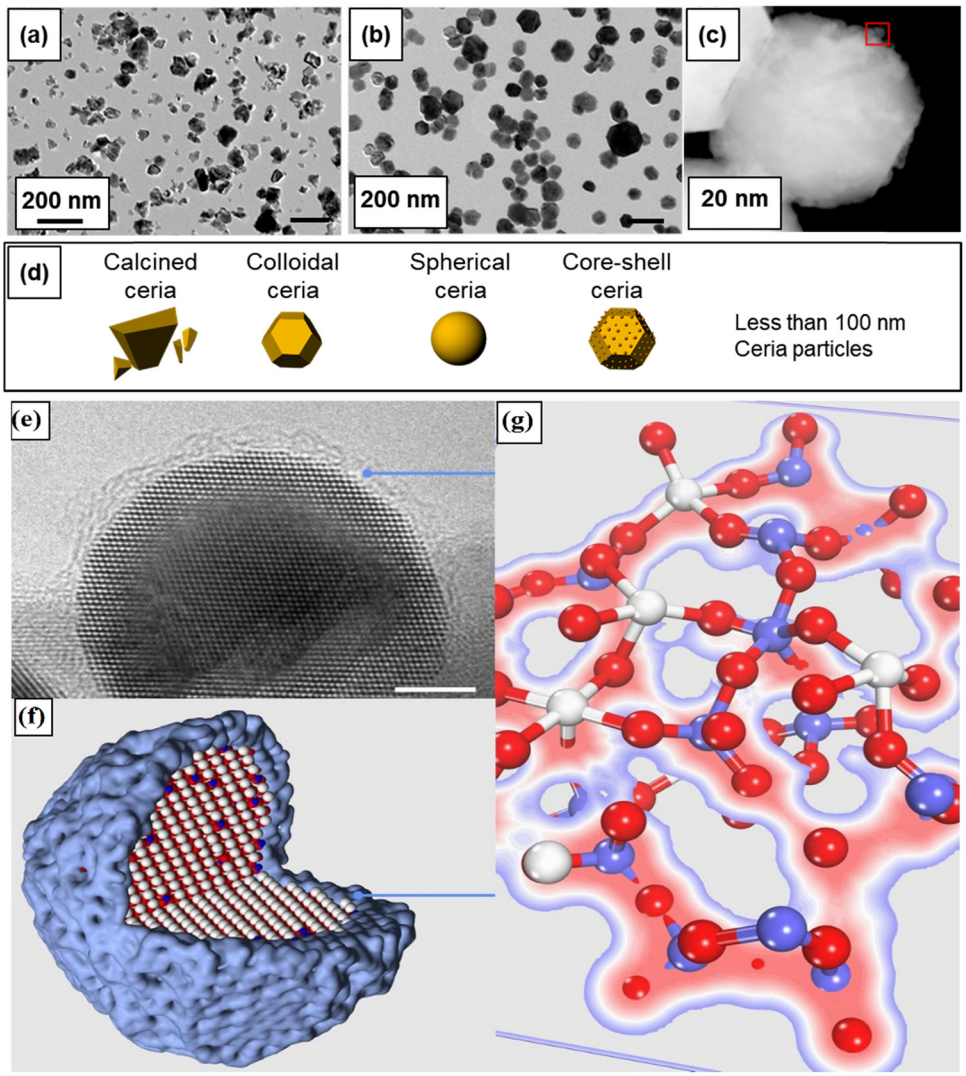


Fig. 21 Different types of CeNPs used in recent CMP slurries; (a) calcined ceria, (b) colloidal ceria, and (c) core/shell ceria particle, and (d) their schematic illustration. HRTEM image of Ti-doped ceria single-crystalline nanoparticle (e), model of a Ti-doped $CeO_2$ sphere (f), and a molecular model of the $TiO_2$ amorphous shell on the nanoparticle (g). (a) and (b) Reprinted with permission from ref. 351. Copyright 2014 American Chemical Society. (c) reprinted with permission from ref. 364. (e) and (f) Reprinted with permission from ref. 371.

In the solution growth method, cerium hydroxide ($Ce(OH)_3$) is precipitated from a solution of cerium nitrate mixed with ammonium hydroxide and transformed to $CeO_2$ in the presence of oxygen ($Ce(OH)_3 + 1/2O_2 \rightarrow CeO_2(s) + 3H_2O$). These particles are separated and washed repeatedly for removing residual precursors until the desired conductivity of the suspension is obtained.[357,358] Particles with a very narrow size distribution can be produced by this method, as shown in Fig. 21b. These relatively uniform-sized CeNP abrasives have polyhedral and nearly spherical shape, which is expected to minimize the generation of scratches because of fewer sharp edges and corners.

Coating ceria abrasives with a layer of different materials and chemical compositions makes it is possible to change the physicochemical properties of the core abrasive, including the shape, surface chemistry, surface charge, porosity, and hardness, and can be tailored to increase their reactivity with films. To benefit from this strategy, core/shell type $CeO_2$ abrasives have been investigated and have showed increased removal rates as well as improved surface roughness of polished oxide films. Core/shell structured composite particles, comprising of mesoporous silica,[359,360] dendritic silica,[361] polymethylmethacrylate (PMMA),[362] and polystyrene (PS)[363] as core materials with metal-doped $CeO_2$ particles making up the shell, generated relatively high oxide removal rates with low surface scratch and roughness values. This was ascribed to the resilient spring-like effect of the softer core silica during polishing. Also, since smaller particles tend to produce a higher quality surface finish, the coating of core $CeO_2$ particles ($\sim$100 nm) with a layer of smaller (5 nm or so) $CeO_2$ shell has been proposed and was shown to achieve high oxide polish rates (Fig. 21c).[364] In principle, these types of composite abrasives can result in

significant cost savings for high volume manufacturing due to the higher throughput, lower abrasive concentrations, and lower waste treatment cost. However, all these composite ceria abrasives are prone to form broken particles as well as peeling-off and/or brittle collapse of the shells. Therefore, further advancements in the field are necessary to avoid these issues. Various types and shapes of pure and composite $CeO_2$ particles used in most CMP slurry formulations are summarized in Fig. 21d.

As NAND technology has evolved from 2D planar to 3D vertical, new CMP steps with higher planarization efficiencies and much higher oxide polish rates have become necessary. This is due to the larger initial step heights and much thicker dielectric layers than those in conventional ILD or STI CMP.[365–367] To meet these challenges, CeNPs-based slurries having the necessary very high oxide polish rates need to be developed. One of the current development approaches is to prepare $Ce^{3+}$-rich $CeO_2$ particles through either metal-doping or coating. Doping with lanthanide (La, Sm, Gd, Nd, and Yb) elements increases $Ce^{3+}$ concentration by increasing oxygen vacancies at the surface, thus enhancing the removal rates of the oxide film.[368–370] Praveen *et al.* reported that La-doped $CeO_2$ particles showed ~20% higher removal rates of $SiO_2$ films when compared to the non-doped $CeO_2$ particles.[368] Similarly, Cheng *et al.* showed that Nd doping increases $Ce^{3+}$ concentration on the particles surface and thus produced ~30% higher removal rates of the oxide film at pH 9.5.[369] The removal rates of oxide films were well correlated with $Ce^{3+}$ concentrations in metal-doped particles. For example, Feng *et al.* prepared single-crystal Ti-doped CeNPs spheres with a size distribution of 50–150 nm through the liquid-phase flame spray pyrolysis of solutions of cerium and titanium precursors.[371] The $CeO_2$ core of the particles were encapsulated by a 1–2 nm shell of $TiO_2$ to minimize the surface energy, resulting in a nearly spherical morphology (Fig. 21e–g). The polishing results showed that these particles reduced the CMP-caused defects by 80% and increased the removal rates of the oxide film by 50%.[371]

### 4.3. Chemical and biological sensing

The field of chemical sensors and biosensors has witnessed a radical transformation due to the rapid advancement and innovations in functional materials and biomaterials. Metal oxide nanomaterials can serve for both recognition and transduction purposes[372] alone or in conjunction with biomolecules such as DNA or enzymes. Enzyme-based sensors are considered to be one of the most reliable sensing techniques due to their high sensitivity, selectivity and fast response.[373–375] However, an enzyme's stability can be severely compromised with temperature and pH changes. For these reasons, researchers have focused on using nanotechnology tools to develop more robust sensors by engineering materials that mimic the function and complexities of natural enzymes.[376–379] Metals and metal oxides NPs and nanocomposites,[374,380,381] metal organic frameworks,[382,383] and carbon-based nanomaterials[384–386] have demonstrated promising potential as artificial nanoenzymes[195] with peroxidase or oxidase-like mimetic activity, which could be used as receptors or transduction materials for sensing.

CeNPs have emerged as a promising enzyme-mimetic material that possesses intrinsic oxidase or peroxidase-like properties due to the mixed oxidation states ($Ce^{3+}/Ce^{4+}$), which provides the ability to catalyze many chemical and biologically relevant reactions.[375] Upon the reduction of $Ce^{4+}$ to $Ce^{3+}$, the CeNPs mimics catalase activity by inducing $H_2O_2$ oxidation, generating molecular $O_2$. On the contrary, oxidation of $Ce^{3+}$ to $Ce^{4+}$ mimics superoxide dismutase (SOD) activity by reducing $O_2^-$ to $H_2O_2$. The efficiency of CeNPs as a peroxidase mimic is strongly dependent on the low ratio of ($Ce^{3+}/Ce^{4+}$).[387] The high catalytic activity, oxygen rich surface and low toxicity175 make them excellent candidates for enzyme-mimetic and enzyme immobilization purposes.[229,388] Furthermore, CeNPs have been used as a material with therapeutic potential to reduce harmful ROS/RNS due to the unique regenerative ability to scavenge ROS/RNS species.[200,389] The combination of sensing and therapeutic functions makes CeNPs a powerful theranostic platform for biomedical applications.[26,390] An ROS-scavenging tissue adhesive nanocomposite was synthesized by immobilizing ultrasmall ceria nanocrystals on the surface of uniform mesoporous silica (MSN).[391] The ceria nanocrystals-decorated MSN does not only have a strong tissue adhesion strength but they also help minimize the ROS-mediated deleterious effects, thus efficiently accelerating the wound healing process, as evidenced by marked skin appendage morphogenesis and limited scar formation.

Various studies have shown the ability of CeNPs to reduce symptoms of oxidative stress-related diseases, such as chronic inflammation,[392] endometriosis,[393] cancer,[394,395] and diabetes.[396,397] However, with the diversity of methods and synthetic procedures used to synthesize these particles, each producing different types, shapes, sizes, coatings and $Ce^{4+}/Ce^{3+}$ ratios, the antioxidant effects can vary significantly. Controlling the surface chemistry to efficiently regulate the reducing and oxidizing efficiency (*e.g.*, antioxidant *vs.* pro-oxidant) in biological systems remains a challenge, as is the tendency of CeNPs to agglomerate in biological fluids.[170] In some cases, CeNPs have been found toxic, but the mechanism responsible for CeNPs toxicity, if present, is still inclear and subject to debate.[11] Therefore, it is important to develop new kinds of CeNPs with high dispersibility and enhanced catalytic activity that are able to maintain their redox properties in biological fluids. Several strategies have been reported in the literature to improve these properties. For example, CeNPs have been coupled with materials such as $Cu_2O$,[398] $TiO_2$,[399] and Eu[400,401] to enhance their catalytic and enzyme mimetic properties. The use of CeNPs in conjunction with $TiO_2$ nanotubes increased the peroxidase mimetic activity.[402] In another study, adding Eu to the nanocrystal structure imparted fluorescence and increased the oxidase-like activity of ultra-small (2–5 nm diameter) CeNPs.[400] The decoration of graphene sheets with metal oxide NPs such as CeNPs improved the mechanical, electrical and thermal properties of both materials. In this hybrid structure, CeNPs have a wide band gap (3.4 eV) with a

 

high isoelectric point (IEP, 9.0) and excellent enzyme binding ability,[403] while graphene has high electrical conductivity. Therefore, CeNP–graphene composites that synergistically combine the electrical conductivity of graphene with the catalytic properties of CeNPs are excellent materials for electrochemical biosensors. The CeNP-reduced graphene oxide ($CeO_2$–rGO) composite prepared by a facile one-pot hydrothermal method used in combination with horseradish peroxidase (HRP) enabled the detection of $H_2O_2$ at very low levels. The CeNPs–rGO composite provided a well-defined microenvironment for HRP immobilization and enhanced the direct electron transfer (DET) between the enzyme and the $CeO_2$–rGO at the electrode surface, significantly improving performance for $H_2O_2$ detection. Other works reported a 100-fold increase in the oxidase mimicking activity of naked CeNPs particles by fluoride capping. This mechanism has been used for the ultrasensitive sensing of fluoride (0.64 μM).[404]

Hybrid nanomaterials offer several advantages for chemical sensing and biosensing due to their ability to provide synergistic catalytic functions due to the formation of hybrid junctions associated with rich redox reactions, thus enhancing their catalytic performance.[373] Artificial intelligence and machine learning, through the use of computer-aided designs of the CeNPs, could in the future be used to screen and rationally design particles with the desired properties for applications.[406,407] Using these tools, it is now possible to predict the optimal CeNP shape that delivers the best catalytic performance in some specific reactions.[406] For instance, the facet engineering of CeNPs with the help of computational calculations made it possible to understand the crystal facet effect that plays a crucial role in determining the surface energy and reactivity.[408] $CeO_2$ nanorods with a dominant (110) facet showed the highest peroxidase-mimetic activity due to the rich defect chemistry on their surface (Fig. 22). These studies provided an increased understanding of the fundamental CeNPs properties that drive their unique reactivity. This knowledge is essential to rationally design and tailor their activity.

Several types of chemical and biological sensing systems where CeNPs have been used as receptors for gases, enzyme mimetic materials, co-catalyst or as a label for quantifying affinity recognition reactions have been developed (Fig. 23). Applications include gas, biomimetic or enzyme-based sensors, immuno, aptamer and DNA-based sensors. Examples for each of these classes are discussed in the section below.

**4.3.1. Gas sensing.** Semiconductor metal oxides are well known candidates for gas-sensing applications due to their high sensitivity for the adsorption of gases.[409] The gas-sensing mechanism is based on the adsorption of target molecules, generating changes on the material's conductivity at the oxide surface, though a dynamic process mediated by oxygen vacancies and subsurface defects.[410] In many such applications, the CeNPs are typically used as a support for metals like Pt or Au. CeNPs-based sensors have been designed for the detection of carbon dioxide,[411] acetone,[412] nitrogen dioxide and sulfur dioxide.[413] Because the electrical conductivity of CeNPs is a function of the oxygen partial pressure, ceria-based NPs, nanostructures and thin films can be used as oxygen sensors.[414] Nanostructured ceria also showed response towards different humidity levels and therefore can be used to fabricate humidity sensors by measuring the resistance variation upon exposure to moisture.[415] High surface area truncated octahedral CeNPs with a higher level of $Ce^{4+}$ ions exhibited the highest humidity sensing with a response time of 10 s.

Highly porous yolk–shell CeNP nanospheres prepared by microwave-assisted solvothermal synthesis showed a two times

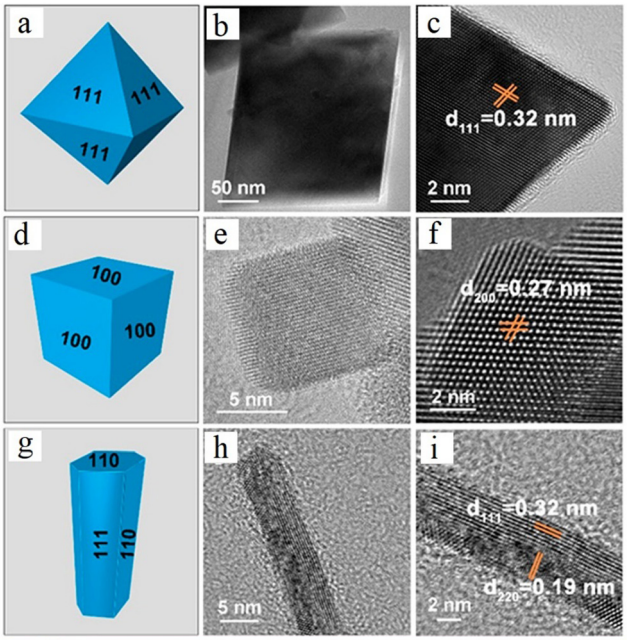


Fig. 22 $CeO_2$ with different shapes and exposed facets (a)–(i), and $H_2O_2$ detection scheme using HRP/$CeO_2$–rGO-modified glassy carbon electrode (j). Reprinted with permission from ref. 405. Copyright 2022 American Chemical Society.

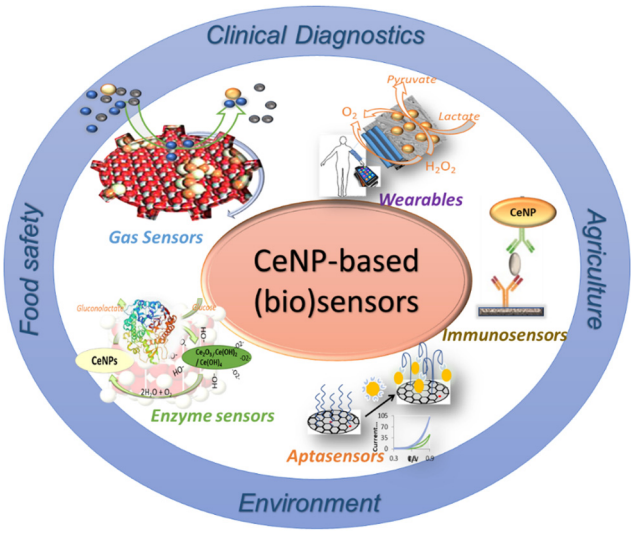


Fig. 23 Summary of chemical sensing and biosensing involving CeNPs-based materials and their applications.

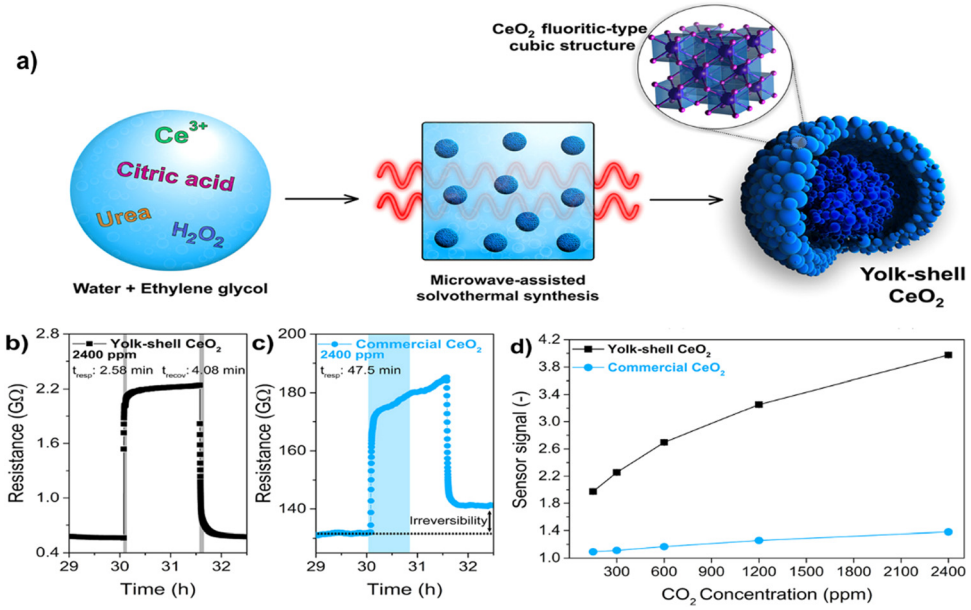


Fig. 24 Microwave-assisted solvothermal synthesis of yolk–shell CeNPs (a), response and recovery times to 2400 ppm of the sensor prepaid with yolk–shell CeNPs (b) as compared to the commercial CeNPs (c), and comparative sensor signal in response to $CO_2$ concentrations (d) (reprinted with permission from ref. 411. Copyright 2020 American Chemical Society).

increase in the sensitivity for $CO_2$ detection as compared to commercial CeNPs (Fig. 24) due to increased porosity and permeability for gas adsorption though the hollow structure.[411] Similar structures were used to build sensors for acetone, with detection in the ppm concentration range, and a response and recovery time of 6 and 11 s, respectively.[412] The doping of CeNPs with lanthanum was shown to strongly influence the redox ($Ce^{3+}/Ce^{4+}$) ratio and gas adsorption properties for CO. Under optimized conditions, the sensor provided fast response at a temperature of 380 °C under CO exposure associated with $Ce^{4+}$ reduction and vacancy generation.[416]

**4.3.2. Enzyme mimetics and enzymatic biosensors.** CeNPs have been widely investigated to fabricate enzyme mimetic and enzyme–CeNPs-based biosensors with colorimetric or electrochemical detection.224,417 These sensors use CeNPs either as an enzyme mimetic (*e.g.*, as a synthetic replacement of a natural enzyme)[418] or co-immobilized with a natural enzyme to catalytically amplify the enzymatic reactions[419] and therefore enhance their detection sensitivity. As compared to systems based solely on biocatalytic enzymes (*e.g.*, oxidases or peroxidases), sensors based on CeNPs are more robust, inexpensive and not susceptible to denaturation.

Sensors with optical detection measure changes in the optical properties associated with redox processes at the CeNPs surface. It is known that CeNPs form charge transfer complexes with $H_2O_2$[224] and catecholate compounds,[420] generating a distinctive concentration-dependent optical response. Based on these principles, a variety of colorimetric sensors have been reported using CeNPs as color-generating probes (*e.g.*, as a replacement to commonly used soluble dyes) or to enhance the colorimetric signals of redox dyes such as 3,3′,5,5,-tetramethylbenzidine (TMB) or azino-bis(3-ethylbenzothiazoline-6-sulfonic acid) (ABTS). The high stability and rich surface functionalities of the CeNPs makes them amenable to patterning on solid surfaces, providing opportunities for the development of portable and inexpensive sensors.

One of the first demonstration of CeNPs as colorimetric probes was reported in 2011 for the detection of $H_2O_2$ and oxidase enzyme substrates such as glucose.[224] The advantage of this system over conventional colorimetric assays is evident when comparing the two types of assays in Fig. 25A and B. When CeNPs is used as a color probe and peroxidase mimetic, in the presence of $H_2O_2$, the while/yellowish color of the CeNPs changes into bright yellow/orange due to the oxidation of $Ce^{3+}$ to $Ce^{4+}$ and formation of peroxide-Ce complexes at the NP surface, producing a unique concentration-dependent response.[224] When CeNPs are co-immobilized with glucose oxidase on filter paper, $H_2O_2$ is generated on exposure to glucose, and the enzymatically generated $H_2O_2$ is then measured as a color change. Conventional enzyme-based colorimetric assays for oxidase enzymes involve the use of two enzymes, one for the conversion of substrate to $H_2O_2$ (*e.g.*, glucoseoxidase), and one for the conversion of the enzymatically generated $H_2O_2$, typically a peroxidase, and a soluble redox dye. Because these reagents are soluble, they are generally used in solution or stored on specially designed reservoirs with reactions being accomplished though microfluidic channels. Conventional dyes are expensive and maintaining their stability is a challenge. Since CeNPs is a stable inorganic material that can replace both the peroxidase enzyme and the organic dye, they can be easily affixed to a solid platform such as paper, plastic or textiles for creating stand-alone portable sensors. Such reagent-less sensors have significantly enhanced the stability and portability and are low-cost as compared to solution-based assays (Fig. 25C). For example, a CeNP-based

 

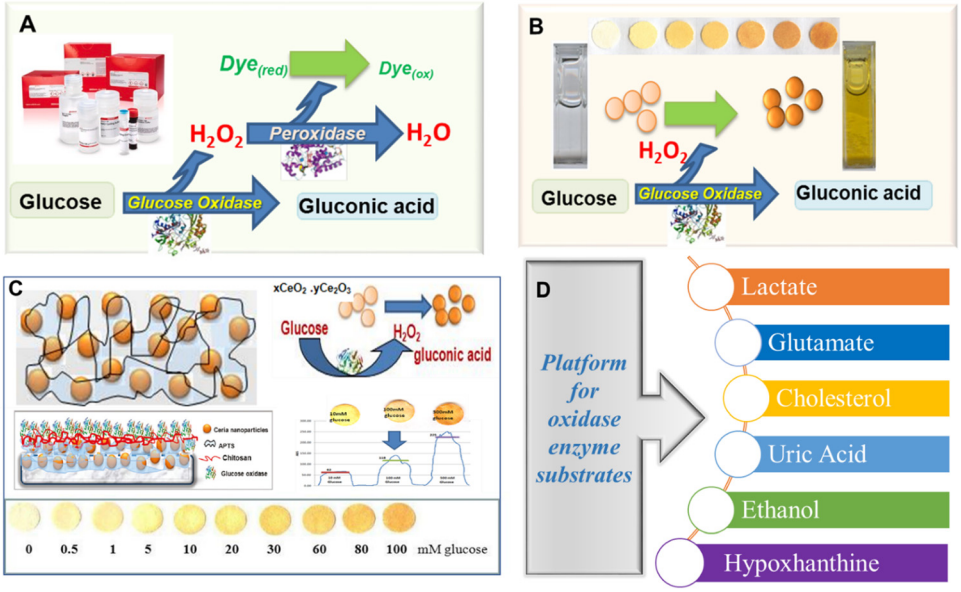


Fig. 25 Detection of glucose using glucose oxidase (GOx) enzyme by conventional colorimetric assay with GOx, peroxidase and a redox dye (A) and the CeNP-based sensor (B). Immobilization of CeNPs on paper using 3-aminopropyltriethoxysilane (APTS) and chitosan biopolymer and ImageJ quantification of biosensor response (C) with examples of biosensor targets developed based on CeNPs used as colorimetric probes (A, B reproduced with permission from ref. 224. Copyright 2011 American Chemical Society).

biosensor for glucose developed on filter paper displayed a limit of detection of 0.5 mM with a linear range up to 100 mM glucose. This concept can be extended as a general platform for any oxidase enzyme system that involves the generation of $H_2O_2$ as a reaction product, such as lactate, glutamate, cholesterol, uric acid, ethanol and hypoxhantine (Fig. 25D).

Similar types of colorimetric sensors based on CeNPs have been designed to detect enzyme activities, such as alkaline phosphatase (ALP). For example, a CeNPs-based sensor was developed based on the color changes of CeNPs reacting with hydrolytic products of ALP-catalyzed reactions, from substrates such as catechol monophosphate, ascorbic 2-phosphate and hydroquinone diphosphate. The method, adapted to a paper-based platform, had a detection limit of 0.04 U $L^{-1}$ ALP with a linear range up to 2 U $L^{-1}$when ascorbic 2-phosphate was used as the substrate.[421] More recently, the activity of beta-galactosidase (beta-Gal) was determined using a procedure involving CeNP-induced oxidation of 4-aminophenol (4-AP) produced in the hydrolysis of the 4-aminophenyl-beta-D-galactopyranoside substrate (4-APG) by beta-Gal. The approach enhanced the detection sensitivity and enabled beta-Gal measurements in the visible range, reaching a detection limit of 0.06 U $L^{-1}$ and a linear range up to 2.0 U $L^{-1}$. A 30-fold amplification as compared to a commercially available beta-Gal assay was reported using the CeNP assay.[422] In addition to colorimetric sensors, opportunities exist to design CeNP-based fluorescence and imaging assays by doping CeNPs with Eu. For example, Eu-doped CeNPs (5 nm diameter doped with 2% Eu) exhibit bright and stable fluorescence in aqueous media (Fig. 26). Their combined catalysis and fluorescent properties can serve as a universal concept to design fluorescent assays with the ability to monitor enzymatic reactions and quantify enzymatic activity and substrates such as AlP activity, dopamine, glucose and lactate with increased selectivity and sensitivity.[400]

The distinctive changes in the optical properties of the CeNPs reacting with compounds with phenolic or catecholoamine moieties were used to develop paper-based sensors for the detection of phenolic antioxidants, with the reported detection limits in the range of 20–400 μM, depending on the structure of the compound. These sensors have the capability to provide a unique optical signature generated when CeNPs interact with a single or a mixture of antioxidants. The method enabled field assessment and classification of the antioxidant capacity in tea,[423] wine,[424] medical mushrooms[425] and cosmetic products.[426] For these measurements, the CeNPs stabilized onto a paper platform form the actual sensing platform (*e.g.*, sensing spot or label), enabling portability and reagentless operation. Similar to a pH paper, analysis is performed by adding the sample to the sensor; the antioxidants in the sample produce an immediate color change that is visible to the naked eye. Quantification is achieved by comparison with a pre-calibrated detection scheme. For more precise quantification, analysis can be performed with a color reader such as a cell phone with a color reading app; no additional reagents are needed (other than the sample). In comparison with other assays for antioxidant analysis, the CeNPs sensors have very low cost and are stable at room temperature and field deployable. Finally, biosensing systems based on CeNPs have practical utility, as demonstrated by the development of several standalone devices for the detection of ethanol in breath,[427] phenolic antioxidants for evaluating antioxidant activity in teas and

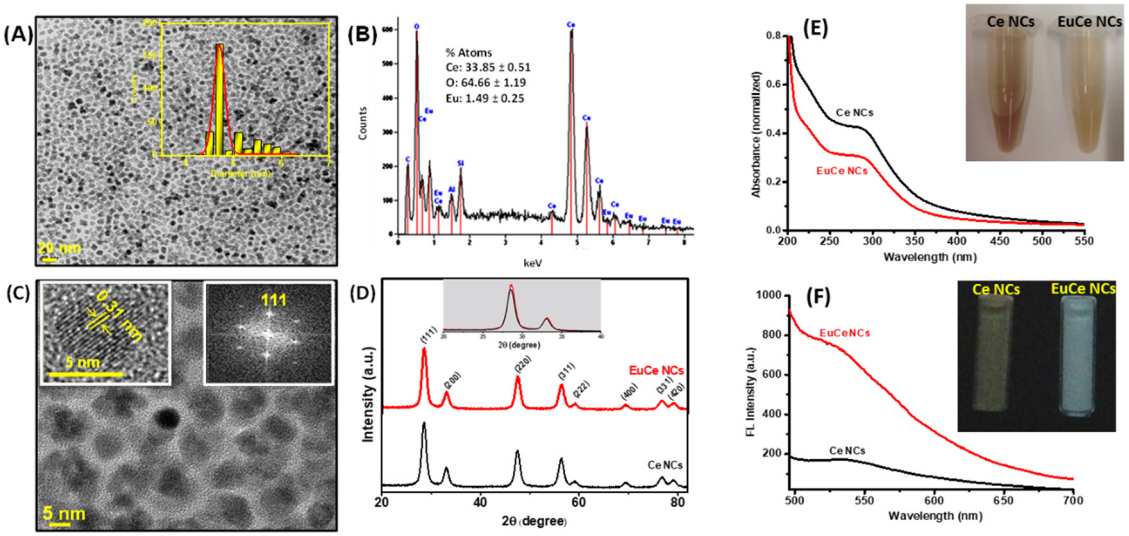


Fig. 26 Morphological, structural and catalytic activity characterization of Eu-doped CeNPs, (A) The HR-TEM (inset: particle size distribution). (B) EDX, (C) HR-TEM at high magnification (inset: dimension of single spherical particle (left) and electron diffraction (right)), (D) XRD patterns of CeNPs and Eu-CeNPs. (E) UV-vis spectra of CeNPs and Eu-CeNPs showing emission at $\lambda_{ex}$, 466 nm, and $\lambda_{em}$ 522 nm, inset: photographs of Eu-CeNPs under UV (365 nm) (reprinted with permission from ref. 400. Copyright 2018 American Chemical Society).

wines,[425] and measuring the hypoxanthine content to assess the freshness of fish and meat,[428] are summarized in Fig. 27.

Several hybrid configurations of CeNPs-based enzyme biosensors have been developed in which the CeNPs are used in conjunction with oxidase enzymes to catalytically amplify the enzymatic reaction or the product of an enzymatic reaction, significantly enhancing the sensitivity of the biosensor. Moreover, the ability of the CeNPs to store and release oxygen has been used as an oxygen reservoir to fuel oxygen to oxidase enzymes, enabling them to operate in oxygen-restrictive environments such as tissue hypoxia. This principle has been demonstrated effectively for improving the sensitivity of implantable electrochemical microbiosensors fabricated by co-immobilizing the enzyme with the CeNPs at the surface of a microelectrode, typically a Pt wire or a carbon fiber brush, with diameters ranging from 100 to 150 μm. Successful developments have been demonstrated with CeNPs-based biosensors for the detection of dopamine,[429] glutamate,[430] lactate[431] and glucose.[432] Enhanced selectivity has been obtained with Pt-doped CeNPs, which imparts conductivity and amplifies the electrocatalytic signal for $H_2O_2$ oxidation, as shown in Fig. 28A for glucose detection. The lactate biosensor, for example, had a detection limit of 37 μM in implantable conditions and was able to quantify the real time release of lactate *in vivo* during cerebral ischemia and reperfusion (Fig. 28B).[431] This lactate biosensor operated in a continuous mode due to the ability of the enzymatically generated $H_2O_2$ to react with the CeNPs, producing oxygen in the process. This released oxygen is then utilized by the enzyme, facilitating its functionality in the hypoxic medium. Notable, the biosensors without CeNPs do not provide any quantifiable response due to the lack of oxygen, a necessary cofactor for ensuring enzyme function. Other possibilities to enhance the conductivity for electrochemical biosensors are to use the CeNP in conjunction with graphene oxide and PtNPs,[433] conductive polymers such as polyaniline,[434] or mesoporous carbon,[435] leading to enhanced

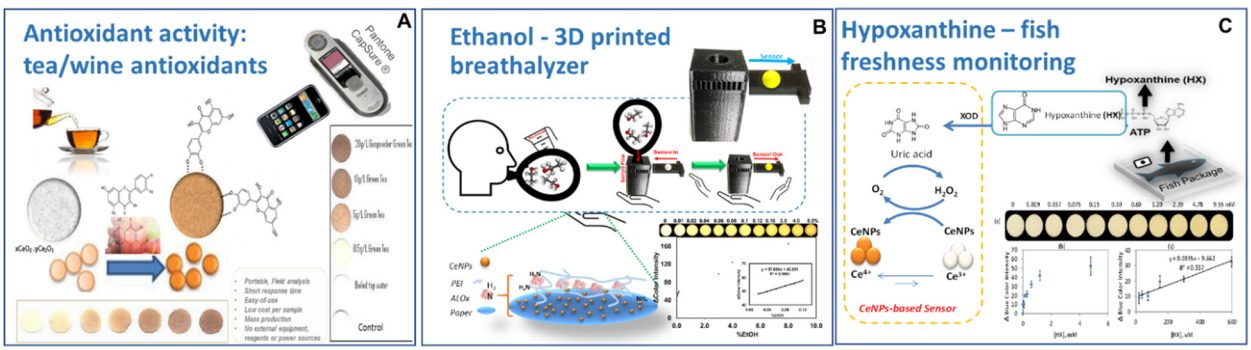


Fig. 27 Examples of practical CeNP-based paper sensors for the detection of antioxidant activity in tea (A), ethanol in breath using a 3D printed device (B) and hypoxanthine to assess the freshness of fish (C). Reprinted with permission from Refs for (A),[425] (B)[427] and (C).[428] Copyright 2021 American Chemical Society.

 

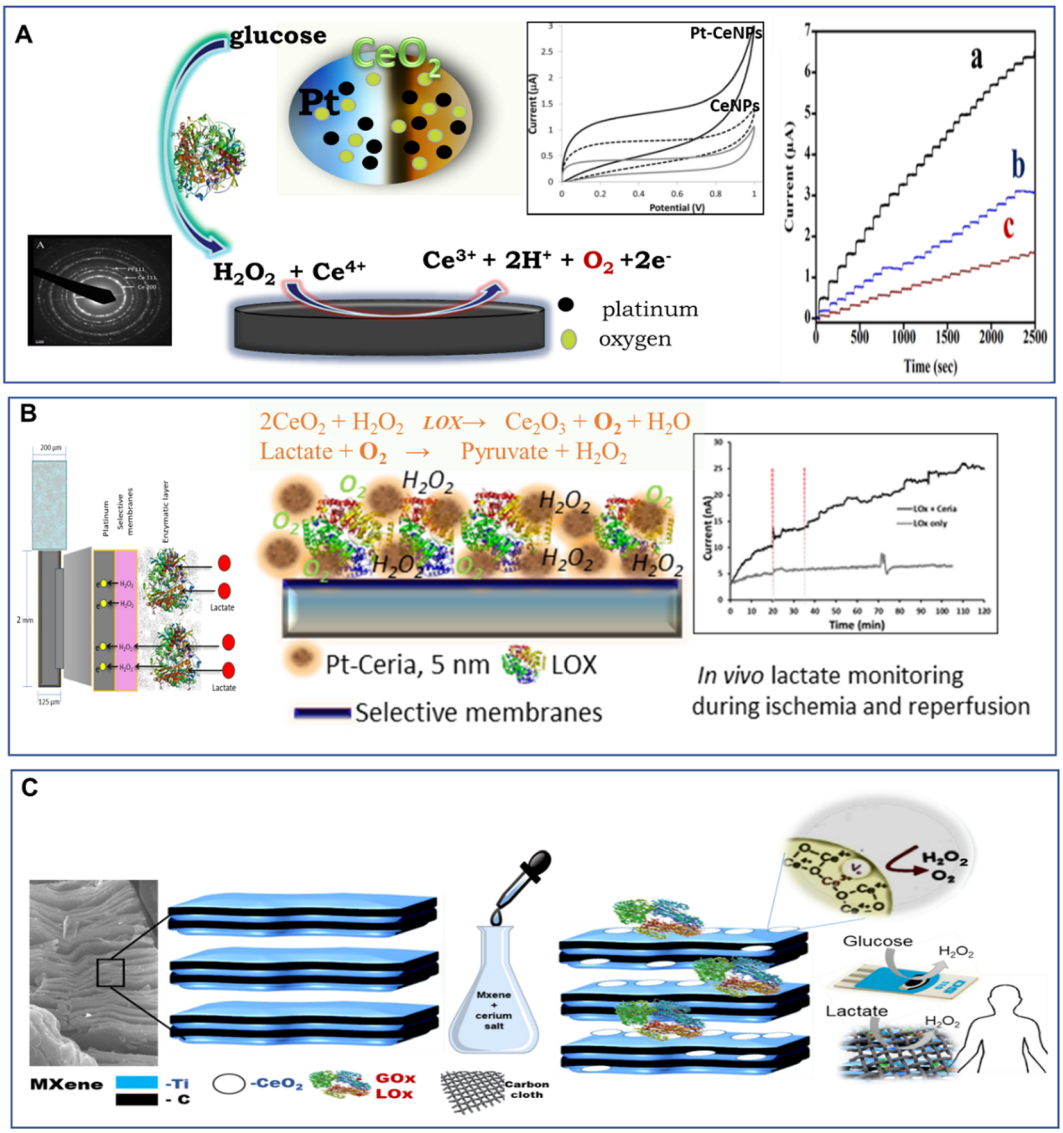


Fig. 28 (A) Electrochemical CeNP-based implantable microbiosensors using Pt-doped CeNP (5 nm), which electrocatalyzes $H_2O_2$ oxidation, further enhancing glucose detection; significantly enhanced responses were obtained when Pt–CeNPs were used (a) as compared to bare CeNPs, (b) or no CeNPs (c) (with permission from ref. 432); (B) implantable microbiosensor configuration for lactate detection during ischemia and reperfusion showing quantifiable responses when Pt-doped CeNPs were immobilized with lactate oxidase (reprinted with permission from ref. 431. Copyright 2015 American Chemical Society.); (C) catalytic MXene-CeNPs biosensing platform for wearable biosensors (with permission from ref. 437).

sensitivities. CeNPs can also be designed in the form of a dual-tethered nanosystem in conjunction with fullerene, which combines the properties of the two materials, leading to hybrid structures with high antioxidant and UV-shielding properties.[436]

Lastly, significant improvements can be achieved by interfacing CeNPs with high surface area materials such as 2D layered MXenes, producing catalytically active materials that can be used in a variety of applications. In a recent work (Fig. 28C), MXene decorated with CeNPs enabled the development of an electrochemical biosensor platform broadly applied to a variety of enzymes and enzyme substrates, achieving detection limits of 0.8 μM $H_2O_2$, 0.49 μM glucose, 3.6 μM lactate and 1.7 μM hypoxanthine.[437] These materials can be integrated within flexible platforms such as carbon cloth and be used to construct wearable devices, as demonstrated for lactate monitoring in sweat.[437]

**4.3.3. Affinity-based biosensors.** CeNPs have been widely used to create affinity biosensors based on interactions of immuno, DNA or aptamer receptors and their targets at the CeNPs surface or using CeNPs as an enzyme-mimetic label in solution or deposited on electrode surfaces. The examples of general strategies of CeNP-based affinity sensors are shown in Fig. 29. Colorimetric assays use the enzyme-mimicking activity of the CeNPs and their ability to react with dyes such as TMB to quantify affinity binding interactions. For example, the CeNPs's oxidase-like activity enabled the electrochemical detection of DNA amplicons by taking advantage of the electrostatic

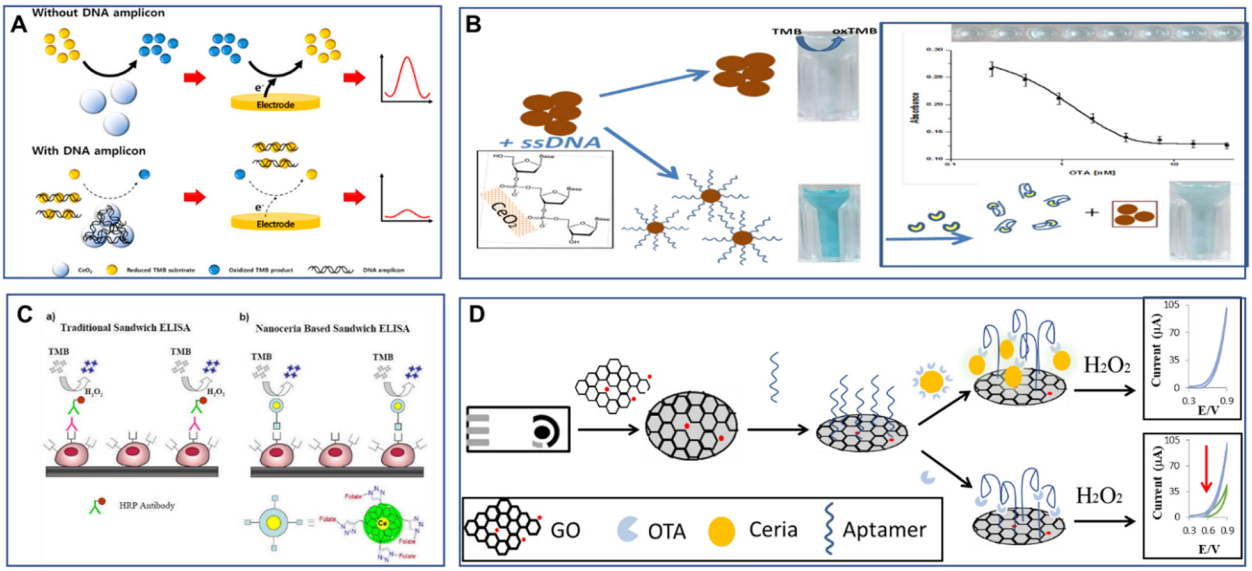


Fig. 29 Examples of bioaffinity interactions with CeNPs as an enzyme-mimetic nanocatalyst with electrochemical (A) and (D) and colorimetric (B) and (C) detection: (A) electrochemical detection of DNA amplicons by quantifying the catalytic activity of CeNPs using TMB (reprinted with permission from ref. 438), (B) colorimetric detection of target binding to DNA-aptamer-modified CeNPs with the detection of target-induced conformational changes and aggregation (with permission from ref. 440), (C) comparison between traditional immunoassay (ELISA, a) and CeNPs-based sandwich assay with CeNP labels mimicking the activity of oxidase enzyme. (Reprinted with permission from ref. 441), and (D) electrochemical sensor using CeNP tag and graphene oxide for the detection of aptamer targets through the measurement of the CeNP's-catalyzed $H_2O_2$ oxidation with and without target (reprinted from ref. 442 with permission from the Royal Society of Chemistry).

interaction between DNA with CeNPs, quantified using TMB. The adsorption of the amplicons on the CeNP surface blocks the CeNP's catalytic activity, thus decreasing the biosensor response proportionally to the concentration of the PCR products (Fig. 29B). The method enabled the determination of DNA amplicons derived from *E. coli* with an assay time of 6 min.[438] Recently, it was shown that such interactions can be conveniently monitored with a low cost personal glucose meter, making it amenable for point-of-care testing.[439] Detection was accomplished by monitoring CeNPs aggregation induced by DNA amplicons produced by PCR and quantifying the reduced ability to catalyze glucose oxidation in the presence of the target due to the electrostatic binding of the amplicons to the CeNPs. The assay time was 5 min and the target genomic DNA derived from *E. coli* was determined down to 10 copies, indicating the promise of this method for low-cost PCR amplification. In another work, a CeNPs-based aptasensing platform was reported using the ability of the CeNPs to interact electrostatically with ssDNA aptamers (Fig. 29A). Target binding was quantified by measuring changes in the CeNP's catalytic activity (*e.g.*, with TMB) before and upon target binding. Target binding was found to induce conformational changes of the aptamer at the CeNPs surface, changing the surface coverage and resulting in a decrease response proportionally with the increase in target concentration, measured by the reaction with TMB.[440] The method enabled the detection of ochratoxin A, a toxin produced by fungi, down to 0.15 nM.

Another interesting application is to use CeNPs as a replacement of the enzyme label in conventional affinity assays (*e.g.*, ELISA) in lieu of oxidase or peroxidase enzymes. One of the first reports suggesting that polymer (polyacrylic acid)-coated CeNPs can be used as an oxidase enzyme label in immunoassayas was published by Asati *et al.* in 2009, who demonstated that conjugation of CeNPs with targetting ligands can be used as a nanocatalyst with dual function as target binding and catalytic detector *via* the oxidation of the colorimetric dye TMB (Fig. 29C).[441] Enhanced detection for electrochemical aptasensors has been achieved by immobilizing the aptamer on a graphene-modified screen-printed electrode.[442] The target was captured by the immobilized aptamer and determined *via* a competitive mechanism between the free and the CeNPs labelled target by monitoring the $H_2O_2$ oxidation, amplified by the CeNP tag. Detection limits in the low nM range (0.1 nM), with a linearity range up to 180 nM, were obtained for the detection of a mycotoxin, ochratoxin A. Such strategies can be successfully implemented in point-of-care diagnostic devices.[443]

DNA-functionalized CeNPs can be used for a variety of biosensing applications such as to probe the oxidation of phosphorous compounds[444] and $H_2O_2$.[445] Modifications of the CNP surface can be made to enhance the oxidase-like activity and enable the detection of ions such as fluoride, quantified indirectly using ABTS dye.[404] Moreover, the CeNP's surface chemistry and surface ligand can be modulated to immobilize or displace DNA from the CeNPs' surface for the detection of substrates such as $H_2O_2$ and glucose in serum.[445] When CeNPs were coupled with glucose oxidase, a detection limit of 8.9 mM glucose was obtained. More recently, an integrated system of CeNPs/glucose oxidase was used to produce bio-nanoenzyme catalytic cascades with oxidase-like

 

activity.[446] Inhibition of the oxidase-like activity of CeNPs by ions such as arsenate and arsenite[447] or phosphate due to blocking of $Ce^{3+}$ sites[448] was also reported, opening up new avenues for the development of biomimetic CeNPs inhibition-based sensors. Such engineering designs of the CeNPs surface could increase the performance of CeNPs, making them powerful nanoenzymes for many practical applications.

More recently, hybrid materials and supramolecular structures such as Ce-based MOFs, traditionally known for their electrolytic performances,[449,450] have begun to be explored in biosensing. A bimetallic Ce/Cu-MOF ($CeO_2/CuO_x$@mC) aptamer nanocomposite was prepared for the detection of trace tobramycin (TOB) in human serum and milk.[451] Similarly, a nanohybrid of covalent organic framework (COF) and Ce-based (Ce-MOF@COF) nanostructure showed high binding affinity toward the oxytetracycline (OTC)-targeted aptamer.[452] The aptasensor displayed good reproducibility, selectivity, stability, and acceptable applicability for detecting OTC in various samples, including milk, wastewater, and urine. The future development of Ce-based mesoporous materials such as Ce-MOFs, which possess high porosity, could lead to the development of enhanced catalysts for next-generation sensing.

### 4.4. Environmental remediation

The presence of contaminants, such as metals, organic dyes, pesticides, nutrients and toxins, is a worldwide concern due to their long-term environmental effects.[396] Because of their thermal stability, optical properties, and oxygen transport capacity, CeNP-based materials can be used as sorbents in environmental remediation for water and wastewater treatment.[453–455] CeNPs can be used alone, in binary mixtures or deposited on various supports such as activated carbon, graphene, polymeric nanofibers, or mesoporous structures (Fig. 30). Their removal properties are attributed to the high surface charge density,[456] hydroxilated surface and rich surface defects that facilitate the rapid complexation of oxyanions such as phosphates and arsenates.[5,457] To improve handling, CeNPs has been added to conventional adsorbents such as activated carbon or carbon cryogel,[458] patterned on surfaces, or used in conjunction with porous materials such as mesoporous silica,[459] hierarchical porous $CeO_2$–$ZrO_2$ nanospheres,[460] or MOFs.[300,457]

Ceria-coated activated carbon was synthesized in a single step and used in water purification, where it demonstrated high efficiency for the removal of As(III) and As(V).[461] Additionally, a nanocomposite prepared from graphene nanosheets and CeNPs (G/$CeO_2$) was used for the extraction of Se(IV), As(V), As(III), Cu(II) and Pb(II) from water.[462] The maximum adsorption capacity of G/$CeO_2$ was extrapolated from the Langmuir model and found to be 8.4 for As(V), 14.1 for Se(IV), 50.0 for Cu(II) and 75.6 for Pb(II) (expressed in mg $g^{-1}$). These also showed good selectivity towards Se(IV) in the presence of Se(VI). CeNP-based materials were also used for ultratrace metal ions detection and speciation *via* electrochemistry.[271] Enhaced arsenic removal was achieved using porous $CeO_2$–$ZrO_2$ hollow nanospheres due to the high sorption capacity and selectivity for As; adsorption capacities of 110.7 and 145.3 mg $g^{-1}$ were reported for $As^{3+}$ and $As^{5+}$, respectively.[460] As a dual $Ce^{3+}/Ce^{4+}$ oxidation state

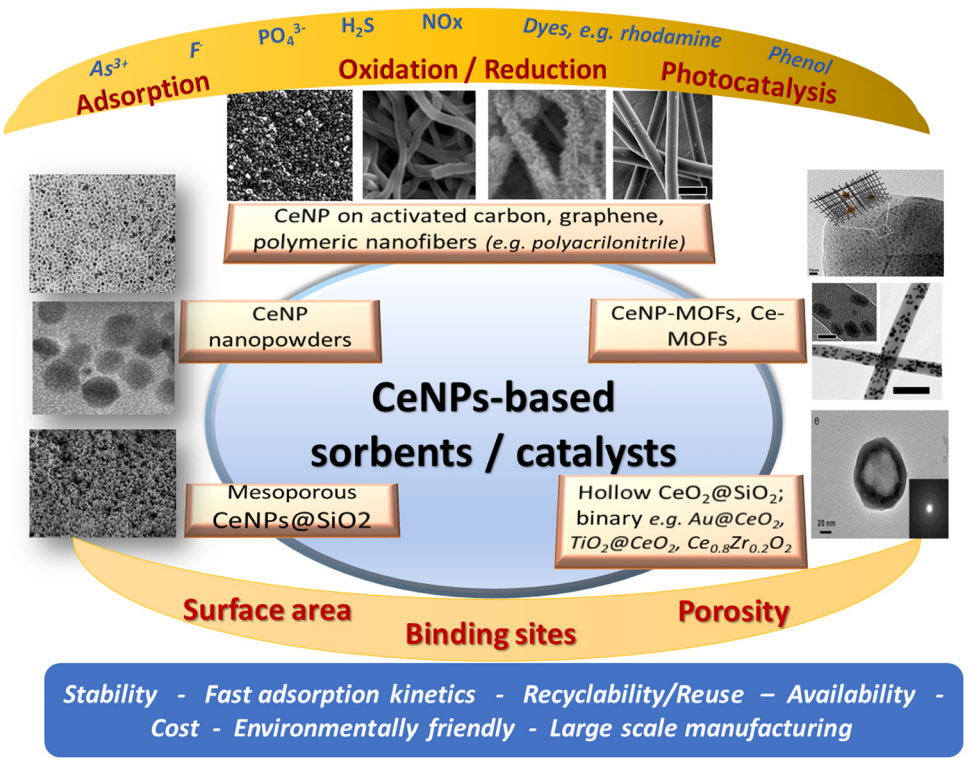


Fig. 30 Summary of CeNPs-based materials for environmental remediation.

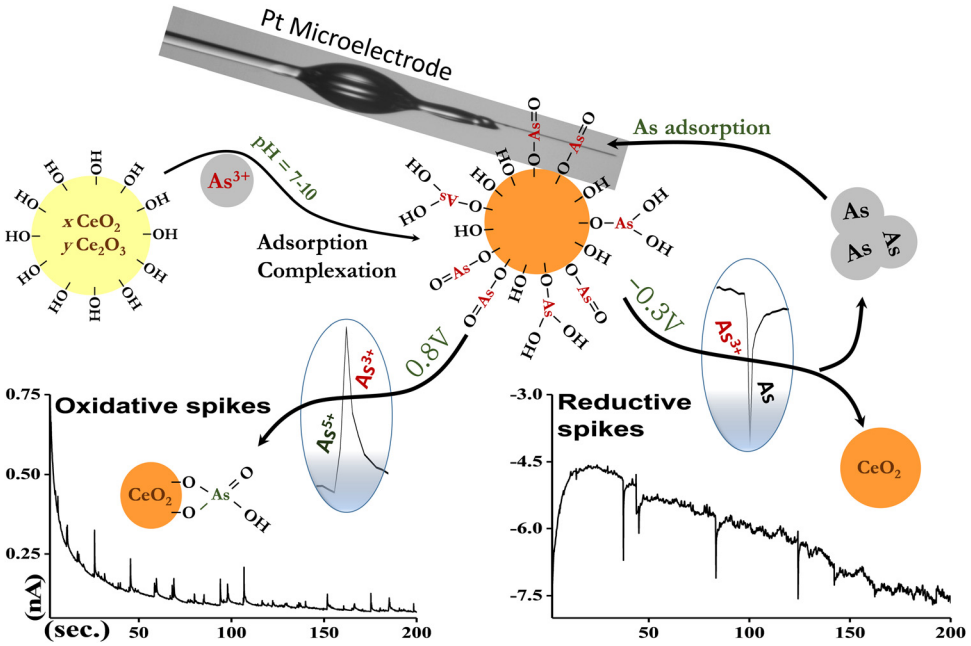


Fig. 31 Mechanism of $As^{3+}$ adsorption on CeNPs quantified by nanoscale electrochemistry by measuring current transients measured in reductive (−0.3 V) and oxidative (0.8 V *vs.* Ag/AgCl) conditions in PB at pH 8. Reproduced with permission from ref. 463. Copyright © 2019, American Chemical Society.

material, CeNPs can participate in electron exchange reactions with the $As^{3+}$ ions present in the solution. The mechanism of As adsorption and redox processes occurring between the surface $Ce^{3+}/Ce^{4+}$ and $As^{3+}$ at different pH conditions was demonstarted at single particle levels using nanoscale electrochemistry by monitoring the oxidation of $As^{3+}$ to $As^{5+}$ at 0.8 V *vs.* Ag/AgCl or the reduction of $As^{3+}$ to $As^{0}$ at −0.3 V (*vs.* Ag/AgCl).[463] The highest sorption capacity was observed at pH 8. In acidic environments (pH < 4), a small fraction of $As^{3+}$ was oxidized to $As^{5+}$ by surface $Ce^{4+}$ and further adsorbed onto the $CeO_2$ surface as an $As^{5+}$ bidentate complex (Fig. 31). Adsorption was common in basic conditions, confirming the strong adsorption of $As^{3+}$ onto CeNPs. These findings pave the way for rationally selecting the optimal material structure and conditions to increase the sorption capacity for environmental sensing and remediation applications.

CeNPs exhibit high selectivity for fluoride ($F^-$) adsorption and can be used as an adsorbent for $F^-$ removal from water. F is one of the essential elements in the human body for the formation of dental enamel and normal mineralization of bones.[464] However, the excessive intake of $F^-$ is harmful to the body and can lead to various health issues ranging from mild dental fluorosis to crippling skeletal fluorosis. While CeNPs are effective adsorbents and could be used in large scale column purification technologies for water defluoridation, their small size is impractical as it could cause column blockage, high pressure drop, and low flow rate. To overcome these limitations, binary oxides and hydroxides such as $CeO_2$–$ZrO_2$ nanocages[465] and Ce–La binary hydroxide[466] were explored as alternative sorbents with good $F^-$ uptake but slow adsorption rate. Further improvements were achieved using CeNPs incorporated on active supports like silica and organic polymers, which provide a large specific surface, fast diffusion kinetics, low cost, high mechanical strength and low pressure drop in a packed adsorption column.[467–470] $F^-$ adsorption onto a cubical ceria nanoadsorbent has shown pH-responsive behavior during the adsorption process.[471] At lower solution pH, a release of $OH^-$ was observed during the adsorption of fluoride by inner-sphere complex formation. At higher solution pH, the pH was found to decrease due to the exchange of $Na^+$ added in the form of NaOH by outer-sphere complex formation with $H^+$ ions adsorbed electrostatically on the adsorbent surface.[471]

Other environmental applications of CeNPs are as catalysts to remove exhaust emission,[472] and volatile organic chemicals (VOCs) and degrade organic pollutants from the environment. For example, CeNPs have shown high performance towards the reduction of $NO_x$ and the catalytic oxidation of $NH_3$ from engine exhaust.[473] Owing to their oxygen storage/release and the $Ce^{4+}/Ce^{3+}$ redox cycle, $CeO_2$-based catalysts are excellent candidates for the selective catalytic reduction of nitrogen oxides ($NO_x$) and carbon monoxide (CO), which contribute to acid rain and photochemical smog. In a typical catalytic convertor, ceria acts as a buffer adsorbing and releasing oxygen species depending on the operating conditions and temperature. It was reported that the use of CeNPs (30 nm) as an additive to fuel resulted in reduced fuel consumption by 2.5%, as well as reduction in NOx emission by 15.7% and smoke opacity by 34.7% compared to the additive-free fuel.[474] Enhanced catalytic performance for selective $NO_x$ reduction by $NH_3$ was obtained with the CeNP-based catalyst on oxide supports such as $Al_2O_2$, $TiO_2$ and $WO_3$ with the highest activation ability for Ce–O–W through rich Brønsted acid sites, redox ability and strong electronic $CeO_2$–support interactions.[475] NPs of $CeO_2$, $CuO/CeO_2$ and $Pt\text{-}MnO_2/CeO_2$ have shown high activity

 

for the oxidation of phenol intermediates.[476–478] Nanocomposites of $TiO_2/CeO_2$ on carbon nanotubes have demonstrated photo-oxidation capabilities for the degradation of organic content in agricultural wastewaters.[479] $Pd/CeO_2$ with carefully designed morphology and optimized shapes were effective catalysts for methanol decomposition to syngas with excellent activity at low temperatures.[480] Mn-doped CeNPs prepared by hydrothermal synthesis have shown a drastic increase in their capacity to adsorb oxygen due to the intercalation of $Mn^{3+}$ and the decrease in the $Ce^{3+}/(Ce^{3+} + Ce^{4+})$ content in the doped samples by replacement with $Mn^{3+}$. The doped samples had a significantly higher activity for toluene oxidation.[481]

CeNPs have also been studied for the photocatalytic degradation of reactive dyes, at which more than 95% of the dyes were destroyed under solar irradiation.[482] Recent work showed the ability of CeNPs to effectively degrade organic dyes such as fluorescein, rhodamine B, brilliant blue and Coomassie blue, with enhanced degradability in the presence of fluoride at ambient temperature.[483] The enhanced degradability in the presence of fluoride was attributed to the increased oxygen vacancy and the strong acidic environment. Hybrid CeNPs-lanthanide oxides demonstrated $H_2S$ adsorption and dissociation with subsequent oxygen vacancy regeneration, enabling their use for the desulfurization of biomass effluents.[484] It was demonstrated that adding Ce to metal oxide catalysts enhanced the catalytic activity and $SO_2$ resistance of Mn/Ti catalysts for the NO reduction with $NH_3$ by inhibiting the accumulation of ammoniom sulfates and preventing sulfidation.[485] The addition of a small amount of Ce (Ce/Ti = 0.05) was shown to improve the oxygen storage/release of $MnO_x$–$CeO_2/TiO_2$, thus enhancing the activity. Binary nanofibrous structures based on anisotropic Au/CeNPs embedded in poly(vinyl alcohol) (PVA) have shown potential as photocatalytic materials, promoting both oxidation and reduction of model waste products for environmental remediation processes such as the catalytic reduction of 4-nitrophenol to 4-aminophenol and of phenol red to bromophenol as well as the degradation rhodamine B in a flow-through reactor (Fig. 32).[486]

In other environmental applications, CeNPs have shown tremendous potential as sorbents for the removal of phosphorus to prevent water eutrophication. Eutrophication has become a global environmental problem due to the unnatural enrichment of water bodies with phosphorus (P) and nitrogen (N), which leads to the excessive growth of harmful algae blooms and depletion of dissolved oxygen levels, creating dead zones.269,457 Thus, removing the excess P and N is essential for preventing the negative consequences of eutrophication.[269,487] $CeO_2$-coated nanofibers have shown high adsorption capacity for the removal of P from aqueous solutions[488] with an adsorption capacity of 17 and 12 mmol $g^{-1}$ at low pH (2–6) and neutral pH. The removal process involved the formation of $CePO_4$ on the nanofiber surface. In other works, a recyclable adsorbent based on CeNPs grafted on mesoporous silica beads ($CeO_2$–$SiO_2$) has shown reversible adsorption behavior for P, demonstrating potential for both the removal and recovery of this important nutrient from

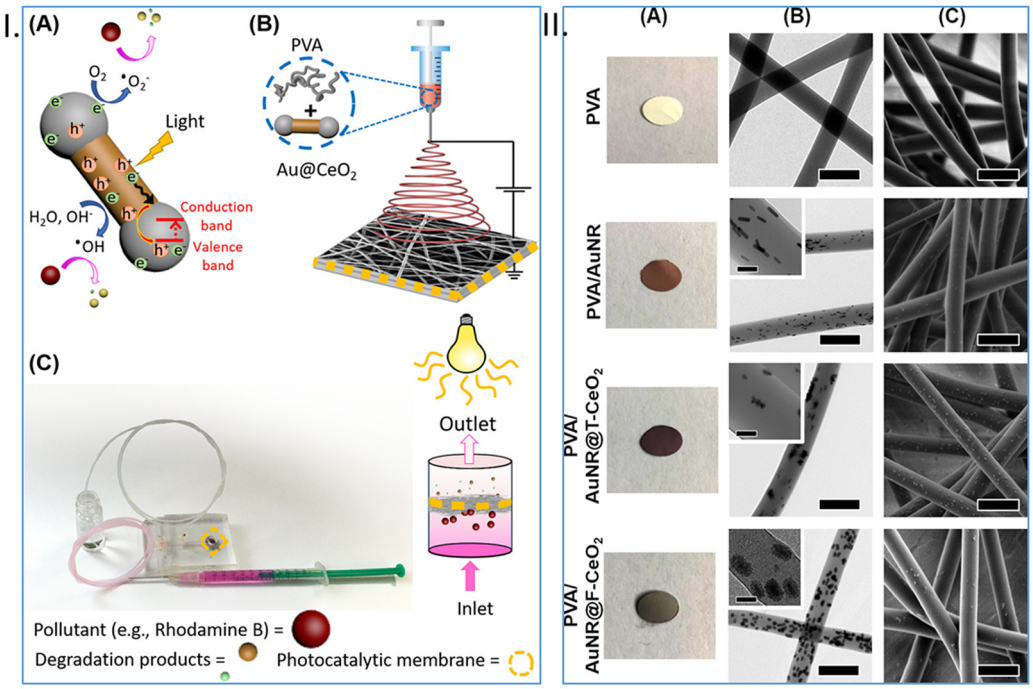


Fig. 32 (I) Photocatalytic membranes prepared by the colloidal electrospinning of a suspension of poly(vinyl alcohol) (PVA) and Au–CeNPs for use in a flow-through fluidic reactor showing (A) photocatalytic process, (B) Preparation of $Au@CeO_2$/PVA nanofibers by electrospinning, and (C) photocatalysis with the flow-through reactor containing the nanofibrous membrane; and (II) images (A), TEM (B) and SEM (C) of electrospun hybrid membranes made with PVA, PVA/AuNR, PVA/T-AuNR@$CeO_2$, and PVA/F-AuNR@$CeO_2$. Reprinted with permission from ref. 486. Copyright 2019 American Chemical Society.

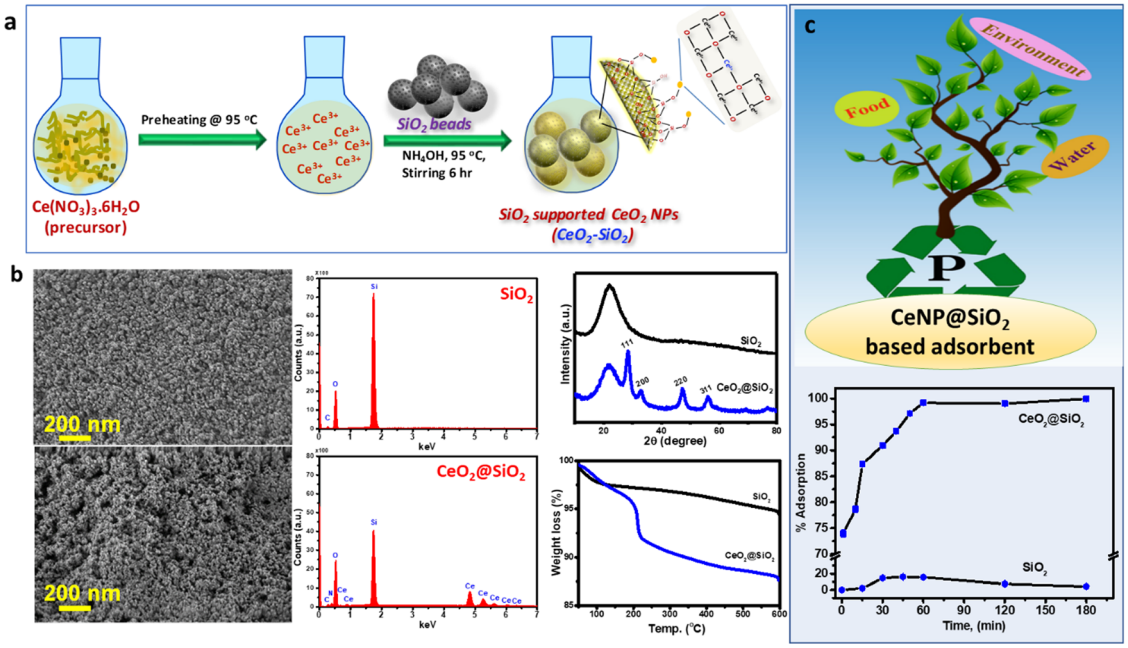


Fig. 33 Synthesis of $CeO_2$@$SiO_2$ adsorbent (a) with SEM, XRD and TGA characterization (b) and adsorption isotherms for the removal of phosphate (c) showing the significantly enhanced adsorption capacity of $CeO_2$@$SiO_2$ as compared to $SiO_2$ (reprinted with permission from ref. 459. Copyright 2019 American Chemical Society).

eutrophic waters (Fig. 33).[459] The adsorption mechanism involved the binding of $PO_4^{3-}$ through ion exchange and Lewis-acid based interactions, which provided a sorption/desorption capacity of 110 mg $g^{-1}$ with 99% removal within 60 min, significantly higher as compared to other sorbents. In the follow-up work with this system, ultrafast removal was achieved using a Ce(IV)-based MOF, Ce(IV) UiO-ss, and Xe 1,4-benzenedicarboxylate (Ce-BDC), which provided high surface area due to the open pores and high binding affinity of its open metal sites for phosphate. A removal capacity of 179 mg $g^{-1}$ within 4 min and in a broad range of pH (2–12) was reported.[457] Other enhancements have been obtained using binary oxides with properly designed ratios,489,490 optimized to enhance surface defects and facilitate complexation, thus increasing the adsorption capacity as compared to the single bare oxide. Su *et al.* developed a solvothermal process to synthesize a series of Ce/Zr binary oxide nanoadsorbents. A sorption capacity of 112.2 mg $g^{-1}$ was reported with an optimized oxides ratio of $Ce_{0.8}Zr_{0.2}O_2$.[491] In order to facilitate the recovery of the adorbents after the treatment, core–shell CeNPs ($Fe_3O_4$@$SiO_2$–$CeO_2$)[492] and ($Fe_3O_4$@-$SiO_2$@*m*$CeO_2$)[493] were designed to magnetically separate and remove these sorbents from the water environment. These structures can be utilized in a variety of applications such as membranes for phosphate separation and purification, sorbents for solid phase extraction or as P-selective materials for environmental sensing. Recently, it was shown that the use of Ce-metal nodes in the UiO-66-$NH_2$ MOF structure enables the fluorimetric sensing of phosphate, with a detection limit of 4.5 μM in a single-step measurement procedure.[494]

While the properties of CeNPs are vastly explored, their potential environmental and toxicological effects are still under investigation. The release of CeNPs into the environment is expected to increase as they start to be implemented in real-world applications.[493,495] Their use as polishers in the semiconducting industry[496] and as diesel fuel additives for catalytic convertors to control auto exhaust emission[497] are just two examples that can the result in the release and accumulation of CeNPs in the environment. The toxicology studied suggest that CeNPs by themselves are not particularly toxic; however, they can become toxic by the adsorption of toxic ions (*e.g.*, $As^{3+}$) or organics on their surface.[463] Therefore, understanding the fate, transport, and toxicity of these NPs exposed to contaminants is becoming increasingly important and will be critical in further studies to examine their environmental and health impacts.[5,498] The green synthesis of CeNPs can provide alternative routes to prepare CeNP-based materials without the need of using environmentally harmful reagents. For example, CeNPs were synthesized using plant-mediated synthesis wherein different plants such as *Gloriosa superba*, *Acalypha indica* and *Aloe vera* were used.[499–501] Additionally, honey, egg white and fungus-mediated synthesis were also used.[502–504] These plant extracts and natural components act as capping and reducing agents to produce nanocrystalline CeNPs in different sizes and morphology. These methods also offer advantages such as the low cost, large-scale production, and more importantly, their environment-friendly nature, making them interesting candidates for use in biomedicine and pharmaceutical applications. A detailed review on the green synthesis of CeNPs and their biological applications has been published.[505]

### 4.5. Biomedical applications

The ability of CeNPs to catalyze the detoxification of free radicals and act as artificial antioxidants provides a broad

 

range of opportunities for using this system in biomedicine, particularly for treating disease conditions in which excess free radical formation is thought to play a role.[506] These range from relatively rare diseases, such as Amyotrophic Lateral Sclerosis (ALS), to more common conditions, such as stroke, cancer,[507] traumatic brain injury, Parkinson's and Alzheimer's disease to the ubiquitous normal processes of aging. CeNPs possess a number of advantages over other antioxidants. CeNPs have been shown to provide antioxidant, immunomodulatory, antimicrobial and antiviral, and anticancer properties, and their ability to be used as theranostic probes.[8] When administered systemically, CeNPs appear to cross the blood brain barrier.[508]

Their properties can be enhanced by modification with other drugs, as demonstrated with edaravone attached using poly(ethylene glycol); the combined effect provided enhanced neuroprotective action for stroke treatment through the inactivation of ROS and enhanced accessibility to cross the blood–brain barrier.[509] The regenerative behavior of the CeNPs, enabling them to regain the antioxidant activity upon interaction with ROS, provide additional opportunities for these particles to remain active for long periods of time and be used in tissue engineering to support neural survival and growth.[510] Thus, they could be administered preventatively or early in a chronic disease process. Other applications include utilization in spinal cord repair as neuroprotective agents,[511,512] support cell survival,[513,514] and scavenging ROS in the eyes to prevent degenerative retinal disorders.[513] When cells were exposed to $H_2O_2$, CeNPs reduced oxidative damage by over 60%.[9,511,512]

CeNPs holds potential as a drug delivery platform for targeted therapy. For example, they can be conjugated with other therapeutically-effective molecules to improve drug delivery[515] or modified with specific receptors and biomolecules for targeted delivery[516] and wound healing.[517] The tunable surface and large surface-to-volume ratio facilitate enhanced loading and potential for release, making them a versatile platform for personalized medicine.[518] They can also be incorporated in hydrogels or other biomaterial matrices and used to support cell adhesion and proliferation, and promote wound healing.[519] The tunable catalytic activity of the CeNPs has been shown to be effective in preventing chemotherapy-induced acute kidney injury and restore redox homeosthasis.[520] Biomedical imaging is another area in which CeNPs can find exciting emerging applications such as contrast agents and imaging modalities for magnetic resonance imaging (MRI) and computed tomography. This can be achieved by the surface modification of the CeNPs with dyes or other imaging agents or by doping with Eu or Gd, enabling the visualization of biological processes and monitoring of therapeutic response, thus facilitating the early detection and monitoring of diseases.[521,522] While the biomedical applications of CeNPs are rapidly emerging, the rational design and better control of the structure, properties and dose response is still needed to establish conditions that can effectively reduce the level of free radicals without impairing the normal physiological functions. Several reviews expanding on the biomedical and theranostic applications of CeNPs can be found in the literature.[8,169,171,523]

# 5. Summary and outlook

The unique structure, tunable reactivity and rich surface chemistry make CeNP an extremely versatile material for a wide variety of applications. Herein, we have comprehensively reviewed the progress made in the development of CeNPs-based materials, their structure, properties and emerging applications over the past two decades. The synthesis and control of the surface properties represent key strategies for customizing the physicochemical characteristics of these materials to meet the requirements of diverse applications and advancing new products and innovations. Understanding the structural properties at the atomic levels provides the fundamental knowledge necessary to engineer structures with controlled reactivity and surface functions. Such studies are still needed to identify key parameters in the synthetic design that can be used to predict the reactivity and generate CeNP-based materials and devices with the desired properties for a given target. Further improvements in the synthesis, surface functionalization and the use of *in situ* characterization techniques will help achieve better control of the CeNPs properties (*e.g.*, antioxidant *vs.* prooxidant) and develop predictable structures with tailored reactivity and surface binding characteristics. Moving forward, we expect development in the following areas.

- First, fundamental work is still needed to identify the origin of CeNPs reactivity (surface defects, complexation, $Ce^{3+}$/$Ce^{4+}$ ratio, size, shape and surface ligand effects) and how these relate to the physicochemical properties and reactivity of the materials. Considerable progress is expected in modulating the surface chemistry and developing structure/function relations, some of which may require computational design for understanding the complex CeNPs chemistry and predicting activity and selectivity for a given target.
- Secondly, recent work has shown that combining two or more materials and creating hybrid and composite structures can significantly enhance the properties. Understanding the effect of interfacial structures and interactions between two or more types of materials (chemical bonds, surface energy, interface mechanics, *etc.*) is needed to more rationally design structures that take advantage of the synergistic effects and complementarity of their mixed components. Examples include noble metals (Pt, Au)-CeNPs, polymeric materials-CeNPs, metal oxides-CeNPs, in particular those with catalytic and magnetic properties ($TiO_2$, ZnO, $Fe_2O_3$), as well as bio-interfaces by conjugating CeNPs with enzymes, aptamers, DNA, antibodies, *etc.*, for obtaining improved catalytic and sensing functions.
- Third, as the applications of these materials continue to grow, the manufacturing and integration of CeNPs in devices, membranes and coatings will constitute an area of intensive research. The use of advanced manufacturing practices such as 2D and 3D printing are of great interest to produce low-cost high throughput structures. Moreover, integrating CeNPs into functional and practical devices will be needed to effectivelly translate these innovations into practice and consumer applications.
- Fourth, as more CeNPs are implemented into consumer products, understanding their environmental transformation,

fate, transport, toxicity and their transformed products will be needed, particularly in areas where there is a risk of exposure such as semiconducting manufaring plants, where large amounts of CeNPs-containing waste is generated, or in high trafic areas, where small CeNPs additives could be released from diesel engine emissions. Tailoring the surface to minimize potential harmful effects is also needed to prevent toxicity on the natural environment and humans. Given their reactivity, the use of CeNPs should be considered with a full understanding of their unique properties in order to reduce potential risks and ensure their safe utilization and implementation into the practice.

• Finally, we expect exciting developments in several areas, highlighting the versatility of these materials in addressing many societal challenges ranging from semiconducting industries to healthcare, environmental remediation and consumer products. Among these, new generations of CeNPs with controlled morphology and surface chemistry will be needed to be used as polishers in CMP to address the needs for smaller and greener semiconducting manufacturing processes. CeNP-based photocatalysts and sorbents will continue to attract interest for environmental remediation and energy conversion. Particularly, the tunable redox chemistry and electrochemical stability make them interesting candidates for electrode materials, electrolytes and catalysis, while the catalytic activity towards pollutants such as VOCs, NOx, metals and organics make them well suited for promoting detoxification and removing contaminants through redox and surface adsorption reactions. An array of products and applications are expected to emerge from the exploration of the antioxidant activity and ability to protect cells from oxidative damage, with impact in drug delivery, biomedical imaging, neuroprotection and the cosmetic industry as anti-aging and UV-protection agents in skin-care. Continued research and development will be needed to explore and optimize the performance of CeNPs in these diverse applications.

In summary, it is increasingly clear that CeNPs have huge potential, as demonstrated by an already increasing number of applications in many areas of science and technology and industries such as catalysis, sensing, semiconductor and environment. The review has tried to provide the most significant advancements to date in a systematic and comprehensive manner. Scientists and engineers can use this overview as a starting point to explore this material's unique and unusual properties and pursue new avenues into the future.

## Conflicts of interest

There are no conflicts to declare.

## Acknowledgements

This material is based upon work supported by the National Science Foundation under Grants 20425544, 1336493, 0954919, and the United States Department of Agriculture (USDA) under Grant 2023-67021-39750. Any opinions, findings, and conclusions or recommendations expressed in this material are those of the author(s) and do not necessarily reflect the views of the National Science Foundation, or the USDA. SA acknowledges all past and present members of Andreescu's group for their contribution to the study of various aspects of ceria chemistry.

## References

1 J. Paier, C. Penschke and J. Sauer, *Chem. Rev.*, 2013, **113**, 3949–3985.
2 R. Schmitt, A. Nenning, O. Kraynis, R. Korobko, A. I. Frenkel, I. Lubomirsky, S. M. Haile and J. L. M. Rupp, *Chem. Soc. Rev.*, 2020, **49**, 554–592.
3 T. Montini, M. Melchionna, M. Monai and P. Fornasiero, *Chem. Rev.*, 2016, **116**, 5987–6041.
4 E. Ozkan, P. Cop, F. Benfer, A. Hofmann, M. Votsmeier, J. M. Guerra, M. Giar, C. Heiliger, H. Over and B. M. Smarsly, *J. Phys. Chem. C*, 2020, **124**, 8736–8748.
5 D. Andreescu, G. Bulbul, R. E. Ozel, A. Hayat, N. Sardesai and S. Andreescu, *Environ. Sci.: Nano*, 2014, **1**, 445–458.
6 J. Zhou, R. T. Guo, X. F. Zhang, Y. Z. Liu, C. P. Duan, G. L. Wu and W. G. Pan, *Energy Fuel*, 2021, **35**, 2981–2998.
7 E. Grulke, K. Reed, M. Beck, X. Huang, A. Cormack and S. Seal, *Environ. Sci.: Nano*, 2014, **1**, 429–444.
8 S. Banavar, A. Deshpande, S. Sur and S. Andreescu, *JPhys Mater.*, 2021, **4**, 042003.
9 M. A. Saifi, S. Seal and C. Godugu, *J. Controlled Release*, 2021, **338**, 164–189.
10 A. Hayat, D. Andreescu, G. Bulbul and S. Andreescu, *J. Colloid Interface Sci.*, 2014, **418**, 240–245.
11 R. A. Yokel, S. Hussain, S. Garantziotis, P. Demokritou, V. Castranova and F. R. Cassee, *Environ. Sci.: Nano*, 2014, **1**, 406–428.
12 J. Ma, X. Tong, J. Wang, G. Zhang, Y. Lv, Y. Zhu, S. Sun, Y.-C. Yang and Y. Song, *Electrochim. Acta*, 2019, **229**, 80–88.
13 A. Trovarelli, *Catalysis by Ceria and Related Materials*, World Scientific Publishing Co Pte Ltd, 2002.
14 E. Mamontov and T. Egami, *J. Phys. Chem. Solids*, 2000, **61**, 1345–1356.
15 T. S. Sakthivel, D. L. Reid, U. M. Bhatta, G. Möbus, D. C. Sayle and S. Seal, *Nanoscale*, 2015, **7**, 5169–5177.
16 B. Choudhury and A. Choudhury, *Mater. Chem. Phys.*, 2012, **131**, 666–671.
17 S. Deshpande, S. Patil, S. V. Kuchibhatla and S. Seal, *Appl. Phys. Lett.*, 2005, **87**, 133113.
18 S. Tsunekawa, R. Sivamohan, S. Ito, A. Kasuya and T. Fukuda, *Nanostruct. Mater.*, 1999, **11**, 141–147.
19 S. Tsunekawa, R. Sahara, Y. Kawazoe and K. Ishikawa, *Appl. Surf. Sci.*, 1999, **152**, 53–56.
20 V. K. Paidi, L. Savereide, D. J. Childers, J. M. Notestein, C. A. Roberts and J. Van Lierop, *ACS Appl. Mater. Interfaces*, 2017, **9**, 30670–30678.
21 H.-Y. Li, H.-F. Wang, X.-Q. Gong, Y.-L. Guo, Y. Guo, G. Lu and P. Hu, *Phys. Rev. B: Condens. Matter Mater. Phys.*, 2009, **79**, 193401.
22 M. Nolan, *Chem. Phys. Lett.*, 2010, **499**, 126–130.

 

23 M. Nolan, S. Grigoleit, D. C. Sayle, S. C. Parker and G. W. Watson, *Surf. Sci.*, 2005, **576**, 217–229.
24 F. Esch, S. Fabris, L. Zhou, T. Montini, C. Africh, P. Fornasiero, G. Comelli and R. Rosei, *Science*, 2005, **309**, 752.
25 C. Zhang, A. Michaelides, D. A. King and S. J. Jenkins, *Phys. Rev. B: Condens. Matter Mater. Phys.*, 2009, **79**, 075433.
26 S. C. Shirbhate, A. K. Yadav and S. A. Acharya, *Appl. Phys. Lett.*, 2016, **108**, 143501.
27 Z. Yang, T. K. Woo, M. Baudin and K. Hermansson, *J. Chem. Phys.*, 2004, **120**, 7741–7749.
28 J. Kullgren, M. J. Wolf, C. Castleton, P. Mitev, W. J. Briels and K. Hermansson, *Phys. Rev. Lett.*, 2014, **112**, 156102.
29 S. Torbrügge, M. Reichling, A. Ishiyama, S. Morita and Ó. Custance, *Phys. Rev. Lett.*, 2007, **99**, 056101.
30 H. Nörenberg and G. A. D. Briggs, *Surf. Sci.*, 1999, **424**, L352–L355.
31 Y. Namai, K.-i Fukui and Y. Iwasawa, *J. Phys. Chem. B*, 2003, **107**, 11666–11673.
32 G.-y Adachi and N. Imanaka, *Chem. Rev.*, 1998, **98**, 1479–1514.
33 P. Knappe and L. Eyring, *J. Solid State Chem.*, 1985, **58**, 312–324.
34 M. Yashima, D. Ishimura, Y. Yamaguchi, K. Ohoyama and K. Kawachi, *Chem. Phys. Lett.*, 2003, **372**, 784–787.
35 M. Zinkevich, D. Djurovic and F. Aldinger, *Solid State Ionics*, 2006, **177**, 989–1001.
36 O. T. Sørensen, *J. Solid State Chem.*, 1976, **18**, 217–233.
37 E. Kümmerle and G. Heger, *J. Solid State Chem.*, 1999, **147**, 485–500.
38 S. Ray and D. Cox, *J. Solid State Chem.*, 1975, **15**, 333–343.
39 Y. Cao, L. Zhao, T. Gutmann, Y. Xu, L. Dong, G. Buntkowsky and F. Gao, *J. Phys. Chem. C*, 2018, **122**, 20402–20409.
40 A. Trovarelli and J. Llorca, *ACS Catal.*, 2017, **7**, 4716–4735.
41 W. Wei-Wei, Y. Wen-Zhu, D. Pei-Pei, X. Hui, J. Zhao, S. Rui, M. Chao, S. Shuo, J. Chun-Jiang and Y. Chun-Hua, *Crystal Plane Effect of Ceria on Supported Copper Oxide Cluster Catalyst for CO Oxidation: Importance of Metal–Support Interaction*, 2017.
42 J. Conesa, *Surf. Sci.*, 1995, **339**, 337–352.
43 M. M. Branda, R. M. Ferullo, M. Causa and F. Illas, *J. Phys. Chem. C*, 2011, **115**, 3716–3721.
44 M. V. Ganduglia-Pirovano, A. Hofmann and J. Sauer, *Surf. Sci. Rep.*, 2007, **62**, 219–270.
45 D. R. Mullins, *Surf. Sci. Rep.*, 2015, **70**, 42–85.
46 D. R. Mullins, P. M. Albrecht and F. Calaza, *Top. Catal.*, 2013, **56**, 1345–1362.
47 M. Nolan, S. C. Parker and G. W. Watson, *Surf. Sci.*, 2005, **595**, 223–232.
48 M. V. Ganduglia-Pirovano, J. L. F. Da Silva and J. Sauer, *Phys. Rev. Lett.*, 2009, **102**, 026101.
49 D. Zhang, X. Du, L. Shi and R. Gao, *Dalton Trans.*, 2012, **41**, 14455–14475.
50 Q. Wu, F. Zhang, P. Xiao, H. Tao, X. Wang, Z. Hu and Y. Lü, *J. Phys. Chem. C*, 2008, **112**, 17076–17080.
51 X. Liu, K. Zhou, L. Wang, B. Wang and Y. Li, *J. Am. Chem. Soc.*, 2009, **131**, 3140–3141.
52 C. Pan, D. Zhang and L. Shi, *J. Solid State Chem.*, 2008, **181**, 1298–1306.
53 S. Yang and L. Gao, *J. Am. Chem. Soc.*, 2006, **128**, 9330–9331.
54 H.-I. Chen and H.-Y. Chang, *Solid State Commun.*, 2005, **133**, 593–598.
55 N. Du, H. Zhang, B. Chen, X. Ma and D. Yang, *J. Phys. Chem. C*, 2007, **111**, 12677–12680.
56 J.-G. Li, T. Ikegami, Y. Wang and T. Mori, *J. Am. Ceram. Soc.*, 2002, **85**, 2376–2378.
57 H.-Y. Chang and H.-I. Chen, *J. Cryst. Growth*, 2005, **283**, 457–468.
58 M. Cabus-Llaurado, Y. Cesteros, F. Medina, P. Salagre and J. Sueiras, *Microporous Mesoporous Mater.*, 2007, **100**, 167–172.
59 H. Y. Ma, H. J. Ren, P. Koshy, C. C. Sorrell and J. N. Hart, *J. Phys. Chem. C*, 2020, **124**, 2644–2655.
60 B. Tang, L. Zhuo, J. Ge, G. Wang, Z. Shi and J. Niu, *Chem. Commun.*, 2005, 3565–3567.
61 Z. Yang, J. Wei, H. Yang, L. Liu, H. Liang and Y. Yang, *Eur. J. Inorg. Chem.*, 2010, 3354–3359.
62 W.-Q. Han, L. Wu and Y. Zhu, *J. Am. Chem. Soc.*, 2005, **127**, 12814–12815.
63 H.-X. Mai, L.-D. Sun, Y.-W. Zhang, R. Si, W. Feng, H.-P. Zhang, H.-C. Liu and C.-H. Yan, *J. Phys. Chem. B*, 2005, **109**, 24380–24385.
64 G. Li, K. Chao, H. Peng, K. Chen and Z. Zhang, *J. Phys. Chem. C*, 2008, **112**, 16452–16456.
65 Z.-R. Tang, Y. Zhang and Y.-J. Xu, *RSC Adv.*, 2011, **1**, 1772–1777.
66 Z. Guo, F. Du, G. Li and Z. Cui, *Inorg. Chem.*, 2006, **45**, 4167–4169.
67 Y. Zhang, F. Hou and Y. Tan, *Chem. Commun.*, 2012, **48**, 2391–2393.
68 K. W. Kolasinski, *Curr. Opin. Solid State Mater. Sci.*, 2006, **10**, 182–191.
69 D. Wang, Y. Kang, V. Doan-Nguyen, J. Chen, R. Küngas, N. L. Wieder, K. Bakhmutsky, R. J. Gorte and C. B. Murray, *Angew. Chem., Int. Ed.*, 2011, **50**, 4378–4381.
70 X. Wang, J. Zhuang, Q. Peng and Y. Li, *Adv. Mater.*, 2006, **18**, 2031–2034.
71 T. Yu, J. Joo, Y. I. Park and T. Hyeon, *Angew. Chem., Int. Ed.*, 2005, **44**, 7411–7414.
72 D. Zhang, F. Niu, H. Li, L. Shi and J. Fang, *Powder Technol.*, 2011, **207**, 35–41.
73 C. Sun, H. Li and L. Chen, *Energy Environ. Sci.*, 2012, **5**, 8475–8505.
74 Q. Yuan, H.-H. Duan, L.-L. Li, L.-D. Sun, Y.-W. Zhang and C.-H. Yan, *J. Colloid Interface Sci.*, 2009, **335**, 151–167.
75 K. Wu, L. D. Sun and C. H. Yan, *Adv. Energy Mater.*, 2016, **6**, 1600501.
76 I. Florea, C. D. Feral-Martin, J. R. Majimel, D. Ihiawakrim, C. Hirlimann and O. Ersen, *Cryst. Growth Des.*, 2013, **13**, 1110–1121.

77 M. Nolan, *J. Mater. Chem.*, 2011, **21**, 9160–9168.
78 M. Nolan, V. S. Verdugo and H. Metiu, *Surf. Sci.*, 2008, **602**, 2734–2742.
79 L. Wu, H. J. Wiesmann, A. R. Moodenbaugh, R. F. Klie, Y. Zhu, D. O. Welch and M. Suenaga, *Phys. Rev. B: Condens. Matter Mater. Phys.*, 2004, **69**, 125415.
80 R. K. Hailstone, A. G. DiFrancesco, J. G. Leong, T. D. Allston and K. J. Reed, *J. Phys. Chem. C*, 2009, **113**, 15155–15159.
81 J. Xu, J. Harmer, G. Li, T. Chapman, P. Collier, S. Longworth and S. C. Tsang, *Chem. Commun.*, 2010, **46**, 1887–1889.
82 M. K. Ghosalya, X. S. Li, A. Beck, J. A. Van Bokhoven and L. Artiglia, *J. Phys. Chem. C*, 2021, **125**, 9303–9309.
83 C. Paun, O. V. Safonova, J. Szlachetko, P. M. Abdala, M. Nachtegaal, J. Sa, E. Kleymenov, A. Cervellino, F. Krumeich and J. A. van Bokhoven, *J. Phys. Chem. C*, 2012, **116**, 7312–7317.
84 X.-D. Zhou and W. Huebner, *Appl. Phys. Lett.*, 2001, **79**, 3512–3514.
85 F. Zhang, S.-W. Chan, J. E. Spanier, E. Apak, Q. Jin, R. D. Robinson and I. P. Herman, *Appl. Phys. Lett.*, 2002, **80**, 127–129.
86 J. Seo, A. Gowda and S. Babu, *ECS J. Solid State Sci. Technol.*, 2018, **7**, P243–P252.
87 J. Seo, J. Moon, J. H. Kim, K. Lee, J. Hwang, H. Yoon, D. K. Yi and U. Paik, *Appl. Surf. Sci.*, 2016, **389**, 311–315.
88 K. M. Kumar, M. Mahendhiran, M. C. Diaz, N. Hernandez-Como, A. Hernandez-Eligio, G. Torres-Torres, S. Godavarthi and L. M. Gomez, *Mater. Lett.*, 2018, **214**, 15–19.
89 B. Choudhury, P. Chetri and A. Choudhury, *J. Exp. Nanosci.*, 2015, **10**, 103–114.
90 G. N. Vayssilov, Y. Lykhach, A. Migani, T. Staudt, G. P. Petrova, N. Tsud, T. Skála, A. Bruix, F. Illas, K. C. Prince, V. R. Matolın, K. M. Neyman and J. Libuda, *Nat. Mater.*, 2011, **10**, 310.
91 P. Nachimuthu, W.-C. Shih, R.-S. Liu, L.-Y. Jang and J.-M. Chen, *J. Solid State Chem.*, 2000, **149**, 408–413.
92 A. Migani, G. N. Vayssilov, S. T. Bromley, F. Illas and K. M. Neyman, *J. Mater. Chem.*, 2010, **20**, 10535–10546.
93 A. Bruix and K. M. Neyman, *Catal. Lett.*, 2016, **146**, 2053–2080.
94 M. A. Sk, S. M. Kozlov, K. H. Lim, A. Migani and K. M. Neyman, *J. Mater. Chem. A*, 2014, **2**, 18329–18338.
95 A. Ruiz Puigdollers, P. Schlexer, S. Tosoni and G. Pacchioni, *ACS Catal.*, 2017, **7**, 6493–6513.
96 M. Boaro, S. Colussi and A. Trovarelli, *Front. Chem.*, 2019, **7**, 28.
97 H. J. Kim, M. G. Jang, D. Shin and J. W. Han, *ChemCatChem*, 2020, **12**, 11–26.
98 L. Mei, L. Zhaogang, H. Yanhong, W. Mitang and L. Hangquan, *J. Rare Earths*, 2008, **26**, 357–361.
99 C. Gunawan, M. S. Lord, E. Lovell, R. J. Wong, M. S. Jung, D. Oscar, R. Mann and R. Amal, *ACS Omega*, 2019, **4**, 9473–9479.
100 D. A. Andersson, S. I. Simak, N. V. Skorodumova, I. A. Abrikosov and B. Johansson, *Proc. Natl. Acad. Sci. U. S. A.*, 2006, **103**, 3518–3521.
101 M. Coduri, S. Checchia, M. Longhi, D. Ceresoli and M. Scavini, *Front. Chem.*, 2018, **6**, 526.
102 T. Vinodkumar, B. G. Rao and B. M. Reddy, *Catal. Today*, 2015, **253**, 57–64.
103 D. Mukherjee and B. M. Reddy, *Catal. Today*, 2018, **309**, 227–235.
104 C. Veranitisagul, N. Koonsaeng, N. Laosiripojana and A. Laobuthee, *J. Ind. Eng. Chem.*, 2012, **18**, 898–903.
105 U. Hennings and R. Reimert, *Appl. Catal., A*, 2007, **325**, 41–49.
106 D. N. Durgasri, T. Vinodkumar, P. Sudarsanam and B. M. Reddy, *Catal. Lett.*, 2014, **144**, 971–979.
107 K. Krishna, A. Bueno-López, M. Makkee and J. Moulijn, *Appl. Catal., B*, 2007, **75**, 189–200.
108 A. Bueno-López, *Appl. Catal., B*, 2014, **146**, 1–11.
109 S. Patil, S. Seal, Y. Guo, A. Schulte and J. Norwood, *Appl. Phys. Lett.*, 2006, **88**, 243110.
110 S. Babu, R. Thanneeru, T. Inerbaev, R. Day, A. E. Masunov, A. Schulte and S. Seal, *Nanotechnology*, 2009, **20**, 085713.
111 N. Shehata, K. Meehan, M. Hudait, N. Jain and S. Gaballah, *J. Nanomater.*, 2014, **2014**, 156.
112 K. Kim, J. D. Yoo, S. Lee, M. Bae, J. Bae, W. Jung and J. W. Han, *ACS Appl. Mater. Interfaces*, 2017, **9**, 15449–15458.
113 I. Hemmilä, V.-M. Mukkala and H. Takalo, *J. Alloys Compd.*, 1997, **249**, 158–162.
114 Q. Ma, J. Wang, Z. Li, X. Lv, L. Liang and Q. Yuan, *Small*, 2019, **15**, 1804969.
115 J. Wu, G. Wang, D. Jin, J. Yuan, Y. Guan and J. Piper, *Chem. Commun.*, 2008, 365–367.
116 L. Li, H. K. Yang, B. K. Moon, Z. Fu, C. Guo, J. H. Jeong, S. S. Yi, K. Jang and H. S. Lee, *J. Phys. Chem. C*, 2009, **113**, 610–617.
117 A. Kumar, S. Babu, A. S. Karakoti, A. Schulte and S. Seal, *Langmuir*, 2009, **25**, 10998–11007.
118 K. Woan, Y.-Y. Tsai and W. Sigmund, *Nanomedicine*, 2010, **5**, 233–242.
119 I. Celardo, M. De Nicola, C. Mandoli, J. Z. Pedersen, E. Traversa and L. Ghibelli, *ACS Nano*, 2011, **5**, 4537–4549.
120 N. Yang, P. Orgian, E. D. Bartolomeo, V. Foglietti, O. Piero Torelli, E. V. Levlev, G. Rossi, S. Licoccia, G. Balestrino, S. V. Kalinin and C. Aruta, *J. Phys. Chem. C*, 2017, **121**, 8841–8849.
121 N. Novik, V. Konakov and I. Y. Archakov, *Rev. Adv. Mater. Sci.*, 2015, 40.
122 S. Damyanova, B. Pawelec, K. Arishtirova, M. V. M. Huerta and J. L. G. Fierro, *Appl. Catal., A*, 2008, **337**, 86–96.
123 T. Masui, T. Ozaki, K.-I. Machida and G.-Y. Adachi, *J. Alloys Compd.*, 2000, **303–304**, 49–55.
124 D. Devaiah, L. H. Reddy, S.-E. Park and B. M. Reddy, *Catal. Rev.*, 2018, **60**, 177–277.
125 E. Aneggi, M. Boaro, S. Colussi, C. de Leitenburg and A. Trovarelli, in *Handbook on the Physics and Chemistry of Rare Earths*, ed. J.-C. G. Bünzli and V. K. Pecharsky, Elsevier, 2016, vol. 50, pp. 209–242.
126 N. Guillén-Hurtado, I. Atribak, A. Bueno-López and A. García-García, *J. Mol. Catal. A: Chem.*, 2010, **323**, 52–58.

 

127 C. Hu, Q. Zhu, Z. Jiang, L. Chen and R. Wu, *Chem. Eng. J.*, 2009, **152**, 583–590.
128 C. Hu, *Chem. Eng. J.*, 2011, **168**, 1185–1192.
129 R. Qin, J. Chen, X. Gao, X. Zhu, X. Yu and K. Cen, *RSC Adv.*, 2014, **4**, 43874–43881.
130 P. Venkataswamy, D. Mukherjee, D. Devaiah, M. Vithal and B. M. Reddy, *Curr. Nanomater.*, 2018, **3**, 103–113.
131 S. Ramana, B. G. Rao, P. Venkataswamy, A. Rangaswamy and B. M. Reddy, *J. Mol. Catal. A: Chem.*, 2016, **415**, 113–121.
132 W. Derafa, F. Paloukis, B. Mewafy, W. Baaziz, O. Ersen, C. Petit, G. Corbel and S. Zafeiratos, *RSC Adv.*, 2018, **8**, 40712–40719.
133 A. J. M. Araújo, V. D. Silva, A. R. O. Sousa, J. P. F. Grilo, T. A. Simões, D. A. Macedo, R. M. Nascimento and C. A. Paskocimas, *Ceram. Int.*, 2019, **45**, 7157–7165.
134 A. Jha, D.-W. Jeong, Y.-L. Lee, I. W. Nah and H.-S. Roh, *RSC Adv.*, 2015, **5**, 103023–103029.
135 A. A. Ansari, J. Labis, M. Alam, S. M. Ramay, N. Ahmad and A. Mahmood, *Phase Trans.*, 2016, **89**, 261–272.
136 Y. Wang, F. Wang, Y. Chen, D. Zhang, B. Li, S. Kang, X. Li and L. Cui, *Appl. Catal., B*, 2014, **147**, 602–609.
137 M. O. Mazan, J. Marrero-Jerez, A. Soldati, P. Núñez and S. A. Larrondo, *Int. J. Hydrogen Energy*, 2015, **40**, 3981–3989.
138 J. Wang, B. Zhang, M. Shen, J. Wang, W. Wang, J. Ma, S. Liu and L. Jia, *J. Sol-Gel Sci. Technol.*, 2011, **58**, 259–268.
139 L. Kundakovic and M. Flytzani-Stephanopoulos, *J. Catal.*, 1998, **179**, 203–221.
140 A. A. Ansari, J. P. Labis, M. Alam, S. M. Ramay, N. Ahmed and A. Mahmood, *Anal. Lett.*, 2017, **50**, 1360–1371.
141 W. Tang, Z. Hu, M. Wang, G. D. Stucky, H. Metiu and E. W. McFarland, *J. Catal.*, 2010, **273**, 125–137.
142 Y.-Q. Su, I. A. W. Filot, J.-X. Liu and E. J. M. Hensen, *ACS Catal.*, 2018, **8**, 75–80.
143 S. Colussi, A. Gayen, M. Farnesi Camellone, M. Boaro, J. Llorca, S. Fabris and A. Trovarelli, *Angew. Chem., Int. Ed.*, 2009, **48**, 8481–8484.
144 E. Aneggi, C. de Leitenburg and A. Trovarelli, *Catal. Today*, 2012, **181**, 108–115.
145 I. Atribak, A. Bueno-Lopez and A. Garcia-Garcia, *Top. Catal.*, 2009, **52**, 2088.
146 M. Konsolakis, S. A. C. Carabineiro, G. E. Marnellos, M. F. Asad, O. S. G. P. Soares, M. F. R. Pereira, J. J. M. Órfão and J. L. Figueiredo, *Inorg. Chim. Acta*, 2017, **455**, 473–482.
147 D. Marrocchelli, S. R. Bishop, H. L. Tuller and B. Yildiz, *Adv. Funct. Mater.*, 2012, **22**, 1958–1965.
148 R. Grau-Crespo, H. de Leeuw Nora, S. Hamad and V. Waghmare Umesh, *Proc. R. Soc. A*, 2011, **467**, 1925–1938.
149 M. Yashima, *J. Phys. Chem. C*, 2009, **113**, 12658–12662.
150 F. Capel, C. Moure and P. Durán, *Ceram. Int.*, 2002, **28**, 627–636.
151 M. Fu, L. Wei, Y. Li, X. Zhou, S. Hao and Y. Li, *Solid State Sci.*, 2009, **11**, 2133–2137.
152 X. Feng, D. C. Sayle, Z. L. Wang, M. S. Paras, B. Santora, A. C. Sutorik, T. X. T. Sayle, Y. Yang, Y. Ding, X. Wang and Y.-S. Her, *Science*, 2006, **312**, 1504.
153 A. Gupta, U. V. Waghmare and M. S. Hegde, *Chem. Mater.*, 2010, **22**, 5184–5198.
154 U. Castanet, C. Feral-Martin, A. Demourgues, R. L. Neale, D. C. Sayle, F. Caddeo, J. M. Flitcroft, R. Caygill, B. J. Pointon, M. Molinari and J. Majimel, *ACS Appl. Mater. Interfaces*, 2019, **11**, 11384–11390.
155 A. Gupta, A. Kumar, U. V. Waghmare and M. S. Hegde, *Chem. Mater.*, 2009, **21**, 4880–4891.
156 G. Dutta, U. V. Waghmare, T. Baidya, M. S. Hegde, K. R. Priolkar and P. R. Sarode, *Chem. Mater.*, 2006, **18**, 3249–3256.
157 M. Nolan, *J. Chem. Phys.*, 2009, **130**, 144702.
158 Z. Yang, Z. Lu, G. Luo and K. Hermansson, *Phys. Lett. A*, 2007, **369**, 132–139.
159 M. Alfredsson and C. R. A. Catlow, *Phys. Chem. Chem. Phys.*, 2002, **4**, 6100–6108.
160 M. D. Krcha, A. D. Mayernick and M. J. Janik, *J. Catal.*, 2012, **293**, 103–115.
161 A. Romero-Núñez and G. Díaz, *RSC Adv.*, 2015, **5**, 54571–54579.
162 S. Gatla, D. Aubert, G. Agostini, O. Mathon, S. Pascarelli, T. Lunkenbein, M. G. Willinger and H. Kaper, *ACS Catal.*, 2016, **6**, 6151–6155.
163 H. Zhu, Y. Chen, Z. Wang, W. Liu and L. Wang, *RSC Adv.*, 2018, **8**, 14888–14897.
164 M. Mittal, A. Gupta and O. P. Pandey, *Sol. Energy*, 2018, **165**, 206–216.
165 S. D. Senanayake, D. Stacchiola and J. A. Rodriguez, *Acc. Chem. Res.*, 2013, **46**, 1702–1711.
166 K. Mudiyanselage, S. D. Senanayake, L. Feria, S. Kundu, A. E. Baber, J. Graciani, A. B. Vidal, S. Agnoli, J. Evans, R. Chang, S. Axnanda, Z. Liu, J. F. Sanz, P. Liu, J. A. Rodriguez and D. J. Stacchiola, *Angew. Chem., Int. Ed.*, 2013, **52**, 5101–5105.
167 X. Wang, J. A. Rodriguez, J. C. Hanson, D. Gamarra, A. Martínez-Arias and M. Fernández-García, *J. Phys. Chem. B*, 2006, **110**, 428–434.
168 R. Kopelent, J. A. van Bokhoven, J. Szlachetko, J. Edebeli, C. Paun, M. Nachtegaal and O. V. Safonova, *Angew. Chem., Int. Ed.*, 2015, **54**, 8728–8731.
169 A. S. Karakoti, N. A. Monteiro-Riviere, R. Aggarwal, J. P. Davis, R. J. Narayan, W. T. Self, J. McGinnis and S. Seal, *JOM*, 2008, **60**, 33–37.
170 S. Das, J. M. Dowding, K. E. Klump, J. F. McGinnis, W. Self and S. Seal, *Nanomedicine*, 2013, **8**, 1483–1508.
171 C. Walkey, S. Das, S. Seal, J. Erlichman, K. Heckman, L. Ghibelli, E. Traversa, J. F. McGinnis and W. T. Self, *Environ. Sci.: Nano*, 2015, **2**, 33–53.
172 C. Korsvik, S. Patil, S. Seal and W. T. Self, *Chem. Commun.*, 2007, 1056–1058.
173 T. Pirmohamed, J. M. Dowding, S. Singh, B. Wasserman, E. Heckert, A. S. Karakoti, J. E. S. King, S. Seal and W. T. Self, *Chem. Commun.*, 2010, **46**, 2736–2738.
174 B. A. Rzigalinski, K. Meehan, R. M. Davis, Y. Xu, W. C. Miles and C. A. Cohen, *Nanomedicine*, 2006, **1**, 399–412.

175 M. Das, S. Patil, N. Bhargava, J.-F. Kang, L. M. Riedel, S. Seal and J. J. Hickman, *Biomaterials*, 2007, **28**, 1918–1925.
176 Y. Xue, Q. Luan, D. Yang, X. Yao and K. Zhou, *J. Phys. Chem. C*, 2011, **115**, 4433–4438.
177 C. Li, X. Shi, Q. Shen, C. Guo, Z. Hou and J. Zhang, *J. Nanomater.*, 2018, **2018**, 12.
178 B. C. Nelson, M. E. Johnson, M. L. Walker, K. R. Riley and C. M. Sims, *Antioxidants*, 2016, **5**, 15.
179 F. Pagliari, C. Mandoli, G. Forte, E. Magnani, S. Pagliari, G. Nardone, S. Licoccia, M. Minieri, P. Di Nardo and E. Traversa, *ACS Nano*, 2012, **6**, 3767–3775.
180 C. Xu and X. Qu, *NPG Asia Mater.*, 2014, **6**, e90.
181 C. López-Alarcón and A. Denicola, *Anal. Chim. Acta*, 2013, **763**, 1–10.
182 B. Drew and C. Leeuwenburgh, *Ann. N. Y. Acad. Sci.*, 2002, **959**, 66–81.
183 B. Uttara, A. V. Singh, P. Zamboni and R. T. Mahajan, *Curr. Neuropharmacol.*, 2009, **7**, 65–74.
184 J. M. McCord and I. Fridovich, *J. Biol. Chem.*, 1969, **244**, 6049–6055.
185 S. Singh, *Front. Chem.*, 2019, **7**, 46.
186 T. Fukai and M. Ushio-Fukai, *Antioxid. Redox Signaling*, 2011, **15**, 1583–1606.
187 E. G. Heckert, A. S. Karakoti, S. Seal and W. T. Self, *Biomaterials*, 2008, **29**, 2705–2709.
188 A. Karakoti, S. Singh, J. M. Dowding, S. Seal and W. T. Self, *Chem. Soc. Rev.*, 2010, **39**, 4422–4432.
189 S. Singh, T. Dosani, A. S. Karakoti, A. Kumar, S. Seal and W. T. Self, *Biomaterials*, 2011, **32**, 6745–6753.
190 J. M. Perez, A. Asati, S. Nath and C. Kaittanis, *Small*, 2008, **4**, 552–556.
191 A. S. Karakoti, P. Munusamy, K. Hostetler, V. Kodali, S. Kuchibhatla, G. Orr, J. G. Pounds, J. G. Teeguarden, B. D. Thrall and D. R. Baer, *Surf. Interface Anal.*, 2012, **44**, 882–889.
192 B. Lipinski, *Oxid. Med. Cell. Longevity*, 2011, 2011.
193 V. Prabhakaran, C. G. Arges and V. Ramani, *Proc. Natl. Acad. Sci. U. S. A.*, 2012, **109**, 1029–1034.
194 Y. Zhang, K. Zhou, Y. Zhai, F. Qin, L. Pan and X. Yao, *RSC Adv.*, 2014, **4**, 50325–50330.
195 Y. Y. Huang, J. S. Ren and X. G. Qu, *Chem. Rev.*, 2019, **119**, 4357–4412.
196 D. W. Jiang, D. L. Ni, Z. T. Rosenkrans, P. Huang, X. Y. Yan and W. B. Cai, *Chem. Soc. Rev.*, 2019, **48**, 3683–3704.
197 L. A. Ridnour, D. D. Thomas, D. Mancardi, M. G. Espey, K. M. Miranda, N. Paolocci, M. Feelisch, J. Fukuto and D. A. Wink, *Biol. Chem.*, 2004, **385**, 1.
198 J. M. Dowding, T. Dosani, A. Kumar, S. Seal and W. T. Self, *Chem. Commun.*, 2012, **48**, 4896–4898.
199 S. Singh, *Front. Chem.*, 2019, 7.
200 J. M. Dowding, S. Das, A. Kumar, T. Dosani, R. McCormack, A. Gupta, T. X. T. Sayle, D. C. Sayle, L. von Kalm, S. Seal and W. T. Self, *ACS Nano*, 2013, **7**, 4855–4868.
201 X. Jiao, H. Song, H. Zhao, W. Bai, L. Zhang and Y. Lv, *Anal. Methods*, 2012, **4**, 3261–3267.
202 P. Cohen, *Nat. Cell Biol.*, 2002, **4**, E127.
203 J. Chin, *Curr. Opin. Chem. Biol.*, 1997, **1**, 514–521.
204 S. J. Franklin, *Curr. Opin. Chem. Biol.*, 2001, **5**, 201–208.
205 F. Tan, Y. Zhang, J. Wang, J. Wei, Y. Cai and X. Qian, *J. Mass Spectrom.*, 2008, **43**, 628–632.
206 A. J. Patil, R. K. Kumar, N. J. Barron and S. Mann, *Chem. Commun.*, 2012, **48**, 7934–7936.
207 M. H. Kuchma, C. B. Komanski, J. Colon, A. Teblum, A. E. Masunov, B. Alvarado, S. Babu, S. Seal, J. Summy and C. H. Baker, *Nanomedicine*, 2010, **6**, 738–744.
208 H. J. Kwon, D. Kim, K. Seo, Y. G. Kim, S. I. Han, T. Kang, M. Soh and T. Hyeon, *Angew. Chem., Int. Ed.*, 2018, **57**, 9408–9412.
209 P. Eriksson, A. A. Tal, A. Skallberg, C. Brommesson, Z. Hu, R. D. Boyd, W. Olovsson, N. Fairley, I. A. Abrikosov, X. Zhang and K. Uvdal, *Sci. Rep.*, 2018, **8**, 6999.
210 M. Huang and S. Fabris, *Phys. Rev. B: Condens. Matter Mater. Phys.*, 2007, **75**, 081404.
211 X. Huang and M. J. Beck, *Chem. Mater.*, 2015, **27**, 5840–5844.
212 Z. Wu, M. Li, J. Howe, H. M. Meyer III and S. H. Overbury, *Langmuir*, 2010, **26**, 16595–16606.
213 G. Preda, A. Migani, K. M. Neyman, S. T. Bromley, F. Illas and G. Pacchioni, *J. Phys. Chem. C*, 2011, **115**, 5817–5822.
214 S. Fabris, G. Vicario, G. Balducci, S. de Gironcoli and S. Baroni, *J. Phys. Chem. B*, 2005, **109**, 22860–22867.
215 V. V. Pushkarev, V. I. Kovalchuk and J. L. d'Itri, *J. Phys. Chem. B*, 2004, **108**, 5341–5348.
216 C. Li, K. Domen, K.-I. Maruya and T. Onishi, *J. Catal.*, 1990, **123**, 436–442.
217 Y. M. Choi, H. Abernathy, H.-T. Chen, M. C. Lin and M. Liu, *ChemPhysChem*, 2006, **7**, 1957–1963.
218 C. Loschen, A. Migani, S. T. Bromley, F. Illas and K. M. Neyman, *Phys. Chem. Chem. Phys.*, 2008, **10**, 5730–5738.
219 C. Li, K. Domen, K. Maruya and T. Onishi, *J. Am. Chem. Soc.*, 1989, **111**, 7683–7687.
220 Z. Wu, M. Li, J. Howe, H. M. Meyer and S. H. Overbury, *Langmuir*, 2010, **26**, 16595–16606.
221 F. Vindigni, M. Manzoli, A. Damin, T. Tabakova and A. Zecchina, *Chem. – Eur. J.*, 2011, **17**, 4356–4361.
222 C. Yang, X. Yu, S. Heissler, P. G. Weidler, A. Nefedov, Y. Wang, C. Woell, T. Kropp, J. Paier and J. Sauer, *Angew. Chem., Int. Ed.*, 2017, **56**, 16399–16404.
223 H.-T. Chen, J.-G. Chang, H.-L. Chen and S.-P. Ju, *J. Comput. Chem.*, 2009, **30**, 2433–2442.
224 M. Ornatska, E. Sharpe, D. Andreescu and S. Andreescu, *Anal. Chem.*, 2011, **83**, 4273–4280.
225 S. S. Lee, W. Song, M. Cho, H. L. Puppala, P. Nguyen, H. Zhu, L. Segatori and V. L. Colvin, *ACS Nano*, 2013, **7**, 9693–9703.
226 S. Saraf, C. J. Neal, S. Das, S. Barkam, R. McCormack and S. Seal, *ACS Appl. Mater. Interfaces*, 2014, **6**, 5472–5482.
227 P. Yu, S. A. Hayes, T. J. O'Keefe, M. J. O'Keefe and J. O. Stoffer, *J. Electrochem. Soc.*, 2006, **153**, C74–C79.
228 F. H. Scholes, C. Soste, A. E. Hughes, S. G. Hardin and P. R. Curtis, *Appl. Surf. Sci.*, 2006, **253**, 1770–1780.

 

229 M. Ornatska, E. Sharpe, D. Andreescu and S. Andreescu, *Anal. Chem.*, 2011, **83**, 4273–4280.
230 N. P. Sardesai, D. Andreescu and S. Andreescu, *J. Am. Chem. Soc.*, 2013, **135**, 16770–16773.
231 Y.-J. Wang, H. Dong, G.-M. Lyu, H.-Y. Zhang, J. Ke, L.-Q. Kang, J.-L. Teng, L.-D. Sun, R. Si, J. Zhang, Y.-J. Liu, Y.-W. Zhang, Y.-H. Huang and C.-H. Yan, *Nanoscale*, 2015, **7**, 13981–13990.
232 D. Damatov and J. M. Mayer, *Chem. Commun.*, 2016, **52**, 10281–10284.
233 K. Binnemans, P. T. Jones, K. Van Acker, B. Blanpain, B. Mishra and D. Apelian, *JOM*, 2013, **65**, 846–848.
234 G. A. Campbell, *Miner. Econ.*, 2014, **27**, 21–31.
235 K. Binnemans, P. T. Jones, B. Blanpain, T. Van Gerven, Y. Yang, A. Walton and M. Buchert, *J. Cleaner Prod.*, 2013, **51**, 1–22.
236 S. Jakab, S. Picart, B. Tribollet, P. Rousseau, H. Perrot and C. Gabrielli, *Anal. Chem.*, 2009, **81**, 5139–5145.
237 X. Beaudoux, M. Virot, T. Chave, G. Durand, G. Leturcq and S. I. Nikitenko, *Green Chem.*, 2016, **18**, 3656–3668.
238 M. Virot, T. Chave, D. Horlait, N. Clavier, N. Dacheux, J. Ravaux and S. I. Nikitenko, *J. Mater. Chem.*, 2012, **22**, 14734–14740.
239 S. Tamilmani, V. Lowalekar, S. Raghavan and R. Small, 7th International Symposium on Ultra Clean Processing of Silicon Surfaces, UCPSS 2004, 2005.
240 *US Pat.*, US6568995B1, 2003.
241 *US Pat.*, US6326305 B1, 2001.
242 N. Um, M. Miyake and T. Hirato, *Green Energy and Technology*, 2011, 66, DOI: 10.1007/978-4-431-53910-0_22.
243 D. Horlait, N. Clavier, S. Szenknect, N. Dacheux and V. Dubois, *Inorg. Chem.*, 2012, **51**, 3868–3878.
244 K. Dhamodharan, T. Aneesh and A. Pius, *J. Radioanal. Nucl. Chem.*, 2019, **319**, 1127–1133.
245 J. T. Dahle, K. Livi and Y. Arai, *Chemosphere*, 2015, **119**, 1365–1371.
246 M. S. A. Asghar, B. J. Inkson and G. Möbus, *ChemPhysChem*, 2017, **18**, 1247–1251.
247 P. Janos, P. Kuran, M. Kormunda, V. Stengl, T. M. Grygar, M. Dosek, M. Stastny, J. Ederer, V. Pilarova and L. Vrtoch, *J. Rare Earths*, 2014, **32**, 360–370.
248 P. Janoš, J. Ederer and M. Došek, *Nova Biotechnol. Chim.*, 2014, **13**, 148.
249 P. Janoš, P. Kuráň, J. Ederer, M. Šťastný, L. Vrtoch, M. Pšenička, J. Henych, K. Mazanec and M. Skoumal, *Adv. Mater. Sci. Eng.*, 2015, **2015**, 241421.
250 W. Kim, B. Kim, D. Choi, T. Oki and S. Kim, *J. Hazard. Mater.*, 2010, **183**, 29–34.
251 Y. Xu, S. S. Mofarah, R. Mehmood, C. Cazorla, P. Koshy and C. C. Sorrell, *Mater. Horiz.*, 2021, **8**, 102–123.
252 Y. Shlapa, S. Solopan, V. Sarnatskaya, K. Siposova, I. Garcarova, K. Veltruska, I. Timashkov, O. Lykhova, D. Kolesnik, A. Musatov, V. Nikolaev and A. Belous, *Colloids Surf., B*, 2022, **220**, 112960.
253 M. Nyoka, Y. Choonara, P. Kumar, P. P. D. Kondiah and V. Pillay, *Nanomaterials*, 2020, **10**(2), 242.
254 T. Yu, J. Joo, Y. I. Park and T. Hyeon, *Angew. Chem.*, 2005, **44**, 7411–7414.
255 V. D. Araújo, W. Avansi, H. B. de Carvalho, M. L. Moreira, E. Longo, C. Ribeirod and M. I. B. Bernardia, *CrystEngComm*, 2012, **14**, 1150–1154.
256 S. Kar, C. Patel and S. Santra, *J. Phys. Chem. C*, 2009, **113**, 4862–4867.
257 A. F. Zedan, S. Moussa and M. S. El-Shall, *Mater. Res. Express*, 2023, 10.
258 K. R. Singh, V. Nayak, T. Sarkar and R. P. Singh, *RSC Adv.*, 2020, **10**, 27194–27214.
259 R. Olbrich, G. E. Murgida, V. Ferrari, C. Barth, A. M. Llois, M. Reichling and M. V. Ganduglia-Pirovano, *J. Phys. Chem. C*, 2017, **121**, 6844–6851.
260 Z. Nie, A. Petukhova and E. Kumacheva, *Nat. Nanotechnol.*, 2009, **5**, 15.
261 W.-J. Ong, L.-L. Tan, S.-P. Chai and S.-T. Yong, *Chem. Commun.*, 2015, **51**, 858–861.
262 Z. Ji, X. Shen, M. Li, H. Zhou, G. Zhu and K. Chen, *Nanotechnology*, 2013, **24**, 115603.
263 M. E. Khan, M. M. Khan and M. H. Cho, *Sci. Rep.*, 2017, **7**, 5928.
264 A. S. Dezfuli, M. R. Ganjali, H. R. Naderi and P. Norouzi, *RSC Adv.*, 2015, **5**, 46050–46058.
265 D. Joung, V. Singh, S. Park, A. Schulte, S. Seal and S. I. Khondaker, *J. Phys. Chem. C*, 2011, **115**, 24494–24500.
266 Y. Wang, C. X. Guo, J. Liu, T. Chen, H. Yang and C. M. Li, *Dalton Trans.*, 2011, **40**, 6388–6391.
267 M. M. Khan, S. A. Ansari, D. Pradhan, D. H. Han, J. Lee and M. H. Cho, *Ind. Eng. Chem. Res.*, 2014, **53**, 9754–9763.
268 D. Joung, V. Singh, S. Park, A. Schulte, S. Seal and S. I. Khondaker, *J. Phys. Chem. C*, 2011, **115**, 24494–24500.
269 A. Othman, E. Dumitrescu, D. Andreescu and S. Andreescu, *ACS Sustainable Chem. Eng.*, 2018, **6**, 12542–12561.
270 L. Yu, Y. Ma, C. N. Ong, J. Xie and Y. Liu, *RSC Adv.*, 2015, **5**, 64983–64990.
271 A. Baranik, R. Sitko, A. Gagor, I. Queralt, E. Marguí and B. Zawisza, *Anal. Chem.*, 2018, **90**, 4150–4159.
272 T. S. Sakthivel, S. Das, C. J. Pratt and S. Seal, *Nanoscale*, 2017, **9**, 3367–3374.
273 A. Szabó, C. Perri, A. Csató, G. Giordano, D. Vuono and J. B. Nagy, *Materials*, 2010, **3**, 3092–3140.
274 X. Qin, F. Peng, F. Yang, X. He, H. Huang, D. Luo, J. Yang, S. Wang, H. Liu, L. Peng and Y. Li, *Nano Lett.*, 2014, **14**, 512–517.
275 S. Sarkar, E. Guibal, F. Quignard and A. K. SenGupta, *J. Nanopart. Res.*, 2012, **14**, 715.
276 S. Wu, J. Dzubiella, J. Kaiser, M. Drechsler, X. Guo, M. Ballauff and Y. Lu, *Angew. Chem., Int. Ed.*, 2012, **51**, 2229–2233.
277 A. Asati, S. Santra, C. Kaittanis and J. M. Perez, *ACS Nano*, 2010, **4**, 5321–5331.
278 W. Song, S. Soo Lee, M. Savini, L. Popp, V. L. Colvin and L. Segatori, *ACS Nano*, 2014, **8**, 10328–10342.
279 R. Mehmood, S. S. Mofarah, A. Rawal, F. Tomasetig, X. C. Wang, J. L. Yang, P. Koshy and C. C. Sorrell, *ACS Sustainable Chem. Eng.*, 2019, **7**, 9189–9201.

280 M. Mari, B. Müller, K. Landfester and R. Muñoz-Espí, *ACS Appl. Mater. Interfaces*, 2015, **7**, 10727–10733.
281 K. Katta, D. Busko, Y. Avlasevich, K. Landfester, S. Baluschev and R. Muñoz-Espí, *Beilstein J. Nanotechnol.*, 2019, **10**, 522–530.
282 M. E. Culica, A. L. Chibac-Scutaru, V. Melinte and S. Coseri, *Materials*, 2020, 13.
283 R. Cao, D. Sun, Y. Liang, M. Hong, K. Tatsumi and Q. Shi, *Inorg. Chem.*, 2002, **41**, 2087–2094.
284 R. Mohammadinasab, M. Tabatabaee, B.-M. Kukovec and H. Aghaie, *Inorg. Chim. Acta*, 2013, **405**, 368–373.
285 P. Gohari Derakhshandeh and J. Soleimannejad, *Ultrason. Sonochem.*, 2016, **31**, 122–128.
286 A. K. Boal, F. Ilhan, J. E. DeRouchey, T. Thurn-Albrecht, T. P. Russell and V. M. Rotello, *Nature*, 2000, **404**, 746–748.
287 L. Qi, J. Fresnais, P. Muller, O. Theodoly, J. F. Berret and J. P. Chapel, *Langmuir*, 2012, **28**, 11448–11456.
288 Z. Shen, J. Liu, F. Hu, S. Liu, N. Cao, Y. Sui, Q. Zeng and Y. Shen, *CrystEngComm*, 2014, **16**, 3387–3394.
289 P. G. Derakhshandeh, J. Soleimannejad and J. Janczak, *Ultrason. Sonochem.*, 2015, **26**, 273–280.
290 Z. Shen, S. He, P. Yao, X. Lao, B. Yang, Y. Dai, X. Sun and T. Chen, *RSC Adv.*, 2014, **4**, 12844–12848.
291 A. U. Czaja, N. Trukhan and U. Müller, *Chem. Soc. Rev.*, 2009, **38**, 1284–1293.
292 W. P. Mounfield, U. Tumuluri, Y. Jiao, M. Li, S. Dai, Z. Wu and K. S. Walton, *Microporous Mesoporous Mater.*, 2016, **227**, 65–75.
293 M. Lammert, M. T. Wharmby, S. Smolders, B. Bueken, A. Lieb, K. A. Lomachenko, D. D. Vos and N. Stock, *Chem. Commun.*, 2015, **51**, 12578–12581.
294 T. Islamoglu, A. Atilgan, S.-Y. Moon, G. W. Peterson, J. B. DeCoste, M. Hall, J. T. Hupp and O. K. Farha, *Chem. Mater.*, 2017, **29**, 2672–2675.
295 A. M. Ebrahim and T. J. Bandosz, *ACS Appl. Mater. Interfaces*, 2013, **5**, 10565–10573.
296 J. Qi, J. Chen, G. Li, S. Li, Y. Gao and Z. Tang, *Energy Environ. Sci.*, 2012, **5**, 8937–8941.
297 T. K. Kim, K. J. Lee, J. Y. Cheon, J. H. Lee, S. H. Joo and H. R. Moon, *J. Am. Chem. Soc.*, 2013, **135**, 8940–8946.
298 H. Wang, M. Liu, S. Guo, Y. Wang, X. Han and Y. Bai, *Mol. Catal.*, 2017, **436**, 120–127.
299 Z. Zhang, H. Shi, Q. Wu, X. Bu, Y. Yang, J. Zhang and Y. Huang, *New J. Chem.*, 2019, **43**, 4581–4589.
300 M. H. Hassan, D. Andreescu and S. Andreescu, *ACS Appl. Nano Mater.*, 2020, **3**, 3288–3294.
301 J. M. Thomas, *J. Chem. Phys.*, 2008, **128**, 182502.
302 J. Zhang, L. P. Li, X. S. Huang and G. S. Li, *J. Mater. Chem.*, 2012, **22**, 10480–10487.
303 J. Qi, J. Chen, G. D. Li, S. X. Li, Y. Gao and Z. Y. Tang, *Energy Environ. Sci.*, 2012, **5**, 8937–8941.
304 S. Song, X. Wang and H. Zhang, *NPG Asia Mater.*, 2015, **7**, e179.
305 A. Figueroba, A. Bruix, G. Kovács and K. M. Neyman, *Phys. Chem. Chem. Phys.*, 2017, **19**, 21729–21738.
306 N. Acerbi, S. Golunski, S. C. Tsang, H. Daly, C. Hardacre, R. Smith and P. Collier, *J. Phys. Chem. C*, 2012, **116**, 13569–13583.
307 E. A. Derevyannikova, T. Y. Kardash, L. S. Kibis, E. M. Slavinskaya, V. A. Svetlichnyi, O. A. Stonkus, A. S. Ivanova and A. I. Boronin, *Phys. Chem. Chem. Phys.*, 2017, **19**, 31883–31897.
308 L. Wang, H. He, Y. Yu, L. Sun, S. Liu, C. Zhang and L. He, *J. Inorg. Biochem.*, 2014, **135**, 45–53.
309 C. M. Magdalane, K. Kaviyarasu, J. J. Vijaya, B. Siddhardha and B. Jeyaraj, *J. Photochem. Photobiol., B*, 2016, **163**, 77–86.
310 R. Kannan, A. R. Kim, S. K. Eo, S. H. Kang and D. J. Yoo, *Ceram. Int.*, 2017, **43**, 3072–3079.
311 Z. Kebin and L. Yadong, *Angew. Chem., Int. Ed.*, 2012, **51**, 602–613.
312 M. Krishnan, J. W. Nalaskowski and L. M. Cook, *Chem. Rev.*, 2010, **110**, 178–204.
313 S. Park, J. M. Vohs and R. J. Gorte, *Nature*, 2000, **404**, 265.
314 P. Jasinski, T. Suzuki and H. U. Anderson, *Sens. Actuators, B*, 2003, **95**, 73–77.
315 L. Truffault, M.-T. Ta, T. Devers, K. Konstantinov, V. Harel, C. Simmonard, C. Andreazza, I. P. Nevirkovets, A. Pineau, O. Veron and J.-P. Blondeau, *Mater. Res. Bull.*, 2010, **45**, 527–535.
316 F. Caputo, M. Mameli, A. Sienkiewicz, S. Licoccia, F. Stellacci, L. Ghibelli and E. Traversa, *Sci. Rep.*, 2017, **7**, 4636.
317 U. Tumuluri, G. Rother and Z. Wu, *Ind. Eng. Chem. Res.*, 2016, **55**, 3909–3919.
318 J. A. Rodriguez, D. C. Grinter, Z. Liu, R. M. Palomino and S. D. Senanayake, *Chem. Soc. Rev.*, 2017, **46**, 1824–1841.
319 A. Trovarelli, *Catal. Rev.*, 1996, **38**, 439–520.
320 K. Polychronopoulou, A. F. Zedan, M. AlKetbi, S. Stephen, M. Ather, M. S. Katsiotis, J. Arvanitidis, D. Christofilos, A. F. Isakovic and S. AlHassan, *J. Environ. Chem. Eng.*, 2018, **6**, 266–280.
321 J. Zhang, Y. Cao, C.-A. Wang and R. Ran, *ACS Appl. Mater. Interfaces*, 2016, **8**, 8670–8677.
322 S. H. Kim, B. C. Park, Y. S. Jeon and Y. K. Kim, *ACS Appl. Mater. Interfaces*, 2018, **10**, 32112–32119.
323 J. Quiroz, J.-M. Giraudon, A. Gervasini, C. Dujardin, C. Lancelot, M. Trentesaux and J.-F. Lamonier, *ACS Catal.*, 2015, **5**, 2260–2269.
324 L. Song, T. Xu, D. Gao, X. Hu, C. Li, S. Li and G. Chen, *Chem. – Eur. J.*, 2019, **25**, 6621–6627.
325 M. Dubey, S. Wadhwa, A. Mathur and R. Kumar, *Appl. Surf. Sci. Adv.*, 2022, **12**, 100340.
326 Y. Mordekovitz, L. Shelly, B. A. Rosen and S. Hayun, *J. Am. Ceram. Soc.*, 2021, **104**, 2337–2347.
327 S. Zhang, C. Zhao, Y. Liu, W. Li, J. Wang, G. Wang, Y. Zhang, H. Zhang and H. Zhao, *Chem. Commun.*, 2019, **55**, 2952–2955.
328 I. Y. Habib, J. Burhan, F. Jaladi, C. M. Lim, A. Usman, N. T. R. N. Kumara, S. C. E. Tsang and A. H. Mahadi, *Catal. Today*, 2021, **375**, 506–513.

 

329 K. Polychronopoulou, A. A. AlKhoori, A. M. Efstathiou, M. A. Jaoude, C. M. Damaskinos, M. A. Baker, A. Almutawa, D. H. Anjum, M. A. Vasiliades, A. Belabbes, L. F. Vega, A. F. Zedan and S. J. Hinder, *ACS Appl. Mater. Interfaces*, 2021, **13**, 22391–22415.
330 H. A. Aleksandrov, I. Z. Koleva, K. M. Neyman, T. T. Tabakova and G. N. Vayssilov, *RSC Adv.*, 2018, **8**, 33728–33741.
331 K. Kuntaiah, P. Sudarsanam, B. M. Reddy and A. Vinu, *RSC Adv.*, 2013, **3**, 7953–7962.
332 A. Chien, N. Ye, C. W. Huang and I. H. Tseng, *Catalysts*, 2021, **11**, 731.
333 N. Sutradhar, A. Sinhamahapatra, S. Pahari, M. Jayachandran, B. Subramanian, H. C. Bajaj and A. B. Panda, *J. Phys. Chem. C*, 2011, **115**, 7628–7637.
334 J. Liu and C. Zhu, *Nanomaterials*, 2021, **11**(9), 2231.
335 A. A. Aboud, H. Al-Kelesh, W. M. A. E. Rouby, A. A. Farghali, A. Hamdedein and M. H. Khedr, *J. Mater. Res. Technol.*, 2018, **7**, 14–20.
336 G. Jayakumar, A. Albert Irudayaraj, A. Dhayal Raj, S. John Sundaram and K. Kaviyarasu, *J. Phys. Chem. Solids*, 2022, **160**, 110369.
337 M. Makkee and J. A. Moulijn, *Catal. Rev.*, 2001, **43**, 489–564.
338 P. Sudarsanam, K. Kuntaiah and B. M. Reddy, *New J. Chem.*, 2014, **38**, 5991–6001.
339 L. F. Nascimento, J. F. Lima, P. C. de Sousa Filho and O. A. Serra, *Chem. Eng. J.*, 2016, **290**, 454–464.
340 Q. Shen, G. Lu, C. Du, Y. Guo, Y. Wang, Y. Guo and X. Gong, *Chem. Eng. J.*, 2013, **218**, 164–172.
341 B. Suryadevara, *Advances in chemical mechanical planarization (CMP)*, Woodhead Publishing, 2016.
342 P. V. Dandu, B. Peethala and S. Babu, *J. Electrochem. Soc.*, 2010, **157**, H869–H874.
343 N. K. Penta, B. Peethala, H. Amanapu, A. Melman and S. Babu, *Colloids Surf., A*, 2013, **429**, 67–73.
344 R. Srinivasan, P. V. Dandu and S. Babu, *ECS J. Solid State Sci. Technol.*, 2015, **4**, P5029–P5039.
345 P. D. Veera, S. Peddeti and S. Babu, *J. Electrochem. Soc.*, 2009, **156**, H936–H943.
346 J. Seo, J. Moon, J.-Y. Bae, K. S. Yoon, W. Sigmund and U. Paik, *J. Nanosci. Nanotechnol.*, 2014, **14**, 4351–4356.
347 R. Sabia and H. J. Stevens, *Mach. Sci. Technol.*, 2000, **4**, 235–251.
348 H. Doi, M. Suzuki and K. Kinuta, Proceedings of International Conference on Planarization/CMP Technology 2014, 2014.
349 L. M. Cook, *J. Non-Cryst. Solids*, 1990, **120**, 152–171.
350 S. R. Alety, K. V. Sagi and S. Babu, *ECS J. Solid State Sci. Technol.*, 2017, **6**, P898.
351 J. Seo, J. W. Lee, J. Moon, W. Sigmund and U. Paik, *ACS Appl. Mater. Interfaces*, 2014, **6**, 7388–7394.
352 J.-S. Kim, H.-G. Kang, M. Kanemoto, U. Paik and J.-G. Park, *Jpn. J. Appl. Phys.*, 2007, **46**, 7671.
353 P. Janoš, J. Ederer, V. Pilařová, J. Henych, J. Tolasz, D. Milde and T. Opletal, *Wear*, 2016, **362**, 114–120.
354 S.-K. Kim, Y.-H. Kim, U. Paik and J.-G. Park, *J. Electrochem. Soc.*, 2007, **154**, H642–H646.
355 D. Ryuzaki, Y. Hoshi, Y. Machii, N. Koyama, H. Sakurai and T. Ashizawa, 2009 Symposium on VLSI Technology, 2009.
356 H.-G. Kang, J.-D. Koh, S.-W. Han, J. W. Lee, B.-G. Lee, S.-H. Pyi, B.-S. Lee, J.-W. Kim, B. Reiss and J.-D. Jeong, ICPT 2012-International Conference on Planarization/CMP Technology, 2012.
357 *USA Pat.*, 2014.
358 *USA Pat.*, 2012.
359 A. Chen, J. Long, Z. Li and Y. Chen, *J. Mater. Sci.: Mater. Electron.*, 2018, **29**, 11466–11477.
360 Y. Chen, C. Zuo, Z. Li and A. Chen, *J. Alloys Compd.*, 2018, **736**, 276–288.
361 Y. Chen, W. Cai, W. Wang and A. Chen, *J. Nanopart. Res.*, 2019, **21**, 226.
362 Y. Chen, Z. Li and N. Miao, *Tribol. Int.*, 2015, **82**, 211–217.
363 Y. Chen and R. Long, *Appl. Surf. Sci.*, 2011, **257**, 8679–8685.
364 K. Kim, J. Seo, M. Lee, J. Moon, K. Lee, D. K. Yi and U. Paik, *J. Mater. Res.*, 2017, **32**, 2829–2836.
365 N. D. Urban, D. Dickmann, B. Her and B. Santora, *ECS Trans.*, 2016, **72**, 37–42.
366 J. Choe, *Comparison of 20 nm & 10 nm-class 2D Planar NAND and 3D V-NAND Architecture*, Techinsights, 2015.
367 T. C. Li, B. Reiss, S. P. Kuttiatoor, V. Lam, J.-D. Lee and R. Jia, 2015 International Conference on Planarization/CMP Technology (ICPT), 2015.
368 B. Praveen, B.-J. Cho, J.-G. Park and S. Ramanathan, *Mater. Sci. Semicond. Process.*, 2015, **33**, 161–168.
369 J. Cheng, S. Huang, Y. Li, T. Wang, L. Xie and X. Lu, *Appl. Surf. Sci.*, 2020, **506**, 144668.
370 N. Shehata, K. Meehan, M. Hudait and N. Jain, *J. Nanopart. Res.*, 2021, **14**, 1173.
371 X. Feng, D. C. Sayle, Z. L. Wang, M. S. Paras, B. Santora, A. C. Sutorik, T. X. Sayle, Y. Yang, Y. Ding and X. Wang, *Science*, 2006, **312**, 1504–1508.
372 B. W. Liu and J. W. Liu, *TrAC, Trends Anal. Chem.*, 2019, 121.
373 D. Jampaiah, T. Srinivasa Reddy, V. E. Coyle, A. Nafady and S. K. Bhargava, *J. Mater. Chem. B*, 2017, **5**, 720–730.
374 Y. Tao, E. Ju, J. Ren and X. Qu, *Adv. Mater.*, 2015, **27**, 1097–1104.
375 A. S. Finny, A. Othman and S. Andreescu, in *Cerium Oxide ($CeO_2$)*: Synthesis, Properties and Applications*, ed. S. Scirè and L. Palmisano,* Elsevier, 2020, pp. 259–277.
376 A. Othman, A. Karimi and S. Andreescu, *J. Mater. Chem. B*, 2016, **4**, 7178–7203.
377 A. Karimi, A. Othman, A. Uzunoglu, L. Stanciu and S. Andreescu, *Nanoscale*, 2015, **7**, 6909–6923.
378 J. Wu, X. Wang, Q. Wang, Z. Lou, S. Li, Y. Zhu, L. Qin and H. Wei, *Chem. Soc. Rev.*, 2019, **48**, 1004–1076.
379 H. Wei and E. Wang, *Chem. Soc. Rev.*, 2013, **42**, 6060–6093.
380 L. Song, C. Huang, W. Zhang, M. Ma, Z. Chen, N. Gu and Y. Zhang, *Colloids Surf., A*, 2016, **506**, 747–755.

381 Y.-Z. Li, T.-T. Li, W. Chen and Y.-Y. Song, *ACS Appl. Mater. Interfaces*, 2017, **9**, 29881–29888.
382 C. Hou, Y. Wang, Q. Ding, L. Jiang, M. Li, W. Zhu, D. Pan, H. Zhu and M. Liu, *Nanoscale*, 2015, **7**, 18770–18779.
383 L. Ai, L. Li, C. Zhang, J. Fu and J. Jiang, *Chem. – Eur. J.*, 2013, **19**, 15105–15108.
384 S. Kumar, P. Bhushan and S. Bhattacharya, *RSC Adv.*, 2017, **7**, 37568–37577.
385 Y.-W. Bao, X.-W. Hua, H.-H. Ran, J. Zeng and F.-G. Wu, *J. Mater. Chem. B*, 2019, **7**, 296–304.
386 H. Sun, Y. Zhou, J. Ren and X. Qu, *Angew. Chem., Int. Ed.*, 2018, **57**, 9224–9237.
387 I. Celardo, J. Z. Pedersen, E. Traversa and L. Ghibelli, *Nanoscale*, 2011, **3**, 1411–1420.
388 A. A. Ansari, P. R. Solanki and B. D. Malhotra, *J. Biotechnol.*, 2009, **142**, 179–184.
389 J. M. Yong, L. Fu, F. Tang, P. Yu, R. P. Kuchel, J. M. Whitelock and M. S. Lord, *ACS Biomater. Sci. Eng.*, 2022, **8**, 512–525.
390 C. Ispas, J. Njagi, M. Cates and S. Andreescu, *J. Electrochem. Soc.*, 2008, **155**(8), F169.
391 H. Wu, F. Li, S. Wang, J. Lu, J. Li, Y. Du, X. Sun, X. Chen, J. Gao and D. Ling, *Biomaterials*, 2018, **151**, 66–77.
392 S. M. Hirst, A. S. Karakoti, R. D. Tyler, N. Sriranganathan, S. Seal and C. M. Reilly, *Small*, 2009, **5**, 2848–2856.
393 K. Chaudhury, N. Babu K, A. K. Singh, S. Das, A. Kumar and S. Seal, *Nanomedicine*, 2013, **9**, 439–448.
394 D. Zahra, A. Javaid, M. Iqbal, I. Akbar and U. A. Ashfaq, *Crit. Rev. Ther. Drug Carrier Syst.*, 2021, **38**, 1–26.
395 Y. Gao, K. Chen, J.-L. Ma and F. Gao, *OncoTargets Ther.*, 2014, **7**, 835–840.
396 N. Pourkhalili, A. Hosseini, A. Nili-Ahmadabadi, S. Hassani, M. Pakzad, M. Baeeri, A. Mohammadirad and M. Abdollahi, *World J. Diabetes*, 2011, **2**, 204–210.
397 R. Najafi, A. Hosseini, H. Ghaznavi, S. Mehrzadi and A. M. Sharifi, *Brain Res. Bull.*, 2017, **131**, 117–122.
398 H. Bao, Z. Zhang, Q. Hua and W. Huang, *Langmuir*, 2014, **30**, 6427–6436.
399 L. Artiglia, S. Agnoli, M. C. Paganini, M. Cattelan and G. Granozzi, *ACS Appl. Mater. Interfaces*, 2014, **6**, 20130–20136.
400 A. Othman, A. Hayat and S. Andreescu, *ACS Appl. Nano Mater.*, 2018, **1**, 5722–5735.
401 E. O. Gubernatorova, X. Liu, A. Othman, W. T. Muraoka, E. P. Koroleva, S. Andreescu and A. V. Tumanov, *Adv. Healthcare Mater.*, 2017, **6**, 1700176.
402 H. Zhao, Y. Dong, P. Jiang, G. Wang and J. Zhang, *ACS Appl. Mater. Interfaces*, 2015, **7**, 6451–6461.
403 A. A. Ansari, P. R. Solanki and B. D. Malhotra, *Appl. Phys. Lett.*, 2008, **92**, 263901.
404 B. W. Liu, Z. C. Huang and J. W. Liu, *Nanoscale*, 2016, **8**, 13562–13567.
405 S. Radhakrishnan and S. J. Kim, *RSC Adv.*, 2015, **5**, 12937–12943.
406 M. Molinari, A. R. Symington, D. C. Sayle, T. S. Sakthivel, S. Seal and S. C. Parker, *ACS Appl. Bio Mater.*, 2019, **2**, 1098–1106.
407 P. Pentyala, V. Singhania, V. K. Duggineni and P. A. Deshpande, *Mol. Catal.*, 2022, **522**, 112190.
408 M. Chen, X. Zhou, C. Xiong, T. Yuan, W. Wang, Y. Zhao, Z. Xue, W. Guo, Q. Wang, H. Wang, Y. Li, H. Zhou and Y. Wu, *ACS Appl. Mater. Interfaces*, 2022, **14**, 21989–21995.
409 A. Kolmakov and M. Moskovits, *Annu. Rev. Mater. Res.*, 2004, **34**, 151–180.
410 C. Schilling and C. Hess, *J. Phys. Chem. C*, 2018, **122**, 2909–2917.
411 C. A. Zito, T. M. Perfecto, A. C. Dippel, D. P. Volanti and D. Koziej, *ACS Appl. Mater. Interfaces*, 2020, **12**, 17745–17751.
412 L. Lyu, Q. Xie, Y. Y. Yang, R. R. Wang, W. F. Cen, S. Y. Luo, W. S. Yang, Y. Gao, Q. Q. Xiao, P. Zou and Y. Yang, *Appl. Surf. Sci.*, 2022, 571.
413 P. Jasinski, T. Suzuki and H. U. Anderson, *Sens. Actuators, B*, 2003, **95**, 73–77.
414 H. J. Beie and A. Gnorich, *Sens. Actuators, B*, 1991, **4**, 393–399.
415 T. Divya, M. P. Nikhila, M. Anju, T. V. A. Kusumam, A. K. Akhila, Y. T. Ravikiran and N. K. Renuka, *Sens. Actuators, B*, 2017, **261**, 85–93.
416 L. S. R. Rocha, M. Cilense, M. A. Ponce, C. M. Aldao, L. L. Oliveira, E. Longo and A. Z. Simoes, *Phys. B*, 2018, **536**, 280–288.
417 F. Charbgoo, M. Ramezani and M. Darroudi, *Biosens. Bioelectron.*, 2017, **96**, 33–43.
418 A. Hayat, J. Cunningham, G. Bulbul and S. Andreescu, *Anal. Chim. Acta*, 2015, **885**, 140–147.
419 A. Hayat and S. Andreescu, *Anal. Chem.*, 2013, **85**, 10028–10032.
420 G. Bulbul, A. Hayat, X. B. Liu and S. Andreescu, *RSC Adv.*, 2016, **6**, 60007–60014.
421 A. Hayat, G. Bulbul and S. Andreescu, *Biosens. Bioelectron.*, 2014, **56**, 334–339.
422 F. Mustafa, S. Liebich and S. Andreescu, *Anal. Chim. Acta*, 2021, 1186.
423 E. Sharpe, R. Bradley, T. Frasco, D. Jayathilaka, A. Marsh and S. Andreescu, *Sens. Actuators, B*, 2014, **193**, 552–562.
424 V. Andrei, E. Sharpe, A. Vasilescu and S. Andreescu, *Talanta*, 2016, **156**, 112–118.
425 E. Sharpe, T. Frasco, D. Andreescu and S. Andreescu, *Analyst*, 2013, **138**, 249–262.
426 A. Othman, L. Norton, A. S. Finny and S. Andreescu, *Talanta*, 2020, 208.
427 F. Mustafa, M. Carhart and S. Andreescu, *ACS Appl. Nano Mater.*, 2021, **4**, 9361–9369.
428 F. Mustafa, A. Othman and S. Andreescu, *Sens. Actuators, B*, 2021, 332.
429 J. Njagi, M. M. Chernov, J. C. Leiter and S. Andreescu, *Anal. Chem.*, 2010, **82**, 989–996.
430 R. E. Ozel, C. Ispas, M. Ganesana, J. C. Leiter and S. Andreescu, *Biosens. Bioelectron.*, 2014, **52**, 397–402.
431 N. P. Sardesai, M. Ganesana, A. Karimi, J. C. Leiter and S. Andreescu, *Anal. Chem.*, 2015, **87**, 2996–3003.
432 N. P. Sardesai, A. Karimi and S. Andreescu, *ChemElectroChem*, 2014, **1**, 2082–2088.

 

433 Z. H. Yang, Y. Zhuo, R. Yuan and Y. Q. Chai, *Biosens. Bioelectron.*, 2015, **69**, 321–327.
434 M. B. Gumpu, N. Nesakumar, S. Sethuraman, U. M. Krishnan and J. B. B. Rayappan, *Sens. Actuators, B*, 2014, **199**, 330–338.
435 E. Kang, J. Lee, B. Y. Won, S. Kim, S. Shin, M. I. Kim and H. G. Park, *RSC Adv.*, 2015, **5**, 78747–78753.
436 A. Pinna, E. Cali, G. Kerherve, G. Galleri, M. Maggini, P. Innocenzi and L. Malfatti, *Nanoscale Adv.*, 2020, **2**, 2387–2396.
437 R. Khan and S. Andreescu, *Biosens. Bioelectron.*, 2024, **248**, 115975.
438 H. Y. Kim, J. K. Ahn, M. I. Kim, K. S. Park and H. G. Park, *Electrochem. Commun.*, 2019, **99**, 5–10.
439 H. Y. Kim, K. S. Park and H. G. Park, *Theranostics*, 2020, **10**, 4507–4514.
440 G. Bubul, A. Hayat and S. Andreescu, *Adv. Healthcare Mater.*, 2016, **5**, 822–828.
441 A. Asati, S. Santra, C. Kaittanis, S. Nath and J. M. Perez, *Angew. Chem., Int. Ed.*, 2009, **48**, 2308–2312.
442 G. Bulbul, A. Hayat and S. Andreescu, *Nanoscale*, 2015, **7**, 13230–13238.
443 R. Wang, Y. Du, Y. Fu, Y. Guo, X. Gao, X. Guo, J. Wei and Y. Yang, *ACS Sens.*, 2023, **8**, 4442–4467.
444 X. Z. Wang, B. W. Liu and J. W. Liu, *Langmuir*, 2018, **34**, 15871–15877.
445 B. W. Liu, Z. Y. Sun, P. J. J. Huang and J. W. Liu, *J. Am. Chem. Soc.*, 2015, **137**, 1290–1295.
446 J. Y. Zhang, J. Wang, J. Liao, Y. Lin, C. B. Zheng and J. W. Liu, *ACS Appl. Mater. Interfaces*, 2021, **13**, 50236–50245.
447 Y. Y. Chang, Q. S. Chen, B. W. Liu, Z. J. Zhang, M. Liu and J. W. Liu, *Inorg. Chem. Commun.*, 2021, 134.
448 R. N. McCormack, P. Mendez, S. Barkam, C. J. Neal, S. Das and S. Seal, *J. Phys. Chem. C*, 2014, **118**, 18992–19006.
449 M. Al Sharabati, R. Sabouni and G. A. Husseini, *Nanomaterials*, 2022, **12**, 277.
450 Y. Ma, X. Qu, C. Liu, Q. Xu and K. Tu, *Front. Mol. Biosci.*, 2021, **8**, 805228.
451 S. Wang, Z. Li, F. Duan, B. Hu, L. He, M. Wang, N. Zhou, Q. Jia and Z. Zhang, *Anal. Chim. Acta*, 2019, **1047**, 150–162.
452 N. Zhou, Y. Ma, B. Hu, L. He, S. Wang, Z. Zhang and S. Lu, *Biosens. Bioelectron.*, 2019, **127**, 92–100.
453 X. Ouyang, W. Li, S. Xie, T. Zhai, M. Yu, J. Gan and X. Lu, *New J. Chem.*, 2013, **37**, 585–588.
454 S. Olivera, K. Chaitra, K. Venkatesh, H. B. Muralidhara, A. Inamuddin, A. M. Asiri and M. I. Ahamed, *Environ. Chem. Lett.*, 2018, **16**(4), 1233–1246.
455 G. K. Sarma, S. Sen Gupta and K. G. Bhattacharyya, *Environ. Sci. Pollut. Res.*, 2019, **26**, 6245–6278.
456 M. Lürling, G. Waajen and F. van Oosterhout, *Water Res.*, 2014, **54**, 78–88.
457 M. H. Hassan, R. Stanton, J. Secora, D. J. Trivedi and S. Andreescu, *ACS Appl. Mater. Interfaces*, 2020, **12**, 52788–52796.
458 T. M. Arsic, A. Kalijadis, B. Matovic, M. Stoiljkovic, J. Pantic, J. Jovanovic, R. Petrovic, B. Jokic and B. Babic, *Process. Appl. Ceram.*, 2016, **10**, 17–23.
459 A. Othman, P. Vargo and S. Andreescu, *ACS Appl. Nano Mater.*, 2019, **2**, 7008–7018.
460 W. Xu, J. Wang, L. Wang, G. Sheng, J. Liu, H. Yu and X. J. Huang, *J. Hazard. Mater.*, 2013, **260**, 498–507.
461 R. Sawana, Y. Somasundar, V. S. Iyer and B. Baruwati, *Appl. Water Sci.*, 2017, **7**, 1223–1230.
462 A. Baranik, A. Gagor, I. Queralt, E. Marguí, R. Sitko and B. Zawisza, *Microchim. Acta*, 2018, **185**, 264.
463 A. Karimi, S. Andreescu and D. Andreescu, *ACS Appl. Mater. Interfaces*, 2019, **11**, 24725–24734.
464 G. Zhang, Z. He and W. Xu, *Chem. Eng. J.*, 2012, **183**, 315–324.
465 J. Wang, W. Xu, L. Chen, Y. Jia, L. Wang, X.-J. Huang and J. Liu, *Chem. Eng. J.*, 2013, **231**, 198–205.
466 P. Zhang, T. Ouyang, S. Chen, R. Li and L. Lai, 2010 4th International Conference on Bioinformatics and Biomedical Engineering, 2010.
467 J. Lin, Y. Wu, A. Khayambashi, X. Wang and Y. Wei, *Adsorpt. Sci. Technol.*, 2018, **36**, 743–761.
468 K. Mukhopadhyay, A. Ghosh, S. K. Das, B. Show, P. Sasikumar and U. Chand Ghosh, *RSC Adv.*, 2017, **7**, 26037–26051.
469 M. Chigondo, H. Kamdem Paumo, M. Bhaumik, K. Pillay and A. Maity, *J. Colloid Interface Sci.*, 2018, **532**, 500–516.
470 E. E. Merodio-Morales, H. E. Reynel-Ávila, D. I. Mendoza-Castillo, C. J. Duran-Valle and A. Bonilla-Petriciolet, *Int. J. Environ. Sci. Technol.*, 2019, 115–128.
471 A. Dhillon, T. Kumar Sharma, S. K. Soni and D. Kumar, *RSC Adv.*, 2016, **6**, 89198–89209.
472 J. G. Dale, S. S. Cox, M. E. Vance, L. C. Man and M. F. Hochella, *Environ. Sci. Technol.*, 2017, **51**, 1973–1980.
473 L. Zhang, J. Pierce, V. L. Leung, D. Wang and W. S. Epling, *J. Phys. Chem. C*, 2013, **117**, 8282–8289.
474 P. Dinesha, S. Kumar and M. A. Rosen, *Biofuel Res. J.*, 2021, **8**, 1374–1383.
475 J. X. Chen, Y. X. Chen, M. J. Zhou, Z. W. Huang, J. Y. Gao, Z. Ma, J. M. Chen and X. F. Tang, *Environ. Sci. Technol.*, 2017, **51**, 473–478.
476 A. F. Santiago, J. F. Sousa, R. C. Guedes, C. E. Jeronimo and M. Benachour, *J. Hazard. Mater.*, 2006, **138**, 325–330.
477 L. Chang, I. P. Chen and S. S. Lin, *Chemosphere*, 2005, **58**, 485–492.
478 S. S. Lin, C. L. Chen, D. J. Chang and C. C. Chen, *Water Res.*, 2002, **36**, 3009–3014.
479 D. Wilson, W. Wang and R. J. G. Lopes, *Appl. Catal., B*, 2012, **123**, 273–281.
480 F. Carraro, A. Fapohunda, M. C. Paganini and S. Agnoli, *ACS Appl. Nano Mater.*, 2018, **1**, 1492–1501.
481 S. Kurajica, I. K. Ivkovic, G. Drazic, V. Shvalya, M. Duplancic, G. Matijasic, U. Cvelbar and K. Muzina, *Ceram. Int.*, 2022, **33**, 29451–29458.
482 P. K. Sane, S. Tambat, S. Sontakke and P. Nemade, *J. Environ. Chem. Eng.*, 2018, **6**, 4476–4489.
483 Y. W. Wang, T. T. Liu and J. W. Liu, *ACS Appl. Nano Mater.*, 2020, **3**, 842–849.
484 A. D. Mayernick, R. Li, K. M. Dooley and M. J. Janik, *J. Phys. Chem. C*, 2011, **115**, 24178–24188.

485 Q. L. Wang, J. J. Zhou, J. C. Zhang, H. Zhu, Y. H. Feng and J. Jin, *Aerosol Air Qual. Res.*, 2020, **20**, 477–488.
486 Y. Z. Guo and H. Therien-Aubin, *ACS Appl. Mater. Interfaces*, 2021, **13**, 37578–37588.
487 D. J. Conley, H. W. Paerl, R. W. Howarth, D. F. Boesch, S. P. Seitzinger, K. E. Havens, C. Lancelot and G. E. Likens, *Science*, 2009, **323**, 1014–1015.
488 Y. G. Ko, T. Do, Y. Chun, C. H. Kim, U. S. Choi and J.-Y. Kim, *J. Hazard. Mater.*, 2016, **307**, 91–98.
489 M. Teng, L. Luo and X. Yang, *Microporous Mesoporous Mater.*, 2009, **119**, 158–164.
490 Y. Zhang, M. Yang, X.-M. Dou, H. He and D.-S. Wang, *Environ. Sci. Technol.*, 2005, **39**, 7246–7253.
491 Y. Su, W. Yang, W. Sun, Q. Li and J. K. Shang, *Chem. Eng. J.*, 2015, **268**, 270–279.
492 J. Liu, J. Cao, Y. Hu, Y. Han and J. Zhou, *Water Sci. Technol.*, 2017, **76**, 2867–2875.
493 H. Ding, Y. Zhao, Q. Duan, J. Wang, K. Zhang, G. Ding, X. Xie and C. Ding, *J. Rare Earth.*, 2017, **35**, 984–994.
494 M. H. Hassan and S. Andreescu, *Inorg. Chem.*, 2023, **62**(51), 20970–20979.
495 A. Othman, D. Andreescu, D. P. Karunaratne, S. V. Babu and S. Andreescu, *ACS Appl. Mater. Interfaces*, 2017, **9**, 12893–12905.
496 E. Dumitrescu, D. P. Karunaratne, S. V. Babu, K. N. Wallace and S. Andreescu, *Chemosphere*, 2018, **192**, 178–185.
497 J. J. Zhang, K. B. Lee, L. He, J. Seiffert, P. Subramaniam, L. Yang, S. Chen, P. Maguire, G. Mainelis, S. Schwander, T. Tetley, A. Porter, M. Ryan, M. Shaffer, S. Hu, J. Gong and K. F. Chung, *Environ. Sci.: Processes Impacts*, 2016, **18**, 1333–1342.
498 B. Collin, M. Auffan, A. C. Johnson, I. Kaur, A. A. Keller, A. Lazareva, J. R. Lead, X. M. Ma, R. C. Merrifield, C. Svendsen, J. C. White and J. M. Unrine, *Environ. Sci.: Nano*, 2014, **1**, 533–548.
499 A. Arumugam, C. Karthikeyan, A. S. Haja Hameed, K. Gopinath, S. Gowri and V. Karthika, *Mater. Sci. Eng., C*, 2015, **49**, 408–415.
500 S. Kannan and M. Sundrarajan, *Int. J. Nanosci.*, 2014, **13**, 1450018.
501 G. S. Priya, A. Kanneganti, K. A. Kumar, K. V. Rao and S. Bykkam, *Int. J. Sci. Res. Publ.*, 2014, **4**, 199–224.
502 S. Maensiri, C. Masingboon, P. Laokul, W. Jareonboon, V. Promarak, P. L. Anderson and S. Seraphin, *Cryst. Growth Des.*, 2007, **7**, 950–955.
503 M. Darroudi, S. J. Hoseini, R. Kazemi Oskuee, H. A. Hosseini, L. Gholami and S. Gerayli, *Ceram. Int.*, 2014, **40**, 7425–7430.
504 S. A. Khan and A. Ahmad, *Mater. Res. Bull.*, 2013, **48**, 4134–4138.
505 F. Charbgoo, M. B. Ahmad and M. Darroudi, *Int. J. Nanomed.*, 2017, **12**, 1401–1413.
506 F. Zeng, Y. Wu, X. Li, X. Ge, Q. Guo, X. Lou, Z. Cao, B. Hu, N. J. Long, Y. Mao and C. Li, *Angew. Chem., Int. Ed.*, 2018, **130**, 25485–25492.
507 J. L. Y. Tang, S. S. Moonshi and H. T. Ta, *Cell. Mol. Life Sci.*, 2023, **80**, 46.
508 W. Yang, M. Zhang, J. He, M. Gong, J. Sun and X. Yang, *Regener. Biomater.*, 2022, **9**, rbac037.
509 Q. Bao, P. Hu, Y. Xu, T. Cheng, C. Wei, L. Pan and J. Shi, *ACS Nano*, 2018, **12**(7), 6794–6805.
510 Y. Malyukin, P. Maksimchuk, V. Seminko, E. Okrushko and N. Spivak, *J. Phys. Chem. C*, 2018, **122**, 16406–16411.
511 R. W. Tarnuzzer, J. Colon, S. Patil and S. Seal, *Nano Lett.*, 2005, **5**, 2573–2577.
512 M. Das, N. Bhargava, S. Patil, L. Riedel, P. Molnar, S. Seal and J. J. Hickman, *In Vitro Cell. Dev. Biol.: Anim.*, 2005, **41**, 9A–9A.
513 G. A. Silva, *Nat. Nanotechnol.*, 2006, **1**, 92–94.
514 D. Schubert, R. Dargusch, J. Raitano and S. W. Chan, *Biochem. Biophys. Res. Commun.*, 2006, **342**, 86–91.
515 J. M. Dowding, W. Song, K. Bossy, A. Karakoti, A. Kumar, A. Kim, B. Bossy, S. Seal, M. H. Ellisman, G. Perkins, W. T. Self and E. Bossy-Wetzel, *Cell Death Differ.*, 2014, **21**, 1622–1632.
516 D.-W. Kang, C. K. Kim, H.-J. Jeong, M. Soh, T. Kim, I. Choi, C.-K. Ki, D. Kim, W. Yang, T. Hyeon and S.-H. Lee, *NanoResearch*, 2017, **10**, 2743–2760.
517 H. Nosrati, M. Heydari and M. Khodaei, *Mater. Today Bio*, 2023, **23**, 100823.
518 A. P. Dayanandan, W. J. Cho, H. Kang, A. B. Bello, B. J. Kim, Y. Arai and S. H. Lee, *Biomater. Res.*, 2023, **27**, 68.
519 Y. Xue, F. Yang, L. Wu, D. Xia and Y. Liu, *Adv. Healthcare Mater.*, 2024, **13**, e2302858.
520 Q. Weng, H. Sun, C. Fang, F. Xia, H. Liao, J. Lee, J. Wang, A. Xie, J. Ren, X. Guo, F. Li, B. Yang and D. Ling, *Nat. Commun.*, 2021, 12.
521 A. García, J. A. Cámara, A. M. Boullosa, M. Gustà, L. Mondragón, S. Schwartz, E. Casals, I. Abasolo, N. J. Bastús and V. Puntes, *Nanomaterials*, 2023, 2208.
522 P. C. Naha, J. C. Hsu, J. Kim, S. Shah, M. Bouche, S. Si-Mohamed, D. N. Rosario-Berrios, P. Douek, M. Hajfathalian, P. Yasini, S. Singh, M. A. Rosen, M. A. Morgan and D. P. Cormode, *ACS Nano*, 2020, **14**, 10187–10197.
523 S. Kargozar, F. Baino, S. J. Hoseini, S. Hamzehlou, M. Darroudi, J. Verdi, L. Hasanzadeh, H. W. Kim and M. Mozafari, *Nanomedicine*, 2018, **13**, 3051–3069.

 